FREQUENCY DOMAIN QUANTUM PROCESSING VIA FOUR-WAVE MIXING

A Dissertation

Presented to the Faculty of the Graduate School

of Cornell University

in Partial Fulfillment of the Requirements for the Degree of

Doctor of Philosophy

by

Chaitali Joshi

August 2020

FREQUENCY DOMAIN QUANTUM PROCESSING VIA FOUR-WAVE MIXING

Chaitali Joshi

Doctor of Philosophy in Applied and Engineering Physics

Cornell University

Optical photons are excellent flying qubits for future long-distance quantum networks due to negligible decoherence at room temperature. To date, quantum photonic technologies have focused on processing the spatial, temporal and polarization degrees of freedom of light. However, frequency encoding of information has had a profound impact on classical telecommunications, creating mature low-loss fiber-based and integrated photonics hardware that can be exploited to address challenges of scalability in photonic quantum networks. In this dissertation, we use tools from nonlinear optics to realize coherent frequency domain processing of single photons. We use quantum frequency conversion via Bragg scattering four-wave mixing (BS-FWM) to manipulate the spectral and temporal properties of single photons. We use an implementation of BS-FWM that achieves close to unity efficiency and ultra-low noise to develop a powerful toolbox that combines advantages of frequency encoding, fiber and integrated photonic technologies and nonlinear optics for scaling future quantum networks.

The first application discussed in this thesis is a frequency-multiplexed single-photon source. Deterministic, high-quality sources of single photons are a crucial requirement for scalable photonic quantum information processing (QIP). The most widely used single-photon sources are based on nonlinear parametric processes that are inherently probabilistic. Active feed-forward switching and multiplexing of such probabilistically generated photons can be used to generate photons on demand if a sufficiently large number of modes are multiplexed. Schemes based on spatial and temporal multiplexing however suffer from prohibitive switching losses that significantly limit their performance. We implemented an alternative scheme based on frequency multiplexing that breaks this

limitation. We used BS-FWM as a 'frequency switch' to multiplex frequency modes of a broadband probabilistic single-photon source. We demonstrated a 220% enhancement in single-photon generation rate while maintaining low noise properties ($g^{(2)} = 0.07$) essential for quantum applications. This approach has a unique potential to create a deterministic source of single photons on a chip-based integrated photonics platform.

The next application we discuss is Hong-Ou-Mandel (HOM) interference with photons of distinct colors. Such two-photon interference is a fundamentally quantum effect with no classical analogue and is at the heart of photonic QIP. In this work, we combine frequency-entangled photons generated on-chip together with Bragg-scattering four-wave mixing (BS-FWM) in fiber to demonstrate frequency-domain HOM interference with 95% visibility. BS-FWM coherently couples distinct frequency modes while preserving all quantum properties of the input fields and can therefore be used to create an active, tunable 'frequency beam splitter (FBS)'. We observe a rich two-photon interference pattern including quantum beating, previously observed with cold-atomic systems. Remarkably, we observe high fidelity interference even though the photons propagate for much longer than their mutual coherence time, confirming that this is truly a *two-photon interference* phenomenon. In addition to fundamental novelty, this work establishes four-wave mixing as a tool for selective, high-fidelity two-photon operations in the frequency domain, which combined with integrated single photon sources provides a building block for frequency multiplexed photonic quantum networks. This demonstration will also enable applications such as frequency domain boson sampling, which we discuss in detail in this dissertation.

Finally, we demonstrate a single-photon level time lens with picosecond resolution using BS-FWM. We discuss the conditions under which broadband phase-matching can be achieved with BS-FWM. A time lens draws on space-time duality and imparts a quadratic phase shift on the input signal. With this setup, we achieve a temporal magnification

factor of 158 and resolve single-photon level pulses separated by 2.2 ps. Finally, we show that the temporal phase imparted by the BS-FWM pumps can be generalized to realize significantly more complex, unitary operations on broadband temporal modes. In particular, we use numerical optimization via steepest gradient descent to demonstrate temporal mode sorting of field orthogonal but intensity overlapping Hermite-Gaussian temporal modes. These results show that BS-FWM is a powerful tool for temporal mode quantum processing at the single-photon level.

BIOGRAPHICAL SKETCH

Chaitali Joshi was born in Nashik, Maharashtra, India to her parents Aruna and Dilip Joshi. Chaitali completed her schooling at "Kilbil" St. Joseph's High School in Nashik. Chaitali decided to pursue physics as her major during her undergraduate studies after a fortunate run through India's astronomy olympiad program in high school. She completed her Bachelor's in Engineering Physics at the Indian Institute of Technology, Bombay in August 2013. Chaitali developed a particular liking for quantum physics and was fascinated by the elegance of the subject despite it's relative mathematical simplicity. She also spent two summers pursuing research in soft matter and solid state physics at the Indian Institute of Science in 2011 and at the University of Toronto in 2012. Chaitali arrived in Ithaca in Fall 2013 to pursue her graduate studies at Cornell's Department of Applied and Engineering Physics and joined Prof. Alexander Gaeta's nonlinear and quantum optics lab in Fall 2014. The latter half of her PhD was spent in New York City's Columbia University. Having spent six years in the dungeon with her very few photons, she now looks forward to learning circuit quantum electrodynamics in Prof. Mirhosseini's lab at the California Institute of Technology.

To *Aai*, *Baba* and my big sister *Shalmali*

ACKNOWLEDGEMENTS

The work in this dissertation was made possible only due to the excellent advice, guidance and direction of PIs and postdocs who mentored me during my early years, and the unconditional love and support of my family and close friends.

I would like to thank my advisor Prof. Alexander Gaeta. Alex's research style is a rare combination of pragmatism, scientific rigor and originality. Alex gave me the freedom to pursue my ideas and provided me with the best possible resources to accomplish my experimental goals. Thank you Alex, for giving me a chance and for believing in me when it mattered the most. It has been an absolute honor and privilege to be your PhD student.

I would like to thank Prof. Ana Asenjo-Garcia, who has been a mentor, friend, confidante and an inspirational role model. Ana, you have inspired me with your unapologetic, head-first approach to physics (and to ice skating). Thank you for pushing me to get better and to just do it. Thank you for telling me to get up and try just one more time. Thank you for telling me that the jackhammering will one day end and there will be light at the end of the tunnel, there was! And thank you for speaking up, I will always draw from your strength to raise a voice in order to create a more equal, inclusive and respectful workplace for female scientists.

I would like to thank Prof. Michal Lipson, who has always been generous with her insights, advice and help. Michal's creativity and brilliance are unparalleled, and I have been exceptionally fortunate to have collaborated with her group during my PhD.

I would like to thank Prof. Gregory Fuchs, who has been the chair of my committee at Cornell and who regularly gave me extremely useful advice on quantum optics experiments especially during the early years of this dissertation. I would also like to thank Prof. David Bindel from Computer Science. I had the opportunity to work on a small project on numerical methods for scattering problems in Fall 2015. My applied mathematics

coursework at Cornell has been tremendously beneficial to me and has helped me develop deeper understanding of computational complexity and quantum information theory. I would like to thank Prof. Frank Wise, Prof. James Sethna and Prof. Farhan Rana, who's courses and early advice have helped me tremendously throughout graduate school.

I have benefited tremendously from the work and insights of those who were part of Alex and Michal's group long before I was. I would like to thank Dr. Alessandro Farsi for being the most amazing colleague and friend I could have asked for. Alessandro is a brilliant physicist and an even better experimentalist. The quantum lab is still full of Alessandro's "home-brewed" EDFA's, pulsed lasers and APDs. Thank you Alessandro, for being so generous with your time and inputs. You created so much with so few resources. I hope I did some justice to your amazing work by taking it forward. Most importantly, thank you for being one of the most amazing human beings I have ever known. Here is to more secret adventures in Boulder!

I would like to thank Dr. Sven Ramelow for training me in the lab with great patience in my first year. I have benefited so much from the many experimental trade secrets that I learnt from Sven. Sven's style of writing papers has influenced me greatly. Thank you Sven, for setting me on the right path early on. You are just amazing! Shanti shanti shanti...

I would like to thank Dr. Prathamesh Donvalkar, with whom I worked in the rubidium lab in my first year. Pratham's hard work and dedication to every experiment, and he had many, was influential in making me realize what an experimental physics PhD would take. Pratham has always been a great friend and colleague, and his shenanigans outside the lab are truly missed.

I would like to thank Prof. Dr. Aseema Mohanty, who has been my "quantum buddy" in the Lipson group since Cornell days. I am so lucky to have such a brilliant, determined and kind hearted scientist as a friend and mentor. One day when this is all over, we shall

return and conquer the floors of fat cat. Aseema, I know you want to do it the hard way and I know you will win. Thank you for being you!

I would like to thank my lab mates who have kept me much delightful company late in the evening in the office. Thank you Bok for all the banter and for rescue from broken computers. Your future is brighter and more colorful than all the efficient combs you generate put together. Thank you CSJ for all the sarcasm on Sharapova, the general "vatratpana" and useful inputs before the CAD deadlines. Thank you Yoshi, for organizing the most fun Halloween parties, for taking care of the lab, for generously sharing equipment and for listening to my rants. Thank you Yun for all the quantum discussions. Ara, Adrea, MJ and Jae are always a delight to hangout with. Yair and Ricky, we shall get hummus again! Many thanks are due to members of the ultrafast lab, Jared, Cecilia and Mehdi who are always super fun and helpful. Andrew and Miri, it has been fun working with you guys in the short time we overlapped. I hope you take your inheritance to greater heights.

I would like to thank Dr. Xingchen Ji for fabricating the devices used in this thesis and for being generous during CAD deadlines. Thanks to Oscar, Jakob, Steve, Chris, Utsav for many conversations in the Lipson office and at CLEO parties. Thank you to Gaurang and Ipshita for the chai, for the adventures in various boroughs of NYC and all the corridor chatter. I would like to thank Shriddha Chaitanya, for always being ready to hit some tennis balls, for the ferry rides, for the gossip and deep conversation. Shriddha, your hard work and dedication will pay off immensely and I look forward to seeing you all grown up one day.

I have been so fortunate to have made many friends during this PhD, especially during my early years at Cornell. Ved, you're the first person I met after I landed in Ithaca. Your work hard, train harder and party hardest style never ceases to inspire. Your general Tso's stir fry is sorely missed! I would not have survived Ithaca's brutal winters

without Sophie Dramé-Maigné's warmth and friendship. Sophie, your jovial spirit and your apple crumble are both missed, and I promise to come to Paris to find them one day. Arzoo Katiyar was my first friend in Ithaca, whose company I have missed the most after moving to New York. Go forth with your new adventures, I know you will go places very few have managed see. Neeraj and Prateek have been my tennis buddies and amazing friends. We're all done with our A-exams, but the celebrations can go on. Sarah and Neann, thank you for introducing me to so much in this new country and for always looking out for me. I miss our ITAP shenanigans. Thank you to Yu-Dai Tsai, Dan Quach and other friends from Cornell physics, you made TAing fun!

I would like to thank Gauri Patwardhan, for being the most kind and caring roommate for the last six years. I miss our hangouts in 156, at Bandwagon and at Argos. Thank you for keeping my secrets safe with you. And please come to California.

I would like to thank Rajveer Nehra, of the "why does your multiplexing not work with 99% efficiency" fame. Thank you for all the shayari, Ghalib and crazy road trips. Thank you for reminding me that climbing down was never an option. Cheers to more tacos and photons in LA!

Pratik, it is a miracle that our paths have crossed. Your jubilant spirit that weathers every deadline with a huge smile is so contagious. Your brilliance, originality and incessant drive to "nail it" is perhaps only eclipsed by your magnanimous and kind hearted soul. You want to conquer the world, and I know you will!

I would like to thank Dr. Avik Dutt who has been one of my closest friends since my first week at Cornell. Thank you Avik, for homeworking with me in the Nines, for editing abstracts at 5 am the day of the deadline, letting me into the Cornell stock room at midnight and for being there each and every step of the way. For cracking all those stupid jokes and making the most hilarious puns. You give so much to those around you and to science itself. I would have never made it to the finish line without you. But then

del dot E would still be rho by epsilon.

Thank you to the insti friends, Deepak, Thukral, Sneha, Sajan, Dishi, Patil, Tau and Surabhi, for their rock solid dosti over the last decade. Your calls light up my days, cure my homesickness and make it all worth it.

Finally, I would like to thank my family. Aai and Baba have worked hard to create this path for me for so many decades. Thank you for encouraging me to always aim for the most, and for your unconditional love and support through this long journey. And thank you to my big sister Shalmali, words are insufficient to express how much I love you and how much everything you do means to me.

TABLE OF CONTENTS

LIST OF TABLES

LIST OF FIGURES

CHAPTER 1

INTRODUCTION

1.1 Quantum information processing in the frequency domain

Frequency encoding of information has had a profound impact on classical telecommunication technologies, but remains relatively unexplored for quantum information processing (QIP). The revolutionary potential of the frequency degree of freedom of a photon lies in the fact that it enables dense encoding and processing of quantum information in a single spatial mode. In classical telecom applications, interactions between fields of different frequencies are undesirable and much effort is invested in eliminating "crosstalk". In order to create a "color qubit" however, it is necessary to create a photon in a superposition state consisting of various frequencies. This requires different optical frequencies to interact and is made possible using tools from *nonlinear optics*. This dissertation explores the use of nonlinear optical processes to induce *coherent, low-noise interactions* between quantum fields of distinct frequencies.

The optical response of dielectric materials is ordinarily linear. However, when sufficiently intense optical fields create an electric field that is comparable to the atomic fields binding electrons to the nucleus, nonlinear effects arise and the polarization induced in the medium becomes non-trivially dependent on the intensity of incident fields [1]. This intensity dependent polarization leads to a variety of nonlinear wave mixing effects such as three and four-wave mixing. Strong classical fields can mediate the interaction between quantum level fields via this nonlinear material response. This leads us to techniques for frequency domain processing of photons using nonlinear optics.

Achieving efficient interaction between quantum fields of different frequencies is

challenging as this requires a strong nonlinear process that does not introduce additional noise. For this purpose, we use Bragg scattering four wave mixing (BS-FWM), a third order parametric process that we implement with close to unity efficiency and ultra-low noise. The process can be engineered to emulate a unitary, two-mode beam splitter type interaction [2]. BS-FWM was first explored for efficient quantum frequency translation (QFT) between closely spaced frequency modes (few hundred GHz to a few THz) [3]. In this dissertation, we demonstrate several applications that show that BS-FWM is a versatile toolbox for manipulating the spectral and temporal properties of single-photon fields and show applications of this process that go far beyond QFT. A significant advantage of BS-FWM is that the interaction between the quantum fields can be controlled by changing the properties of the classical pump waves involved in the interaction. In our experiments, we realize flexible phase-matching conditions that allow wide-tunability between the input and target frequency modes, enabling scalable multiplexing operations. Finally, by including auxiliary pump fields, arbitrary unitary interactions between a large number of frequency modes can be realized in a monolithic optical structure such as a fiber. This is particularly useful for experiments such as boson sampling which require simultaneous operations and interference of a large number (30-50) of modes to demonstrate quantum advantage.

In addition to fundamental novelty, this work seeks to address several technical obstacles in scaling photonic quantum networks to regimes that are challenging to achieve with spatial, polarization or temporal mode encodings. A major challenge for photonic QIP is the probabilistic nature of operations due to lack of deterministic photon-photon interactions. This leads to prohibitive losses and resource overheads compared to other platforms with deterministic interactions [4–6]. Frequency encoding can harness low-loss, fiber-based and integrated photonic devices to significantly reduce scaling losses and experimental complexity of photonic QIP experiments. While frequency encoding

does not overcome the fundamental problem of probabilistic operations, it offers a path to scaling experiments such as boson sampling and cluster state generation with markedly reduced losses and resource overheads.

1.2 Dissertation outline and summary of results

In Section 2.1, we introduce the fundamentals including the nonlinear Schrödinger equation, coupled mode equations for BS-FWM and details of experimental implementation in a dispersion-shifted fiber. We theoretically analyze conditions under which the phase-matching is flexible. We show frequency conversion with 97%efficiency and ultra-low noise. We also demonstrate that the frequency separation between the input and target modes can be tuned by over 1 THz while maintaining the conversion efficiency at 95%. We solve the coupled mode equations for BS-FWM in the cw-limit and show that the evolution emulates a frequency beam splitter, the parameters of which can be tuned by controlling the power and relative phase of the two pumps.

Next, we study photon pair generation via nonlinear processes - spontaneous parametric down conversion (SPDC) and spontaneous four-wave mixing (SFWM) in $\chi^{(2)}$ and $\chi^{(3)}$ media respectively. We discuss phase-matching techniques for SPDC processes in $\chi^{(2)}$ crystals, including periodic poling. We discuss the photon statistics and joint spectro-temporal properties of the generated photons and their dependence on the spectral properties of the pump and the phase-matching conditions. We discuss cavity-enhanced SFWM in microresonators and show that these integrated single-photon sources are ideally suited for frequency domain applications discussed in this thesis. We discuss relevant aspects of microresonator dispersion engineering to achieve efficient photon pair generation over a sufficiently large bandwidth. We also discuss in detail techniques

to optimize the cavity and bus waveguide coupling conditions to maximize the photon pair generation rate. We also discuss the generation of spectrally pure single photons in microresonators.

In the final section of Section 2.1, we discuss techniques to characterize non-classical states of light, with a focus on phase-insensitive second-order coherence measurements. We also discuss heralding and post selection, which are used extensively in this thesis alongside photon coincidence measurements. We discuss state-of-the-art single-photon detection systems and time tagging. The experiments in this thesis did not use phase sensitive techniques such as homodyne and heterodyne measurements and references have been included in place of an extensive discussion on these methods.

In Chapter 3, we propose and demonstrate a frequency multiplexed single-photon source. Alternative schemes using spatial and temporal multiplexing suffer from increasing switching losses as a large number of modes are multiplexed, making deterministic operation challenging to achieve. In this work, we implement a frequency switching scheme based on BS-FWM that breaks this limitation. The losses in our switching scheme are constant irrespective of the number of multiplexed modes. We perform theoretical analysis to show clear advantage of this scheme over spatial and temporal mode multiplexing. We achieve a photon generation rate of 46 kHz, a coincidences-to-accidentals ratio of > 100 and an improved $g^{(2)}(0)$ of 0.07. We discuss the generation of pure, indistinguishable photons using SFWM in microresonators, and show that our scheme can achieve 50% efficiency with 10 multiplexed modes.

In Chapter 4 we demonstrate two-photon quantum interference with spectrally distinct photons generated from a microresonator. We use BS-FWM to implement an active "frequency beam splitter" (FBS) and achieve interference visibilities of 0.95 ± 0.02. The interfering photons are narrow in bandwidth (<300 MHz) but separated by 800 GHz,

and Bragg scattering renders them indistinguishable after interaction. We observe a rich interference pattern including quantum beating. Quantum interference between spectrally distinct photons is counterintuitive, as such photons do not interfere when overlapped on passive linear devices, such as beam-splitters. When a single photon is incident on one port of the FBS, the resulting output is a photon in an equal superposition of two colors; a bichromatic qubit. When two photons of distinct colors are incident on the two ports of this active device, quantum interference results in an output state where the two photons always exit from the same frequency arm. Our measurements confirm this bunched bichromatic output, with an interference visibility well above the classical limit. This work establishes four-wave mixing as a tool for selective high-fidelity two-photon operations in the frequency domain which, combined with integrated single-photon sources, provides a building block for frequency-multiplexed photonic quantum networks.

Finally, in Chapter 6, we demonstrate a single-photon time lens based on BS-FWM. A time lens draws on space time duality and imparts a quadratic phase on the input fields in the time domain. In the previous chapters, all interacting fields were spectrally narrow and all results could be explained in the cw-limit. However, the flexible phase-matching conditions allowed by our implementation of BS-FWM make it possible to realize efficient operations on broadband quantum pulses. We show that it is possible to temporally magnify (spectrally compress) single-photon level pulses with BS-FWM and demonstrate a time lens 2.2 picosecond resolution and a magnification factor of 158. Temporal modes that are broadband in frequency (such as 1D Hermite-Gaussian (HG) modes) have been shown to be a universal framework for photonic QIP. We propose and simulate a 1D HG temporal mode sorter by generalizing the phase imparted by the time lens. We use steepest gradient descent for numerical optimization and demonstrate sorting of 12 HG modes using a cascaded 4-stage scheme. This result shows that BS-

FWM can perform complex operations on picosecond-scale waveforms and can be used as a toolbox for temporal mode quantum processing.

CHAPTER 2

THE ESSENTIALS: BRAGG SCATTERING, SINGLE-PHOTON SOURCES AND MEASUREMENT OF QUANTUM STATES OF LIGHT

2.1 Quantum frequency translation via Bragg scattering four-wave mixing (BS-FWM)

Quantum frequency translation (QFT) is a process by which the central frequency of a photon wave packet is shifted while preserving all other properties of the photon [7]. In order to preserve all quantum properties of the input photon wavepacket, such as superposition and entanglement with other systems, QFT must be performed with unity efficiency without introducing any spurious noise [3]. A device that efficiently performs QFT can act as an interconnect between quantum systems that work in disparate frequency bands, such as quantum memories and telecom band photons. QFT is however can be exploited as a significantly more powerful toolbox with applications that go far beyond conventional interconnects. QFT can coherently couple and manipulate distinct frequency modes of light. This will be the central theme of this thesis.

QFT was first observed via sum/difference frequency generation mediated by $\chi^{(2)}$ nonlinearity in a $KTiOPO_4$ (KTP) crystal [7]. Energy conservation in such a process however requires that the frequency difference between the input and the target field be equal to that of the pump field. This necessarily induces a large frequency shift of the order of a few 10s of THz. Alternatively, four-wave mixing mediated by $\chi^{(3)}$ nonlinearity can be used to induce frequency shifts of the order of a few hundred GHz. In this work, we exploit a particular configuration of four wave mixing shown in Fig. 2.1. In this configuration, two strong classical pump fields (ω_{P1}, ω_{P2}) mediate the interaction

between two quantum fields (ω_R, ω_B) in a $\chi^{(3)}$ nonlinear medium. In contrast to other third-order processes such as degenerate FWM, which suffer from excess noise due to amplification of vacuum fluctuations, BS-FWM is a unitary process that preserves the number of photons in the quantum fields [8, 9]. A photon in mode ω_R is annihilated for every photon generated in the mode ω_B, and vice versa. Energy conservation necessitates that the frequency separation between the pumps $\Omega = \omega_{P1} - \omega_{P2}$ is equal to the energy separation between the two quantum fields, i.e $\omega_B - \omega_R = \Omega$. Flexible phase-matching conditions can be engineered by placing the pump fields and the single-photon fields symmetrically about the zero-dispersion wavelength of a $\chi^{(3)}$ material. Tunable frequency conversion can then be achieved by simply tuning the separation Ω between the two strong classical pump waves. These flexible phase matching conditions and tunability of the QFT process are crucial for several applications described in this thesis. This configuration also ensures that the classical pump fields are placed sufficiently far in frequency from the single-photon fields, making it easy to reject the pumps after the nonlinear interaction.

In this chapter, we will describe in detail the theory of quantum frequency translation via BS-FWM using coupled-mode equations. We will provide analytically solutions for the evolution of the quantum fields for the case where all interacting fields are narrow in frequency (cw-limit). We will also discuss the phase-matching conditions and regimes for which spurious side bands are suppressed, allowing for a two-mode unitary, beam-splitter like interaction. The more general case with pulsed pumps is discussed in the time lens chapter. We will then discuss the experimental implementation of this process in a commercial dispersion-shifted fiber. Finally, we will discuss implementations of BS-FWM on integrated photonic platforms.

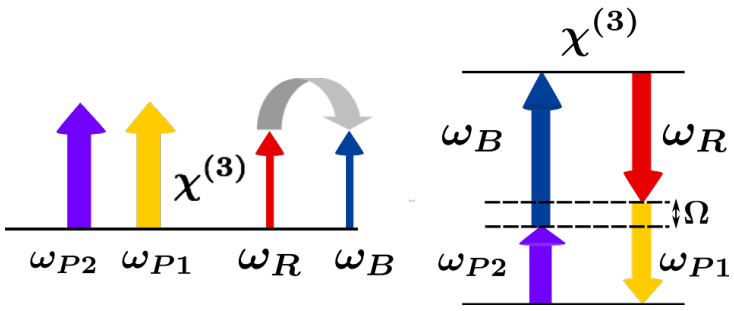

Figure 2.1: **Quantum frequency translation:** Bragg-scattering four-wave mixing (BS-FWM) (left) Two strong pumps ω_{P1}, ω_{P2} drive the interaction between two quantum-level fields ω_R, ω_B. (right) BS-FWM is a unitary process where a photon in the input mode (ω_R) is annihilated for each photon produced in the target mode (ω_B) and vice versa.

2.1.1 The nonlinear Schrödinger equation

We first derive the nonlinear Schrödinger equation (NLSE) starting from the propagation equation of an electromagnetic field $\boldsymbol{E}$ in a dielectric medium,

$$\nabla^2 \boldsymbol{E} - \frac{1}{c^2}\frac{\partial^2 \boldsymbol{E}}{\partial t^2} = \mu_0 \frac{\partial^2 \boldsymbol{P_L}}{\partial t^2} + \mu_0 \frac{\partial^2 \boldsymbol{P_{NL}}}{\partial t^2} \tag{2.1}$$

where $\boldsymbol{E} = \boldsymbol{E}(\boldsymbol{r}, t)$ is the space and time dependent electric field and we have separated the linear ($\boldsymbol{P_L}(\boldsymbol{r}, t)$) and nonlinear contributions ($\boldsymbol{P_{NL}}(\boldsymbol{r}, t)$) to the polarization induced in the medium. These components are related to the electric field via the linear and nonlinear susceptibilities. These susceptibilities are in general frequency dependent, and it is easiest to further simplify the linear part of 2.1 in the Fourier domain via the transformation,

$$\boldsymbol{E}(\boldsymbol{r}, t) = \int_{-\infty}^{\infty} \tilde{E}(\boldsymbol{r}, \omega - \omega_0) \exp -i(\omega - \omega_0) t d\omega \tag{2.2}$$

where we have eliminated the fast time dependence $\exp(i\omega_0 t)$ assuming that the bandwidth of the field $E(\boldsymbol{r}, t)$ is much smaller than the carrier frequency ω_0. Using the frequency dependent linear susceptibility, we can write a similar expression for the linear polarization,

$$\boldsymbol{P_L}(\boldsymbol{r}, \boldsymbol{t}) = \epsilon_0 \int_{-\infty}^{\infty} \chi^{(1)}(\omega) \tilde{E}(\boldsymbol{r}, \omega - \omega_0) \exp -i(\omega - \omega_0) t d\omega \tag{2.3}$$

Combining eqs. 2.2 and 2.3 with 2.1, we can simplify the linear part of the field propagation in the frequency domain,

$$\begin{aligned}&\nabla^2\tilde{E}(\boldsymbol{r},\omega-\omega_0)+\frac{\omega^2}{c^2}(1+\chi^{(1)}(\omega))\tilde{E}(\boldsymbol{r},\omega-\omega_0)\\&=\nabla^2\tilde{E}(\boldsymbol{r},\omega-\omega_0)+\left(\frac{\omega n(\omega)}{c}\right)^2\tilde{E}(\boldsymbol{r},\omega-\omega_0)\end{aligned}\tag{2.4}$$

where we have introduced the frequency dependent refractive index $n^2(\omega) = 1 + \chi^{(1)}(\omega)$. We can now define the frequency dependent propagation constant,

$$\beta(\omega) = \frac{n(\omega)\omega}{c}\tag{2.5}$$

For fields propagating in a waveguide (such as an optical fiber), it is reasonable to assume that $\frac{\partial^2 E}{\partial x^2}, \frac{\partial^2 E}{\partial y^2} \ll \frac{\partial^2 E}{\partial z^2}$, i.e diffraction of the optical mode negligible in all directions except the propagation direction (z). We now introduce the slowly varying amplitude $\tilde{A}(\omega - \omega_0)$ such that,

$$\tilde{E}(z,\omega-\omega_0) = \tilde{A}(z,\omega-\omega_0)\exp(i\beta_0 z)\tag{2.6}$$

where β_0 is the propagation constant at ω_0. We can now make the following simplifications,

$$\begin{aligned}&\frac{\partial^2\left(\tilde{A}\exp i\beta_0 z\right)}{\partial z^2}\\&=\frac{\partial}{\partial z}\left[\left(\frac{\partial\tilde{A}}{\partial z}+i\beta_0\tilde{A}\right)\exp i\beta_0 z\right]\\&=e^{i\beta_0 z}\left[\frac{\partial^2\tilde{A}}{\partial z^2}+2i\beta_0\frac{\partial\tilde{A}}{\partial z}-\beta_0^2\tilde{A}\right]\end{aligned}\tag{2.7}$$

Combining eqs. 2.4, 2.5, 2.6, 2.7 and using the slowly varying envelope approximation by neglecting $\frac{\partial^2 A}{\partial z^2}$ we obtain the simplified form for the linear part of the field

propagation in the frequency domain,

$$\begin{aligned} & e^{i\beta_0 z}\left[2i\beta_0\frac{\partial A}{\partial z} + A(\beta(\omega)^2 - \beta_0^2)\right] \\ & \approx 2\beta_0 e^{i\beta_0 z}\left[i\frac{\partial \tilde{A}}{\partial z} + (\beta(\omega) - \beta_0)\tilde{A}\right] \end{aligned} \tag{2.8}$$

where we have used the approximation

$$\beta(\omega)^2 - \beta_0^2 \approx 2\beta_0(\beta(\omega) - \beta_0) \tag{2.9}$$

The frequency dependent propagation constant $\beta(\omega)$ can be Taylor expanded around the carrier frequency ω_0 as,

$$\beta(\omega) = \beta_0 + \sum_{m=1}^{\infty} \frac{1}{m!}\frac{d^m\beta}{d\omega^m}\bigg|_{\omega=\omega_0} (\omega - \omega_0)^m \tag{2.10}$$

The first derivative of the propagation constant $\beta^{(1)}$ is equal to the inverse group velocity $v_g = \frac{\partial\omega}{\partial k}$ and the second derivative $\beta^{(2)}$ is known as the group velocity dispersion (GVD). In order to include the effects of the induced nonlinear polarization, we revert back to the time domain,

$$\tilde{A}(z,t) = \int_{-\infty}^{\infty} \tilde{A}(z, \omega - \omega_0)\exp(i(\omega - \omega_0)t)d\omega \tag{2.11}$$

Combining equations Equations (2.6), (2.8), (2.10) and (2.11) with Equation (2.1), we obtain,

$$2\beta_0 e^{i\beta_0 z}\left[i\frac{\partial}{\partial z} + \sum_{m=1}^{\infty}\frac{1}{m!}\frac{d^m\beta}{d\omega^m}\bigg|_{\omega=\omega_0}\left(i\frac{\partial}{\partial t}\right)^m\right]\tilde{A}(z,t) = \mu_0\frac{\partial^2 P_{NL}}{\partial t^2} \tag{2.12}$$

where we have eliminated the fast time dependence from the nonlinear polarization assuming $\boldsymbol{P}_{NL}(\boldsymbol{r},t) = P_{NL}(\boldsymbol{r},t)\exp(i\omega_0 t)$. In a medium with third order nonlinear susceptibility $\boldsymbol{\chi}^{(3)}$ we have the relation [10],

$$\boldsymbol{P}_{NL} = \epsilon_0 \boldsymbol{\chi}^{(3)} \vdots \boldsymbol{E}(\boldsymbol{r},t)\boldsymbol{E}(\boldsymbol{r},t)\boldsymbol{E}(\boldsymbol{r},t) \tag{2.13}$$

where $\boldsymbol{\chi}^{(3)}$ is in general a fourth-order tensor. Assuming all fields to be polarized in a single direction and restricting to terms in eq. 2.13 oscillating at ω_0, then we obtain,

$$P_{NL} = \frac{3}{4}\epsilon_0 \chi^{(3)} |E|^2 E \tag{2.14}$$

We make the co-ordinate transformation to a frame of reference propagating with the group velocity ($v_g = 1/\beta^{(1)}$) of the pulse,

$$\tau = t - \frac{z}{v_g} = t - \beta^{(1)} z \tag{2.15}$$

resulting in the following change of in the evaluation of the derivatives,

$$\begin{aligned} \frac{\partial \tilde{A}}{\partial z} &= \frac{\partial \tilde{A}}{\partial z} - \beta^{(1)} \frac{\partial \tilde{A}}{\partial \tau} \\ \frac{\partial \tilde{A}}{\partial t} &= \frac{\partial \tilde{A}}{\partial \tau} \end{aligned} \tag{2.16}$$

Combining Equations (2.14) and (2.16) with Equation (2.12) we obtain,

$$2\beta_0 \left[i\frac{\partial}{\partial z} + \sum_{m=2}^{\infty} \frac{1}{m!} \frac{d^m \beta}{d\omega^m}\bigg|_{\omega=\omega_0} \left(i\frac{\partial}{\partial \tau} \right)^m \right] \tilde{A}(z,\tau) = \frac{3}{4} \chi^{(3)} \frac{\omega_0^2}{c^2} |\tilde{A}(z,\tau)|^2 \tilde{A}(z,\tau)$$

which can be further simplified,

$$\left[i\frac{\partial}{\partial z} + \sum_{m=2}^{\infty} \frac{1}{m!} \frac{d^m \beta}{d\omega^m}\bigg|_{\omega=\omega_0} \left(i\frac{\partial}{\partial \tau} \right)^m \right] \tilde{A}(z,\tau) = \frac{3}{8} \chi^{(3)} \frac{\omega_0}{n(\omega_0) c} |\tilde{A}(z,\tau)|^2 \tilde{A}(z,\tau). \tag{2.17}$$

Finally, we can normalize the field amplitude $\tilde{A}(z,t)$ which has units of V/m using the transformation $|A'|^2 = \frac{1}{2}\epsilon_0 n c A_{eff} |\tilde{A}|^2$ such that $|A'|^2$ is proportional to the total optical power (units of W), we obtain,

$$\left[i\frac{\partial}{\partial z} + \sum_{m=2}^{\infty} \frac{1}{m!} \frac{d^m \beta}{d\omega^m}\bigg|_{\omega=\omega_0} \left(i\frac{\partial}{\partial \tau} \right)^m \right] \tilde{A}'(z,\tau) = \gamma |\tilde{A}'(z,\tau)|^2 \tilde{A}'(z,\tau)$$

or equivalently,

$$\left[i\frac{\partial}{\partial z} + \beta(i\partial_\tau) \right] \tilde{A}'(z,\tau) = \gamma |\tilde{A}'(z,\tau)|^2 \tilde{A}'(z,\tau) \tag{2.18}$$

with

$$\beta(i\partial_\tau, \omega_0) = \sum_{m=2}^{\infty} \frac{1}{m!} \frac{d^m\beta}{d\omega^m}\Big|_{\omega=\omega_0} \left(i\frac{\partial}{\partial\tau}\right)^m \tag{2.19}$$

where we have defined the constants $\bar{n}_2 = \frac{3}{8n}\chi^{(3)}$ and $\gamma = \left(\frac{2\bar{n}_2}{\epsilon_0 nc}\right)\frac{\omega_0}{cA_{eff}}$. The coefficient $n_2 = \frac{2\bar{n}_2}{\epsilon_0 nc}$ has units of $\frac{m^2}{W}$ and γ has units of $\frac{1}{mW}$. Eq. 2.18 is the nonlinear Schrödinger equation (NLSE).

2.1.2 Coupled mode equations for BS-FWM

We now derive the coupled mode equations for BS-FWM, starting with the NLSE 2.18. We consider four interacting fields with central carrier frequencies $\omega_{P1}, \omega_{P2}, \omega_R and \omega_B$ (see Figure 2.1. The total field $A(z,t)$ can be written as,

$$A(z,t) = \sum_j A_j(z,t)e^{i(\beta_j z - \omega_j t)} + c.c. \tag{2.20}$$

where $j \in (P1, P2, R, B)$ are denote the four interacting fields. Substituting the ansatz in eq. 2.20 into the NLSE 2.18 and separating the the terms oscillating at the 4 carrier frequencies, we obtain the following coupled mode equations for BS-FWM,

$$\begin{aligned}
\frac{\partial A_{P1}}{\partial z} &= i\beta(i\partial_t, \omega_{P1}) + i\gamma\left(|A_{P1}|^2 + 2|A_{P2}|^2\right)A_{P1} \\
\frac{\partial A_{P2}}{\partial z} &= i\beta(i\partial_t, \omega_{P2}) + i\gamma\left(|A_{P2}|^2 + 2|A_{P1}|^2\right)A_{P2} \\
\frac{\partial A_R}{\partial z} &= i\beta(i\partial_t, \omega_R) + i\gamma\left(2|A_{P1}|^2 + 2|A_{P2}|^2\right)A_R + 2i\gamma A^*_{P1}A_{P2}A_B \exp i\Delta k_L z \\
\frac{\partial A_B}{\partial z} &= i\beta(i\partial_t, \omega_B) + i\gamma\left(2|A_{P1}|^2 + 2|A_{P2}|^2\right)A_B + 2i\gamma A^*_{P2}A_{P1}A_R \exp -i\Delta k_L z
\end{aligned} \tag{2.21}$$

where $\Delta k_L = \beta_{P2} - \beta_{P1} + \beta_B - \beta_R$ is the (linear) phase mismatch. The second terms denote the self-phase and cross-phase modulation due to the strong pumps. In writing eq. 2.21,

we have ignored terms that are second order and higher in the weak-amplitude fields A_R and A_B. The dispersion terms $\beta(i\partial_t, :)$ are as defined in the in eq. 2.19. These terms reflect the dispersion of each of the pulses in the frame of reference of their respective carrier frequencies ($\omega_{P1}, \omega_{P2}, \omega_R$ and ω_B). This form of the dispersion in eq. 2.21 significantly simplifies numerical calculations using techniques such as the split step Fourier method (SSFM), as a single frequency mesh is sufficient to propagate pulses that are actually far separated in frequency [11].

In general when the four interacting fields are broadband in frequency (pulsed), eq. 2.21 cannot be solved analytically and numerical solutions are necessary. In the cw-limit however, a simple analytical solution can be found. In this limit, the dispersion terms in 2.21 are negligible and we can write

$$\begin{aligned}
\frac{\partial A_{P1}}{\partial z} &= i\gamma\left(|A_{P1}|^2 + 2|A_{P2}|^2\right)A_{P1} \\
\frac{\partial A_{P2}}{\partial z} &= i\gamma\left(|A_{P2}|^2 + 2|A_{P1}|^2\right)A_{P2} \\
\frac{\partial A_R}{\partial z} &= i\gamma\left(2|A_{P1}|^2 + 2|A_{P2}|^2\right)A_R + 2i\gamma A^*_{P1}A_{P2}A_B \exp i\Delta k_L z \\
\frac{\partial A_B}{\partial z} &= i\gamma\left(2|A_{P1}|^2 + 2|A_{P2}|^2\right)A_B + 2i\gamma A^*_{P2}A_{P1}A_R \exp -i\Delta k_L z
\end{aligned} \tag{2.22}$$

As the strong pumps A_{P1} and A_{P2} remain undepleted throughout the interaction, it is reasonable to assume that $|A_{P1}|^2, |A_{P2}|^2$ are constant. Then the pumps simply acquire a phase during the process due to self-phase and cross-phase modulation from the other strong pump and we can write,

$$\begin{aligned}
A_{P1}(z) &= A_{P1}(z=0) \exp i\gamma\left(|A_{P1}|^2 + 2|A_{P2}|^2\right)z \\
A_{P2}(z) &= A_{P2}(z=0) \exp i\gamma\left(|A_{P2}|^2 + 2|A_{P1}|^2\right)z
\end{aligned} \tag{2.23}$$

Using eqs 2.23 and using the transformations $\tilde{A}_R = \exp i\gamma\left(2|A_{P1}|^2 + 2|A_{P2}|^2\right)A_R$ $\tilde{A}_B =$

$\exp i\gamma\left(2|A_{P1}|^2 + 2|A_{P2}|^2\right)A_B$,

$$\begin{aligned}\frac{\partial \tilde{A}_R}{\partial z} &= 2i\gamma A^*_{P1}(z=0)A_{P2}(z=0)\tilde{A}_B \exp i\Delta k z \\ \frac{\partial \tilde{A}_B}{\partial z} &= 2i\gamma A^*_{P2}(z=0)A_{P1}(z=0)\tilde{A}_R \exp -i\Delta k z\end{aligned} \tag{2.24}$$

Where $\Delta k = \Delta k_L + \gamma(|A_{P1}|^2 - |A_{P1}|^2)$ is the total phase mismatch. These can be reduced to the second order differential equations,

$$\begin{aligned}\frac{\partial^2 \tilde{A}_R}{\partial z^2} &= i\Delta k \frac{\partial \tilde{A}_R}{\partial z} - \kappa^2 \tilde{A}_R \\ \frac{\partial^2 \tilde{A}_B}{\partial z^2} &= -i\Delta k \frac{\partial \tilde{A}_R}{\partial z} - \kappa^2 \tilde{A}_B\end{aligned} \tag{2.25}$$

where we have defined the complex coupling coefficient $\kappa = 2\gamma A^*_{P1}(z=0)A_{P2}(z=0)$. Equations 2.25 can be solved with the ansatz $\exp i\alpha_R z$ and $\exp i\alpha_B z$where the coefficients alpha satisfy,

$$\begin{aligned}-\alpha_R^2 &= -\Delta k \alpha_R - \kappa^2 \\ -\alpha_B^2 &= \Delta k \alpha_B - \kappa^2 \\ &\text{with solutions} \\ \alpha_R &= \frac{i\Delta k}{2} \pm \sqrt{\left(\frac{\Delta k}{2}\right)^2 + |\kappa|^2} \\ \alpha_B &= -\frac{i\Delta k}{2} \pm \sqrt{\left(\frac{\Delta k}{2}\right)^2 + |\kappa|^2}\end{aligned} \tag{2.26}$$

The solutions have the form

$$\begin{aligned}A_R(z) &= c_R^0 \exp i\alpha_R z + c_R^1 \exp -i\alpha_R z \\ A_B(z) &= c_B^0 \exp i\alpha_B z + c_B^1 \exp -i\alpha_B z\end{aligned} \tag{2.27}$$

The coefficients in 2.27 can be calculated in terms of the initial values and initial deriva-

tives (2.25). The final solutions have the form,

$$\begin{aligned} A_R(z) &= \mu(z)A_R(0) + \nu(z)A_B(0) \\ A_B(z) &= -\nu^*(z)A_R(0) + \mu^*(z)A_B(0) \\ \mu(z) &= \cos Kz - i\frac{\Delta k}{2K}\sin Kz \\ \nu(z) &= i\frac{\kappa}{K}\sin Kz \end{aligned} \tag{2.28}$$

where we have defined $K = \sqrt{\left(\frac{\Delta k}{2}\right)^2 + |\kappa|^2}$. The solutions 2.28 represent a beam-splitter-like two mode transformation. We identify the conversion efficiency as,

$$\eta(z) = \left|\frac{\kappa}{K}\sin Kz\right|^2 \tag{2.29}$$

When the total phase mismatch $\Delta k = 0$, the solutions complete conversion/depletion of the input fields occur when the interaction strength $\kappa L = \frac{\pi}{2}$. For non-zero phase mismatch, the interaction is still a unitary transformation with reduced efficiency. Although are derived for weak input fields A_R, A_B, the transformation is valid for quantized mode operators. BS-FWM can then act as frequency-domain beam splitter. We will exploit this fact to demonstrate two color Hong-Ou-Mandel interference in chapter 4.

2.1.3 Experimental implementation in dispersion-shifted fiber

We implement BS-FWM in a commercial dispersion-shifted fiber (DSF, Corning Vistacor). Our scheme is shown in Figure 2.3a. As seen from Equation (2.29), frequency conversion with unity efficiency can only obtained for a perfectly phase-matched process with $\Delta k = 0$. Phase-matching can be achieved by placing the pump fields and the quantum fields symmetrically about the zero dispersion point ($\beta^{(2)} = 0$) of the interaction medium (see Fig. 2.3b). The measured dispersion for the Corning Vistacor fiber is shown in 2.3b; the fiber has a zero-dispersion wavelength around 1.4 μm . The strong BS-FWM pumps

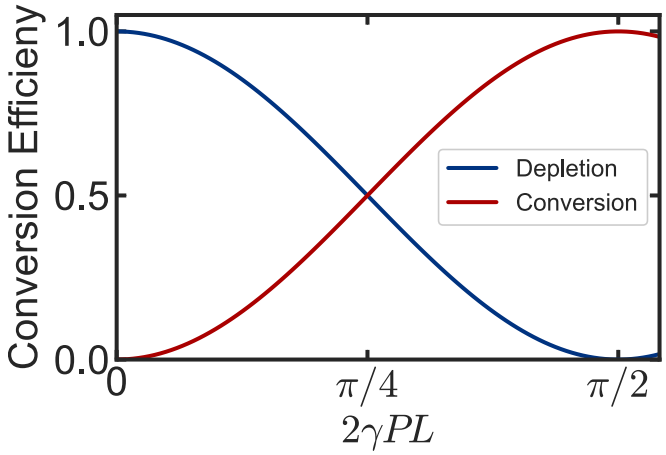

Figure 2.2: **Frequency conversion via BS-FWM:** For a perfectly phase-matched process, it is possible to achieve complete conversion of the input frequency mode (blue) to the target frequency mode (red). Optimal conversion occurs when the interaction strength $\kappa L = \pi/2$.

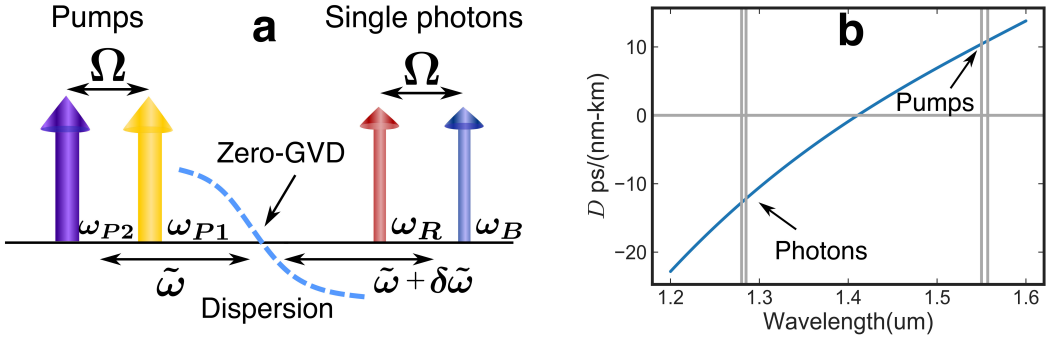

Figure 2.3: **BS-FWM in a dispersion-shifted fiber:** a) Two strong classical pumps (ω_{P1}, ω_{P2}) drive the interaction between two quantum fields (ω_R, ω_B). The frequency separation of the pumps Ω equals the frequency separation of the quantum fields. b) Measured dispersion of the dispersion-shifted fiber used in our implementation of BS-FWM. Phase-matching is achieved by symmetric placement of the pumps and the quantum fields about the zero-group velocity dispersion point (zero-GVD) of the medium. c) For a perfectly phase matched process, complete frequency conversion is achieved when the pump power is such that $2\gamma PL = \pi/2$. d) Measured BS-FWM acceptance bandwidth δ_{BS} for various pump frequency separations Ω. For $\Omega = 700$ GHz, the acceptance bandwidth δ_{BS} is measured to be 150 GHz. The conversion efficiency is maintained at 95% for pump separations as large as 1.7 THz, while the acceptance bandwidth is reduced by a factor of 2.

can then be placed in the C-band at 1.55 μm and the single photons can be placed in the O-band around 1.28 μm . This is experimentally convenient as erbium-doped fiber amplifiers (EDFAs) can be used to amplify the strong classical pumps in the C-band and commercial wavelength division multiplexers (WDMs) can be used to combine the photons and the pumps without adding significant loss to the path of the photons. The large frequency separation between the photons and the BS-FWM pumps makes it convenient to reject the strong pumps after the nonlinear interaction and ensure that BS-FWM acts as a low-noise frequency converter in the single-photon regime.

First, we derive an analytically expression for the phase-mismatch for our selected configuration. We note that for a given pump separation Ω and an input quantum field ω, energy conservation is satisfied for two translated sidebands $\omega + \Omega$ and $\omega - \Omega$. We show that due to effects of higher-order dispersion ($\beta^{(3)}$), it is possible to ensure that only a single sideband is phase-matched. This results in a two-mode interaction without spurious sidebands. The total phase mismatch for the process shown Fig. 2.3 is given as,

$$\Delta k = \beta(\omega_{P1}) - \beta(\omega_{P2}) + \beta(\omega_R) - \beta(\omega_B), \tag{2.30}$$

where β is the propagation constant for each frequency mode [12]. The nonlinear contribution to phase the mismatch vanishes when the two BS-FWM pumps have the same power ($P_1 = P_2$), which is the case in our implementation [12]. For convenience, we introduce the average frequency $\tilde{\omega} = \omega_{ZGVD} - (\omega_{P1} + \omega_{P2})/2$ and the frequency offset $\delta\tilde{\omega}$, where ω_{ZGVD} is the zero-dispersion point of the interaction medium (see Fig. 2.3b). Expanding Eq. 2.30 about the zero-dispersion point, we obtain,

$$\Delta k = \frac{\beta^{(3)}}{6}\left[\left(-\tilde{\omega} + \frac{\Omega}{2}\right)^3 - \left(-\tilde{\omega} - \frac{\Omega}{2}\right)^3 + \left(\tilde{\omega} + \delta\tilde{\omega} - \frac{\Omega}{2}\right)^3 - \left(\tilde{\omega} + \delta\tilde{\omega} + \frac{\Omega}{2}\right)^3\right] + O(\beta^{(4)}). \tag{2.31}$$

This readily simplifies to,

$$\Delta k = \frac{\beta^{(3)}}{2} [\delta\tilde{\omega}\Omega(\delta\tilde{\omega} + 2\tilde{\omega})] + O(\beta^{(4)}) \tag{2.32}$$

which indicates that it is always possible to obtain $\Delta k = 0$ at a specific input/target frequency where $\delta\tilde{\omega} = 0$. However, the BS-FWM acceptance bandwidth δ_{BS} is evidently dependent on $\beta^{(3)}$. Moreoever, as long as the frequency separation of the pumps is much larger than this bandwidth ($\Omega \gg \delta_{BS}$), it is ensured that only one sideband remains phasematched.

The detailed BS-FWM setup is shown in Figure 2.4. Photons from a single-photon source/attenuated coherent laser light in the input frequency mode are combined with the BS-FWM pumps using a C/O dual band WDM. The BS-FWM pumps are sourced from tunable C-band external cavity diode lasers (ECDLs, Agilent, Ando). Alternatively, temperature stabilized distributed feedback (DFB) diode lasers can also be used to get highly efficient frequency conversion. However, for applications that require stability of the pump frequency for extended durations (such as in Chapter 4), we found the wavelength stability and repeatability of the ECDL to be particularly useful. With better thermal control and environmental isolation, it is likely that the DFB lasers can be stabilized for extended durations making the setup significantly more cost effective. The cw-pumps are modulated using electro-optic modulators (EOMs) to carve out 10 ns pulses with a 1 MHz that are first pre-amplified and then amplified to a peak power of about 10 W using a Keopsys EDFA. The nonlinear parameter γ for the Vistacor fiber is about $3/(\text{W km})$ and a 100 m fiber spool suffices to achieve an interaction strength of $\pi/2$. We note that the EOM modulation extinction must be carefully optimized using the input polarization and the bias voltage in order to minimize the DC power at the input of the amplifiers, as a large DC level saturates the amplifiers and prevents the pumps from reaching the necessary peak power for optimal frequency conversion. The fiber spool is dipped in liquid nitrogen in order to eliminate Raman noise (see Figure 2.5). The strain

and temperature changes in the fiber due to liquid nitrogen change the fiber dispersion and therefore the optimal conversion wavelength. The dispersion shown in Figure 2.3b was measured while the fiber was cooled. After the nonlinear interaction, another C/O dual band WDM is used to reject the strong 1.55 μm pumps. The single-photons are sent through a free-space filtering setup consisting of a blazed grating (blaze wavelength 1.25 μm) with 0.5 nm bandwidth. This filtering eliminates broadband noise in the 1.3μm to 1.48 μm band generated in the EDFAs used to amplify the pumps and/or due to Raman scattering in the small part of the Vistacor that is outside the liquid nitrogen dewar and not cooled. The photons are then detected using superconducting nanowire single-photon detectors (SNSPDs). The rejected pumps are monitored after selecting for polarization using a combination of quarter and half-wave plates and a polarizing beam splitter (PBS) and monitored on a photodiode (1GHz bandwidth). Optimizing the polarization of all interacting fields is crucial for observing frequency conversion with > 90% conversion efficiency. We use the fact that the SNSPDs have optimal detection efficiency for a certain input polarization in an iterative optimization procedure. The polarization of the input photons is set to match the SNSPD optimal polarization. We then monitor the depletion of the input signal on the SNSPDs and optimize the polarization of the BS-FWM pumps after the first stage of amplification to get maximum possible depletion. After optimization, the quarter and half-wave plates monitoring the rejected pumps are rotated to get maximum transmission through the PBS. This serves as a polarization reference for the next several hours.

Figure 2.5 shows the dominant noise sources in this implementation of BS-FWM [13]. Spontaneous pair production (purple curve Figure 2.5) originates from a modulation instability type process ($\omega_{P1} + \omega_{P2} = \omega_S + \omega_I$). The gain curve for this process however rapidly drops for large detuning from the strong pumps. The other dominant source of noise near 1.3 μm is the anti-Stokes Raman scattering. The relative strength stokes and

anti-stokes Raman scattering is strongly temperature dependent on temperature. For an input frequency ω_0, the stokes and anti-stokes frequencies are given as $\omega_0 - \omega_S$ and $\omega_0 + \omega_S$ respectively. In this case, the phonon occupation for the excited state is lower by a factor $\exp -\frac{\hbar\omega_S}{k_B T}$ assuming Boltzmann statistics, and at low-temperatures the strength of the anti-stokes scattering is significantly lower compared to the stokes scattering [14]. In order to exploit this strong temperature dependence of anti-stokes scattering, we cool the fiber using liquid nitrogen and achieve significant noise reduction (6 orders of magnitude, see Figure 2.5). The total noise contribution in this configuration is less than 10^{-5} photons per BS-FWM pump pulse, making it suitable for use with single-photon states as input. This completes our analysis of the dominant noise sources in the frequency conversion process.

Figure 2.6a shows our measured frequency conversion efficiency as a function of the BS-FWM pump power for a pump frequency separation Ω = 700 GHz. We observe more than 97% conversion efficiency using a weak, coherent state as the input. The measured conversion efficiency matches well with theory (Equation (2.29). This suggests that the experimental implementation indeed matches a two-mode interaction without spurious nonlinear processes degrading the coherence of the process. Figure 2.6b shows the conversion efficiency as the frequency separation Ω between the input and target photons is tuned all the way to 1.7 THz. We see that the conversion efficiency is maintained at >95%. This measurement was made by detuning the lower frequency pump ω_{P2} in steps of 200 GHz while changing ω_{P1} by < 10 GHz in order to maintain the target frequency mode to be the same throughout the measurement. The high conversion efficiency for this large tuning is a result of the flexible phase matching conditions used in our implementation of BS-FWM. This tunability is extremely crucial for all applications described in this thesis. We note that the acceptance bandwidth reduces due to effects of higher-order dispersion as the detuning Ω becomes large, as predicted theoretically

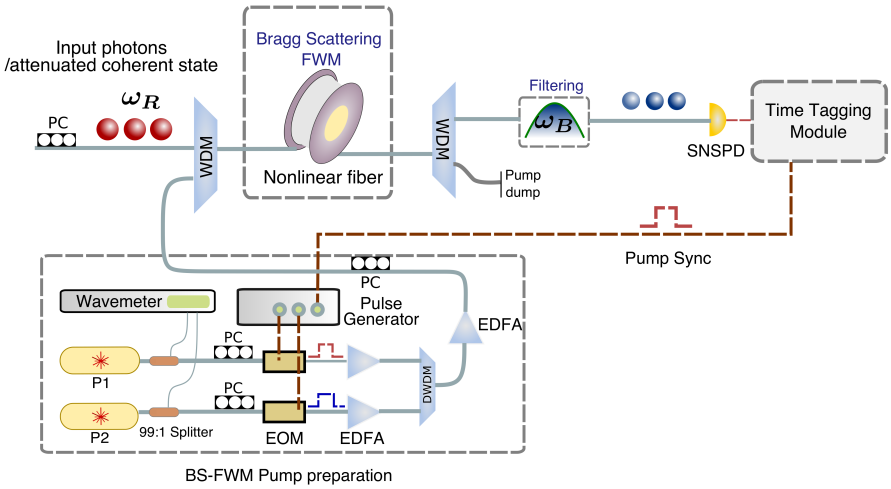

Figure 2.4: **BS-FWM experimental setup** Photons from a single-photon source or a weak coherent input state in the input frequency mode (ω_R) is combined combined with the strong pumps and sent to a spool of dispersion shifted fiber (DSF) for the nonlinear interaction. The DSF spool is cooled using liquid nitrogen to eliminate noise from anti-stokes spontaneous raman scattering. Two external cavity diode lasers are intensity modulated to carve out 10 ns pulses. The pumps are pre-amplified to the level of 5 mW and then amplified to 10 W peak power before being combined with the photons using a C/O dual band WDM. The wavelengths of the pumps are monitored on a wavemeter compensate for drifts. The polarization of all interacting fields is carefully optimized to get maximum depletion of the input signal. The strong pumps are rejected using another dual band WDM and a narrow free-space grating filter is used to extract photons centered around an 0.5 nm bandwidth about the target frequency (ω_B). The photons are detected using superconducting nanowrire single-photon detectors.

(Equation (2.32)). For $\Omega = 700$ GHz, the acceptance bandwidth δ_{BS} is measured to be 150 GHz and this bandwidth is reduced by a factor of 2 to about 80 GHz for a detuning of 1.7 THz.

2.2 Parametric single-photon sources

Efficient sources of single and entangled photons are an essential ingredient for all photonic QIP experiments. The earliest sources of single photons were based on cold atomic clouds and were used for pioneering experiments in quantum informtion such as

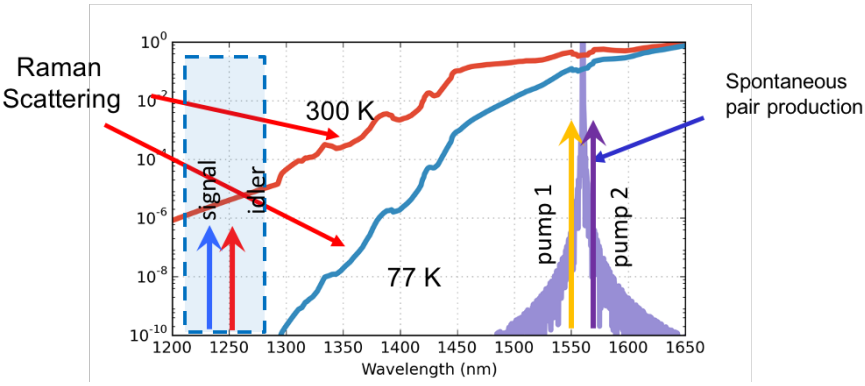

Figure 2.5: **Characterization of noise sources:**The dominant noise sources in our implementation of BS-FWM are spontaneous pair production/modulation instability (purple) and anti-stokes raman scattering (red and blue). The gain profile for spontaneous pair production drops off rapidly for large detuning. We exploit the strong temperature dependence of anti-Stokes Raman scattering and eliminate noise from this source by cooling the fiber using liquid nitrogen.

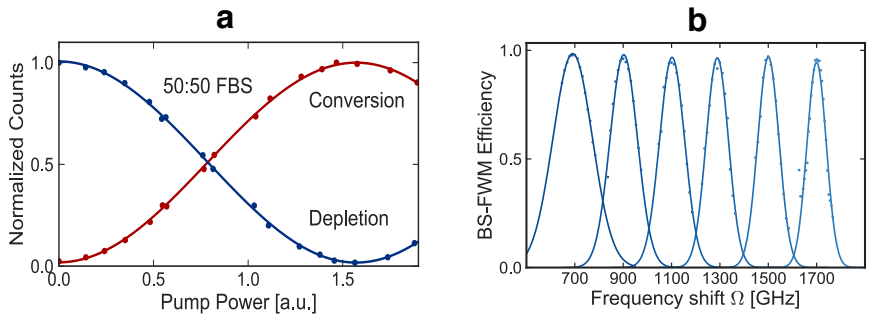

Figure 2.6: **Measured BS-FWM frequency conversion efficiency:**a) Conversion efficiency as a function of pump power for pump separation $\Omega = 700$ GHz. We observe 97% conversion efficiency with an attenuated coherent state as the input. b) Conversion efficiency as the pump detuning is increased up tp 1.7 THz. The conversion efficiency is maintained at $> 95\%$ while the acceptance bandwidth reduces by a factor of 2 due to effects of higher order dispersion.

verification of the Bell inequality and confirmation of violations of local hidden variable theories [15]. In these early experiments, pairs of correlated photons generated from cascaded photon emission from atomic systems were deployed. These setups however required vacuum chambers and suffered from low collection efficiencies. An alternative source of photon pairs based on spontaneous scattering of light in nonlinear media with

$\chi^{(2)}$ or $\chi^{(3)}$ susceptibilities was first proposed and observed in 1967 [16, 17]. These sources of correlated photons were based on *parametric nonlinear processes* such as downconversion ($\chi^{(2)}$) and four-wave mixing ($\chi^{(3)}$) and enabled several experimental breakthroughs in quantum optics, including two-photon Hong-Ou-Mandel (HOM) interference and the generation of squeezed light [18, 19]. Another pioneering experiment in 1995 enabled the direct generation of bright, polarization entangled photon pairs using type-II phase-matched parametric downconversion [20]. These demonstrations of entanglement have since been extended to path, frequency, time and spatial mode entanglement [21–23].

Parametric single-photon sources have several advantages that make them particularly useful for experimental applications. These sources operate at room temperature and can be implemented in a wide range of materials including integrated photonics platforms. These spectra and bandwidth of these sources can be tailor-made for specific target applications in different frequency regimes. Efficient SPDC sources in the infrared have been demonstrated [24, 25]. Single-photon detectors with > 95% quantum efficiency at 1.55 μm are now commercially available. Sources of single-photons based on atoms and artificial atoms (two-level systems) in solid-state platforms lack wavelength tunability and primarily function in the visible and near-infrared. Despite the tremendous progress in optimizing these sources, deterministic generation of single-photons using nonlinear processes is still an unsolved technological challenge. Spontaneous parametric processes are fundamentally probabilistic with a maximum theoretical efficiency of 25%. This fundamental limitation can be overcome by active feed-forward switching and multiplexing of single photons. We will discuss spectral multiplexing in chapter 3. The experiment described in chapter 3 uses an SPDC source implemented with periodically poled lithium niobate (PPLN). In the first section of this chapter, we will discuss the theory of SPDC and experimental implementation to generate heralded single photons at 1.28 μm . Next,

we will discuss spontaneous four-wave mixing (SFWM) in integrated microresonators. A source of frequency-entangled photons based on such cavity-enhanced SFWM for demonstrating frequency-domain HOM interference in chapter 4.

2.2.1 Spontaneous parametric down conversion (SPDC)

Parametric downconversion is the process by which a pump photon ω_P from a strong pump in a medium with second-order nonlinearity ($\chi^{(2)}$) spontaneously decays to two photons of lower frequency such that $\omega_P = \omega_S + \omega_I$. The process can be phenomenologically described as follows: in the presence of the strong pump ω_P and vacuum fluctuations in one of the photon field modes say ω_S, a nonlinear polarization is induced at ω_I in the medium [16]. The brightness of the spontaneous emission is maximum for ω_S, ω_I such that the phase matching condition $\boldsymbol{k}(\omega_P) = \boldsymbol{k}(\omega_S) + \boldsymbol{k}(\omega_I)$ is satisfied.

The Hamiltonian this process can be written as [26],

$$\hat{H}_{PDC} \propto \int_{-L/2}^{L/2} \chi^{(2)} \hat{E}_P^{(+)}(z,t) \hat{E}_S^{(-)}(z,t) \hat{E}_I^{(-)}(z,t) + h.c. \tag{2.33}$$

were the subscripts (P, S, I) denote the three interacting fields. The electric fields $\hat{E}_S, \hat{E}_I$ are related to the quantized creation/annihilation operators as,

$$\hat{E}^{(-)}(z,t) \propto \int d\omega \exp\left(-ik(\omega)z + i\omega t\right) \hat{a}^{\dagger}(\omega) \tag{2.34}$$

where the integral is over the bandwidth of each field and we have assumed collinear propagation in the z-direction. For sufficiently weak nonlinearity, the pump $\hat{E}_P$ can be treated classically,

$$\hat{E}_P^{(+)}(z,t) \propto \int d\omega \exp\left(ik(\omega_P)z - i\omega_P t\right) \alpha(\omega_P) \tag{2.35}$$

where $\alpha(\omega_P)$ is the pump pulse envelope. Then the Hamiltonian Equation (2.36) can be written as,

$$\hat{H}_{PDC} \propto \int_{-L/2}^{L/2} dz \int d\omega_P \int d\omega_S \int d\omega_I \chi^{(2)} \hat{E}_P^{(+)}(\omega_P)\hat{a}_S^\dagger(\omega_S)\hat{a}_I^\dagger(\omega_I) \exp\left[i(\omega_S + \omega_I - \omega_P)\right] \exp\left(i\Delta k z\right) + h.c. \tag{2.36}$$

where Δk is the phase mismatch. The output state can be calculated based on the evolution of the Hamiltonian,

$$\hat{U} = \exp\left(-\frac{i}{\hbar}\int \hat{H}_{PDC}(t)dt\right) \qquad |\psi\rangle_{PDC} = \hat{U}|0_S, 0_I\rangle \tag{2.37}$$

The time domain integral imposes energy conservation and evaluates to a delta function $\delta(\omega_S + \omega_I - \omega_P)$ [26]. The integral over the length of the crystal evaluates to,

$$\int_{-L/2}^{L/2} \exp(i\Delta k z) = \frac{\sin \Delta k L/2}{\Delta k} = \frac{L}{2}\mathrm{sinc}(\Delta k L/2) \tag{2.38}$$

Combining these equations,

$$\hat{U} = \exp\left(\frac{-iC}{\hbar}\int d\omega_I \int d\omega_S \ \alpha(\omega_S + \omega_I)\Theta(\omega_S, \omega_I)\hat{a}_S^\dagger(\omega_S)\hat{a}_I^\dagger(\omega_I)\right) \tag{2.39}$$

where C is a constant proportional to the length L of the crystal and the nonlinearity $\chi^{(2)}$ of the interaction medium and we have defined the phase-matching function

$$\Theta(\omega_S, \omega_I) = \mathrm{sinc}(\Delta k L/2) \tag{2.40}$$

The joint spectral amplitude (JSA) of the photons can be identified from,

$$\phi(\omega_S, \omega_I) = \alpha(\omega_S + \omega_I)\Theta(\omega_S, \omega_I) \tag{2.41}$$

The JSA of the photons determines the extent of correlation between the generated photon pairs and can be engineered by shaping the pump pulse and the phase-matching/acceptance bandwidth of downconversion process. A factorizable JSA such that $\phi(\omega_S, \omega_I) = f(\omega_S)g(\omega_I)$ results in the production of photons in "pure" spectro-temporal modes. The extent of correlations for non-factorizable states can be determined by calculating the Schmidt decomposition of Equation (4.9) [27].

Equation (2.39) can be fully integrated for the case where both photons are in a single spectral spectral mode. In this case the output is a two-mode squeezed state [28].

$$|\psi\rangle_{PDC} = \exp[r\hat{a}_S^\dagger \hat{a}_I^\dagger - r\hat{a}_S \hat{a}_I]|0_S, 0_I\rangle \tag{2.42}$$

Where r is proportional to the length of the crystal, the nonlinearity and pump amplitude. In the limit of low squeezing, the solution in the fock-state basis looks like,

$$|\psi\rangle_{PDC} = \sqrt{1 - |\zeta|^2} \sum_{n=0}^{\infty} \zeta^n |n_S, n_I\rangle \tag{2.43}$$

where $\zeta = \tanh(r)$ is the squeezing parameter. It is evident from Equation (2.43) that photon pairs are always generated in pairs in SPDC. The presence of one or more photons in one of the modes heralds the presence of photon(s) in the other mode. The maximum probability of generating a single-photon is 25% for a squeezing parameter of $|\zeta|^2 = 0.5$. We will discuss how to overcome this intrinsic limitation of SPDC sources in Chapter 3. In the next section, we discuss techniques for phase-matching the SPDC process in $\chi^{(2)}$ crystals.

2.2.2 Phase-matching considerations for down conversion processes

Here, we briefly discuss two phase matching techniques for down conversion processes: birefringent phase matching and quasi-phase matching in periodically poled crystals. In the two single-photon sources built over the course of this work used periodically-poled lithium niobate as the nonlinear material. However, SPDC in birefringent crystals is one of the most common techniques to generate polarization entangled photon pairs.

Assuming a collinear SPDC process, the phase matching condition $\Delta k = 0$ can be written as,

$$\frac{n(\omega_S)\omega_S}{c} + \frac{n(\omega_I)\omega_I}{c} = \frac{n(\omega_P)\omega_P}{c} \tag{2.44}$$

For a crystal with normal dispersion, it is not possible to satisfy Equation (2.44) [29]. This can be easily seen for the case of degenerate SPDC, where the phase-matching condition reduces to $n(\omega_P/2) = n(\omega_P)$ which cannot be satisfied if the refractive index is monotonically increasing. An alternative technique to achieve phase-matching is to use the birefringence of $\chi^(2)$ crystals. For uniaxial birefringent crystals, light polarized in the plane of the optic axis and the propagation direction $\boldsymbol{k}$ (”extraordinary polarization”) sees a refractive index $n_e(\theta)$ that is dependent on the angle θ between the propagation vector and optic axis of the crystal.

$$\frac{1}{n_e(\theta)^2} = \frac{\sin^2\theta}{\bar{n}_e^2} + \frac{\cos^2\theta}{n_o^2} \tag{2.45}$$

The choice of polarization for each of the three interacting fields depends the type of the crystal. For instance, for a negative uniaxial crystal ($n_e < n_o$), a Type-I phase matched process can be realized by polarizing ω_P along the extraordinary direction $n_e(\omega_P, \theta) = n_o(\omega_P/2)$. However, a major problem disadvantage of this scheme is the spatial overlap of the interacting fields reduces the angle θ becomes large [29]. This

problem can be resolved with quasi-phase matching in periodically poled crystals as discussed below.

A periodically poled $\chi^{(2)}$ crystal consists of alternating domains with modified crystal orientation such that the effective second order nonlinear coefficient d_{eff} has alternating signs. Here, d_{eff} is the relevant component of the third order tensor $\chi^{(2)}_{ijk}$ depending on the direction of propagation and polarizations of the interacting fields [29]. This alternating sign of d_{eff} can compensate for the linear phase mismatch, resulting in a quasi phase-matched process. This scheme has several advantages over birefringent phase matching. This scheme allows to phase match processes with co-propagating and co-polarized beams, resulting in maximum spatial overlap over the entire interaction length. Morever, the co-polarized scheme allows access to the highest nonlinear coefficient d_{33}, resulting in a more efficient nonlinear process. If the poling period is Λ, the Fourier series for the nonlinear coefficient has components $d_m \exp ik_m z$ where $k_m = 2\pi m/\Lambda$ and $d_m = 2/(m\pi)\sin(m\pi/2)$. Considering the largest Fourier coefficienct ($m = 1$), the effective phase mismatch can be written as [29],

$$\Delta k_Q = k(\omega_S) + k(\omega_I) - k(\omega_P) - 2\pi/\Lambda \tag{2.46}$$

The optimal poling period is twice the coherence length of the original process,

$$\Lambda = 2\pi/(k(\omega_S) + k(\omega_I) - k(\omega_P)) \tag{2.47}$$

This can be interpreted as a change in sign of the nonlinear coefficient before the field amplitude built up in the crystal starts to decrease due to the phase-mismatch. As we will see in Chapter 3, in addition to the poling period, thermal tuning of the temperature of the nonlinear crystal provides significant tunability to the SPDC process over a range of wavelengths. We will show details of these calculations in Chapter 3.

2.2.3 Spontaneous four wave mixing (SFWM)

In this section, we will discuss photon pair generation in $\chi^{(3)}$ media via spontaneous four-wave mixing (SFWM). $\chi^{(2)}$ nonlinearity is only available in a restricted set of materials due to symmetry considerations. $\chi^{(3)}$ nonlinearity on the other hand is ubiquitous and present in a range of materials and platforms, including photonic crystal fibers and integrated waveguides and microresonators [30]. Integrated photon sources have a compact footprint and several identical sources can be integrated on a monolithic platform. Dispersion engineering in integrated devices for a range of wavelengths results in flexible phase matching conditions and allows for precise control of the spectra and correlations of the generated photons. In $\chi^{(2)}$ processes, the pump is typically placed in the visible/near-visible and the generated photons are in the near-IR/IR. SFWM on the other hand involves a pump frequency which is closely spaced in frequency with the photons. This allows for the generation of IR-photons with IR-pumps and provides access to a wide range of fiber-based telecommunication tools such as WDMs. These can be used for low-loss filtering and for separating the photons into narrow frequency modes, which is required for frequency-domain applications. Photon pairs generated in discrete, narrow frequency bands via cavity enhanced SFWM are particularly well-suited for applications described in this thesis. For this reason, we use a silicon nitride microresonator as a photon pair source to demonstrate frequency-domain HOM interference (Chapter 4).

SFWM is the process where two pump photons ω_{P1}, ω_{P2} combine and decay to two photons ω_S, ω_I such that $2\omega_P = \omega_S + \omega_I$. Here, we consider SFWM with a single pump ($\omega_{P1} = \omega_{P2} = \omega_P$). The phase-mismatch for this process can be calculated from the coupled mode equations,

$$\begin{aligned} \Delta k &= \Delta k_L + \Delta k_{NL} \\ \Delta k_L &= \beta_S + \beta_I - 2\beta_P \\ \Delta k_{NL} &= 2\gamma P_0 \end{aligned} \tag{2.48}$$

where Δk and Δk_{NL} are the linear and nonlinear contributions to the phase-mismatch respectively and $\beta_{P,S,I}$ are the propagation constant at each of the three interacting fields. The linear phase mismatch Δk_L can be simplified by using the Taylor expansion of the propagation constant as in Equation (2.10) around the pump frequency ω_P. The first term corresponding corresponding to group velocity mismatch vanishes due to energy conservation. If $|\omega_{I/S} - \omega_P| = \Omega$, then the linear phase mismatch is $2\beta_P^{(2)}\Omega^2$. The total phase-mismatch can then be simplified to,

$$\Delta k = 2\beta_P^{(2)}\Omega^2 + 2\gamma P_0 \tag{2.49}$$

For efficient spontaneous four-wave mixing, the phase-mismatch in Equation (2.49) must be small. We note that for optical parametric oscillation (OPO) over large bandwidths Ω for applications such as frequency comb generation, this condition is typically satisfied by ensuring anomalous group velocity dispersion ($\beta_P^{(2)} < 0$). This is necessary as the pump power P_0 must be above the OPO threshold, resulting in significant contribution to the nonlinear phase mismatch. On the other hand, for spontaneous processes the pump power used is a fraction of the OPO threshold ensuring that the nonlinear phase mismatch is relatively small. Thus ensuring that $\beta_P^{(2)}$ is small is sufficient to for efficient photon pair generation over reasonable bandwidths [30–32]. Single-mode SFWM produces photons in a two-mode squeezed state with a fock-state distribution similar to Equation (2.43). In crucial distinction, the photon pair generation rate scales as squared of the total interaction strength γPL [30, 31]. The SFWM photon pair source used in this thesis is a silicon nitride microresonator pumped at 1.28 μm where photon pairs are generated over

a bandwidth of less than 5 THz and dispersion is readily engineered by modifying the waveguide geometry. We discuss SFWM in microcavities in the next section.

2.2.4 SFWM in silicon nitride microresonators

Silicon nitride for quantum photonics

Silicon nitride has emerged as a leading integrated photonic platform for nonlinear optics. Si_3N_4 has a broad transparency window from 0.4 - 3 μm , a higher refractive index than glass ($n = 2$) resulting in tight confinement and smaller effective mode area [33]. Si_3N_4 does not suffer from nonlinear loss (two-photon absorption, TPA) in the infrared (IR) due to its high bandgap, which is a detrimental effect for quantum and nonlinear applications with low bandgap materials such as silicon. Even though the nonlinear refractive index for Si_3N_4 ($n_2 = 2.5 \times 10^{-19}$) is an order of magnitude lower than silicon, the demonstrated linear loss for Si_3N_4 waveguides is significantly lower. Finally, in all single-photon level measurements done in our lab so far, we have not seen evidence of noise due to Raman scattering. Moreover, Si_3N_4 waveguides can be engineered to feature strongly anomalous dispersion in the infrared from 1.3 - 1.5 μm even though the material dispersion is strongly normal. All these properties combined make Si_3N_4 an ideal platform for integrated quantum and nonlinear photonics in the IR region.

Si_3N_4 microresonators

Single-photon sources based on high quality-factor microresonators are extremely well-suited for frequency domain applications. These sources can be used to generate photon

pairs in narrow-band, equally spaced frequency bins with a effectively discrete JSA. The spectral correlations of the photons can be controlled by modifying the spectral shape of the pump relative to the linewidth of resonator. The use of high quality factor resonator also allows for high photon flux rate with relatively low input pump power, which greatly simplifies pump rejection and other sources of noise at frequency of the photons. The intrinsic quality factor of a ring resonator is independent of it's length and is given as,

$$Q_i = \frac{2\pi n_g}{\lambda \alpha} \tag{2.50}$$

where n_g is the group index, λ is the wavelength and α is the loss per unit length (i.e. the loss factor after propagation by length L is $1 - \exp -\alpha L$. Si_3N_4 waveguides and ring resonators fabricated by the Lipson nanophotonics group at the Cornell Nanoscale facility now feature low to ultra-low propagation loss ranging from 5 dB/m to 0.8 dB/m corresponding to intrinsic quality factors of 5 million to 37 million at 1550 nm depending on the details of the fabrication procedure [34]. These improvements in fabrication loss and corresponding quality factors were due to modifications to the fabrication processes such as chemical mechanical polishing to improve top surface roughness [34]. The linewidth Δf of the resonator is related to it's quality factor as,

$$Q_L = f/\Delta f \tag{2.51}$$

where Q_L is the loaded quality factor. The loaded quality factor includes contributions from both intrinsic losses (α) and from the coupling of the resonator to the bus waveguide κ.

$$\frac{1}{Q_L} = \frac{1}{Q_i} + \frac{1}{Q_c} \tag{2.52}$$

where Q_c corresponds to the coupling quality factor. At critical coupling, $Q_c = Q_i$ and bus waveguide coupling coefficient is $\kappa_{critical} = 1 - \exp(-\alpha L)$ where $L = 2\pi R$ is the length of the resonator. This condition corresponds to the bus waveguide coupling coefficient

to be exactly equal to the intrinsic loss of the resonator. The coupling quality factor Q_c for an arbitrary coupling coefficient κ can be calculated as $Q_c = Q_i \times \frac{\kappa_{critical}}{\kappa}$. The loaded quality factor can be directly measured in experiments by measuring the transmission of a weak probe at the resonance. In general, the dependence of the transmission on the coupling condition is given as [35],

$$T(\lambda_{res}) = \left[\frac{t-\beta}{1-t\beta}\right]^2 \tag{2.53}$$

where $t = \sqrt{1-\kappa}$ and $\beta = \exp(-\alpha L/2)$. From Equation (2.53), it can be seen that the transmission goes to zero at critical coupling. Phase measurements can be used to determine if a given resonator is overcoupled or undercoupled for a given transmission dip [36]. Successive resonances of a microresonator are separated by the free-spectral range (Δnu_{FSR}) with is primarily dependent on the length L of the resonator,

$$\Delta\nu_{FSR} = \frac{c}{n_g(\lambda_{res})L} \tag{2.54}$$

where $n_g(\lambda_{res})$ is the group index at the resonance wavelength and is related to the effective waveguide index as $n_g = n_{eff} - \lambda\frac{dn_{eff}}{d\lambda}$. Finite element modeling software such as COMSOL Multiphysics can be used to directly calculate the effective waveguide index n_{eff} for a given waveguide dimension and Sellmeir equations for Si_3N_4 and for the cladding material SiO_2.

Photon pair generation in microresonators

The theory of spontaneous four wave mixing in microresonator cavities has been analyzed in several works [37–40]. Here, we discuss the how the device design, in particular the coupling condition of the pump and photon fields determine the photon pair generation and heralding rate. We also discuss the spectral correlations of the generated photon pairs and how they can be modified by engineering the spectro-temporal shape of the pump

and the coupling conditions to achieve > 99% spectral purity. Vernon et al. have shown in Ref. [38, 40, 41] that the total pair generation rate inside the microresonator is,

$$R_i \propto \gamma \epsilon_P^2 f_P / (\hbar \omega_P)^2 \times \frac{K^2}{(A+K)^4} \tag{2.55}$$

where γ is the nonlinear coefficient, ϵ_P is the total energy of the pump pulse, f_P is the pump repetition rate, ω_P is the A is loss rate (ω/Q_i) and K is the resonator bus waveguide coupling rate (ω/Q_c). Both photons are successfully extracted from the resonator with a probability $\left(\frac{K}{K+A}\right)^2$ so that the total extracted photon generation rate is,

$$R_{pair} \propto \gamma \epsilon_P^2 f_P / (\hbar \omega_P)^2 \times \frac{K^4}{(A+K)^6} \tag{2.56}$$

The total pair generation rate is maximized in the moderately overcoupled regime when ($K = 2A$). We note that even though the total pump power coupled into the microresonator is maximum at critical coupling, this only maximizes the single-photon heralding rate and not the total pair extraction rate. Additionally, if maximizing the purity of the output state is desired, then operating in the strongly overcoupled regime ($K \gg A$) is desired [42]. Strongly overcoupling the pump however must be accompanied by significant increase in the input pump power, which can be a nontrivial experimental constraint. Using interferometric coupling, it is possible to individually alter the coupling rates of the pump, signal and idler photons to heralding arm flux rate or the total heralding efficiency, depending on the target application [40].

Another important feature of integrated photon pair sources is the relative ease of engineering spectrally pure single-photon states by modifying spectral shape of the input pump to match that of the resonator. We recall from Equation (4.9) that the JSA of the generated pairs depends on the spectral shape of the pump and the phase-matching condition. As discussed previously, ensuring that the group velocity dispersion at the SFWM pump $\beta_P^{(2)}$ is small or moderately anomalous is sufficient to ensure broadband phase matching. Moreover, the bandwidth of the generated photon pairs is extremely

narrow such that the phase-matching conditions do not vary significantly over this bandwidth. The spectral purity is therefore predominantly determined by the shape of the pump pulse. Two pump photons within the pump envelope α_P combine to produce two photons ω_S, ω_P. Then Equation (2.39) can be modified to to an integral over four frequencies. We can write a modified equation for the JSA for the pump photons [43],

$$\begin{aligned} \phi(\omega_S, \omega_I) &= F_P(\omega_S + \omega_I) l_S(\omega_S) l_I(\omega_I) \\ F_P(\omega) &= \int \alpha(\omega)\alpha(\omega - \omega_P) l_P(\omega) l_P(\omega_P) \end{aligned} \tag{2.57}$$

Here, $l_k(\omega_k) = (-i\omega_k + \omega_k^0/(2Q_k))^{-1}$ is such that $|l_k(\omega_k)|^2$ is the Lorentzian lineshape of the resonator, ω_k^0 is the central resonant frequency and Q_k is the corresponding resonator quality factor. From Equation (2.57) it is clear that if the pump pulse is broadened to fill the entire resonator linewidth, the correlations between the generated photons will be significantly suppressed. However, the input pump pulse cannot be arbitrarily broadened beyond the corresponding resonator linewidth and this limits the spectral purity of the generated photons to 93% [43, 44]. This purity can be further improved by broadening the pump linewidth relative to that of the generated signal and idler photons. This can be achieved via interferometric coupling, where only the pump couples to the resonator on the through port and the signal and idler photons couple to the drop port. The coupling gap on the through port and the drop port can then be independently adjusted to get overcoupled pumps and critically coupled signal/idler photons. A version of this design was CADed during this thesis and is shown in Chapter 4 in our discussion of generating spectrally pure single photons for applications to frequency multiplexing.

2.3 Measurement and characterization of non-classical states of light

The characterization of both classical and quantum states of light primarily relies on correlation measurements and/or interferometric techniques. Young's double slit experiment, the Michelson interferometer and the Hanbury-Brown-Twiss (HBT) interferometer all probe the degree of coherence of the input light fields. The first two, Young's and Michelson's interferometer measure *field* correlations while the HBT interferometer measures *intensity* correlations. The HBT interferometer was first used to measure the angular separation of binary stars. The intensity correlations were insensitive to phase changes caused by atmospheric disturbances and therefore solved a crucial problem with previous measurements that relied on field correlations. The HBT measurement laid the foundation of higher-order coherence measurements that crucially exhibit signature non-classical statistics of different quantum states of light. While a first-order field correlation measurements can reveal the spectral properties such as bandwidth of the incident light, it cannot distinguish between states with identical spectra but different photon statistics.

2.3.1 Correlation functions in quantum optics

A full quantum theory of photo-detection and the corresponding motivation for the definitions of coherence functions is provided in Chapter of 4 of []. Here, we only state the main definitions and their qualitative interpretations. For an input light with a density

operator ρ, the field correlation function is defined as,

$$\begin{aligned} G^{(1)}(\boldsymbol{r_1}, \boldsymbol{r_2}; t_1, t_2) &= Tr[\rho E^{(-)}(\boldsymbol{r_1}, t_1) E^{(+)}(\boldsymbol{r_2}, t_2)] \\ &= \langle E^{(-)}(\boldsymbol{r_1}, t_1) E^{(+)}(\boldsymbol{r_2}, t_2) \rangle \end{aligned} \tag{2.58}$$

and the second-order correlation function is defined as,

$$G^{(2)}(\boldsymbol{r_1}, \boldsymbol{r_2}; t_1, t_2) = Tr[\rho E^{(-)}(\boldsymbol{r_1}, t_1) E^{(-)}(\boldsymbol{r_2}, t_2) E^{(+)}(\boldsymbol{r_2}, t_2) E^{(+)}(\boldsymbol{r_1}, t_1)] \tag{2.59}$$

Assuming a stationary process and plane waves ($\boldsymbol{r_1} = z_1, \boldsymbol{r_2} = z_2$), we can write the correlation functions in terms of the time delay, $\tau = t_2 - t_1 - \frac{z_2 - z_1}{v_g}$ where v_g is the group velocity. The normalized first and second-order coherence functions can then be written as,

$$\begin{aligned} \langle I(t) \rangle &= \langle E^{(-)}(t) E^{(+)}(t) \rangle \\ g^{(1)}(\tau) &= \frac{\langle E^{(-)}(t) E^{(+)}(t+\tau) \rangle}{\sqrt{\langle I(\tau) \rangle \langle I(t+\tau) \rangle}} \\ g^{(2)}(\tau) &= \frac{\langle E^{(-)}(t) E^{(-)}(t+\tau) E^{(+)}(t+\tau) E^{(+)}(t) \rangle}{\langle I(t) \rangle \langle I(t+\tau) \rangle} \end{aligned} \tag{2.60}$$

The definitions in Equation (2.60) have a certain time ordering and normal operator ordering, which correctly takes into account the quantum mechanical description of photo-detection. This ordering is crucial for analyzing photon statistics of non-classical states. For classical fields, it can be shown that $g^{(2)}(\tau) \leq g^{(2)}(0)$ and that $g^{(2)}(0) \geq 1$. Photons in classical states thus tend to *bunch* . This fact can be used to directly distinguish between classical and quantum states of light. For a single-mode quantum state, it can be readily shown that,

$$\begin{aligned} g^{(2)}(0) &= \frac{\langle \hat{a}^\dagger \hat{a}^\dagger \hat{a} \hat{a} \rangle}{\langle \hat{a}^\dagger \hat{a} \rangle^2} \\ &= \frac{\langle n^2 \rangle - \bar{n}}{\bar{n}^2} \end{aligned} \tag{2.61}$$

where $\bar{n}$ is the mean photon number. For a coherent state, Equation (2.61) evaluates to 1. For an $n-$ photon Fock state,

$$g^{(2)}_{Fock}(0) = 1 - \frac{1}{n} < 1 \tag{2.62}$$

The $g^{(2)}(0)$ of a Fock state is always less than 1 (representing *anti-bunching*), in clear deviation from that of classical states. The second-order coherence functions for thermal and coherent states are also independent of the average photon number in the input state. A measurement of $g^{(2)}(0)$ can be used to not only distinguish between quantum and non-classical states of light, but also between different quantum states. $g^{(2)}$ measurements were used in this thesis to quantify the noise properties of the multiplexed single-photon source in Chapter 3. We make a final comment about the $g^{(2)}$ functions from the output of parametric nonlinear processes (see Equation (2.43)). For single-mode parametric downconversion or four-wave mixing, the joint photon state is a two-mode squeezed state. If the $g^{(2)}$ of a single arm is measured, effectively tracing over the other arm, the results will correspond to that of a thermal state. However, an approximate single-photon state can be obtained by *heralding* on one of the arms. In the limit of low squeezing, higher-order contributions to Equation (2.43) are negligible and a heralded $g^{(2)}$ measurement on one of the arms will show non-classical statistics. We note that measurement of correlations and coherence functions can be used to characterize the degree of anti-bunching of quantum states. However, in order to probe other properties such squeezing, phase sensitive techniques such as homodyne and heterodyne measurements are required. These techniques are elucidiated in Ref. [45].

2.3.2 Heralding and post selection

Measurement of events in quantum mechanics is probabilistic. *Postselection* restricts the subspace of accepted events conditioned on the occurrence of a *heralding* event(s) while discarding all other events. Postselection is a powerful concept in computational complexity theory [46]. In a seminal paper, Knill, Laflamme and Milburn showed that given efficient single-photon sources and detectors as resources, linear operations with

beam-splitters, phase shifters and postselection via detection were sufficiently powerful to realize universal quantum computing. They proposed a nonlinear phase-shift gate that relies on two-photon interference, two ancilla photons and postselection that succeeds with 1/16 probability. The generation and detection of large entangled states known as cluster states for measurement-based quantum computing also rely on fusion gates, where the success of fusion is known via postselection. As discussed in the previous section, parametric nonlinear processes typically generate a two-mode squeezed state. However, detection of single-photon in one arm heralds the presence of a single-photon in the other arm in the low squeezing regime. Heralding events also provide feed-forward information which can be used to perform different operations in future time on the heralded photons. Our demonstration of a frequency multiplexed source relies on such feed-forward operations to switch photons to a common target frequency. In Chapter 4, we use a microresonator-based photon pair source that is not synchronized with the BS-FWM pumps. We work around this problem using postselection, and measure three-fold coincidences by heralding on the presence of the BS-FWM pumps.

2.3.3 Single-photon detectors and time tagging

Efficient single-photon detectors with low dark count noise and low temporal jitter are a key enabling technology for quantum photonics. Superconducting nanowire single-photon detectors (SNSPDs) have proved to be a revolutionary technology on this front [47, 48]. The state of the art SNSPDs have system detection efficiencies ranging from 93% to 97%, low timing jitter (< 100 ps), low dark count rate (< 1 Hz) and a reset time of 40 ns [48, 49] at 1.55 μm . These detectors enable efficient, low noise and fast characterization of non-classical states of light in free running mode. Previously, single-photon detectors in the infrared regime were based on InGaAs avalanche photodiodes,

which have <50% detection efficiency and suffered from relatively large dark count rates and low speeds unless operated in gated mode. While these detectors typically require sub-1K temperatures to operate, they are fiber coupled and up to 16-32 detectors can be accommodated in a single closed-cycle cryostat. The best performing SNSPDs still operate as "bucket detectors", i.e. they do not have photon number resolution (PNR) capabilities. For applications described in this thesis, PNR was not strictly required. However, certain applications in quantum photonics greatly benefit from PNR measurements. PNR measurements can be realized using "bucket" single-photon detectors together with spatial and temporal multiplexing schemes [50–54]. A more efficient technology is the use of transition edge sensors (TES) [55–57]. TES detectors with up to to 98% efficiency, negligible dark counts and PNR resolution up to 17 photons have been demonstrated. These detectors are however operated at significantly lower temperatures than SNSPDs and therefore have significantly more recovery time in the range of 5-10 μs. This limits the speed of possible operations significantly. Several groups are currently working on modifying the design of SNSPDs to provide moderate photon number resolution up to 5 photons [58]. We will describe in Chapter 3 how the use of fast PNR operations can significantly improve the performance of multiplexed single-photon sources. The electronic pulses from single-photon detectors (TTL/RF pulses) can be electronically recorded using commercial time tagging modules. These multi-channeled modules are field programmable gate arrays that assign a "time tag" on an absolute periodic time scale (10 us) to all events (pulses above the threshold voltage). These recorded time tags can then be used to reconstruct histograms of photon counts and/or for post-selection based on electronic trigger signals synchronized to heralding events (such as modulated BS-FWM pumps). All measurements in this thesis used a Roithner Laserteknik TTM800 time tagging module with 82 ps free-running resolution. Better channel resolution can be obtained via different acquisition modes. TTM modules

with better timing resolution down to 10 ps are are now commercially available.

CHAPTER 3

FREQUENCY MULTIPLEXING FOR HERALDED SINGLE-PHOTON SOURCES

Parametric single-photon sources are probabilistic due to multi-photon generation which is intrinsic to the spontaneous nonlinear processes discussed in the previous chapter. A promising way to overcome this intrinsic limitation is to *multiplex* the output of several probabilistic sources using an active switching network [59–63]. A key requirement for realizing an efficient multiplexed source is a low loss $N\times1$ switch that can accommodate a large number of modes [64]. Several multiplexed single-photon sources using spatial and temporal degrees of freedom of a photon were demonstrated prior to this work [65–71]. By operating individual sources in a regime with low pair production probability, such schemes allow for increasing the single-photon probability without additional multi-photon generation. A key requirement for efficient multiplexing is a low-loss $N \times 1$ switching network that accommodates a sufficiently large number of modes N to achieve deterministic operation. Deterministic operation can be achieved with as few as $N = 17$ multiplexed modes with a lossless switching network and photon-number resolving (PNR) detectors [72]. Recently, there have been a number of promising demonstrations of multiplexed sources using the spatial and temporal degrees of freedom of a photon [65–71]. However, for both spatial and temporal multiplexing, switching losses increase with the number of modes N, which deteriorates enhancement achieved from multiplexing beyond a few modes. Deterministic operation is therefore challenging to achieve without the use of bulky free-space setups [73, 74].

In this work, we developed and demonstrated an alternative scheme using frequency multiplexing where losses do not scale with the number of modes. Frequency multiplexing allows for multiple switching operations in a single spatial mode, thus effectively

implementing an $N \times 1$ switch in a monolithic optical structure such as a single mode fiber or waveguide. Therefore, distinct from other schemes, switching losses remain fixed irrespective of the number of multiplexed modes N. Quantum frequency translation via BS-FWM, which we perform with close to unity intrinsic efficiency and ultra-low noise, can act as a "frequency switch". This allows us to perform active "frequency switching" of multiple frequency channels to a common target channel [75]. We present a complete characterization of our frequency multiplexing scheme, including theoretical analysis of the scaling performance for large N. We present a proof-of-principle demonstration of frequency multiplexing using three frequency modes in an entirely fiber-based setup that leverages on low-loss off the shelf dense wavelength division multiplexing (DWDM) components. With this low-loss and low-noise setup we achieve generation rates of 46 kHz multiplexed photons with coincidences-to-accidentals ratio exceeding 100 and $g^{(2)}(0)$ of 0.07. BS-FWM is efficiently tunable over a large bandwidth of more than 1 THz and therefore our system can be scaled to include a large number of frequency modes, which is required for deterministic photon generation using multiplexing.

We note that recently, multiple research groups have proposed the use of frequency multiplexing as a resource for both continuous variable [76, 77] and circuit-based single-photon QIP applications [78, 79]. These proposals emphasize the strong potential of frequency multiplexing for addressing the scaling losses and resource overheads in quantum systems. However, most proposals rely on electro-optic modulators (EOMs) to frequency translate single photons. Recent work [80] discusses a spectrally multiplexed single-photon source using EOMs, but no enhancement in the single-photon rate is demonstrated due to high system losses. Another recent demonstration is more promising and also has indistinguishability measurements. EOMs typically have a limited time-bandwidth product close to unity, limiting the maximum frequency shift and the bandwidth of the target pulses. Typical fiber-coupled EOMs also have high insertion loss

of around 3-5 dB. This significantly limits practical implementations to a few frequency modes while exacerbating photon loss due to narrow filtering. Alternatively, our implementation of BS-FWM allows for tunable conversion over 1 THz with an acceptance bandwidth of 100 GHz with few nanosecond pump pulses, which addresses these issues.

3.1 Concept of frequency multiplexing

Figure 3.1 illustrates our frequency multiplexing scheme. A single source that generates broadband frequency correlated photon pairs is used to create narrowband frequency channels $\{\omega_0, \omega_1 ...\}$. One photon from the pair (heralding photon, not shown) is used to herald the presence of the signal photon. Due to energy conservation, the two photons are correlated in frequency, with the heralding photon providing information about the frequency of the signal photon. This heralding information is used to translate the frequency of the signal photon to the target frequency channel ω_t using tunable frequency conversion. We thus effectively implement an active frequency switch to route photons from multiple frequency bins to a single output frequency channel. In order to be viable as an $N \times 1$ switch for large N, the tunable frequency conversion must be efficient over a sufficiently large bandwidth, which is possible with BS-FWM (Figure 2.6). BS-FWM allows for independent control of the input and target frequencies by selectively activating auxiliary pumps in the interaction (see Figure 3.1b). Since phase matching can be achieved by symmetric placement of the classical pumps and quantum fields about the zero-dispersion wavelength of the nonlinear medium, the same setup can be reconfigured to target different frequency shifts by tuning the pump wavelength. For efficient conversion, it is critical that the bandwidth of individual channels be less than the acceptance bandwidth $\Delta\nu_{BS}$ of the BS-FWM process for two fixed pumps. This all-optical frequency switch can support ultrafast operation, with the repetition rate limited only to

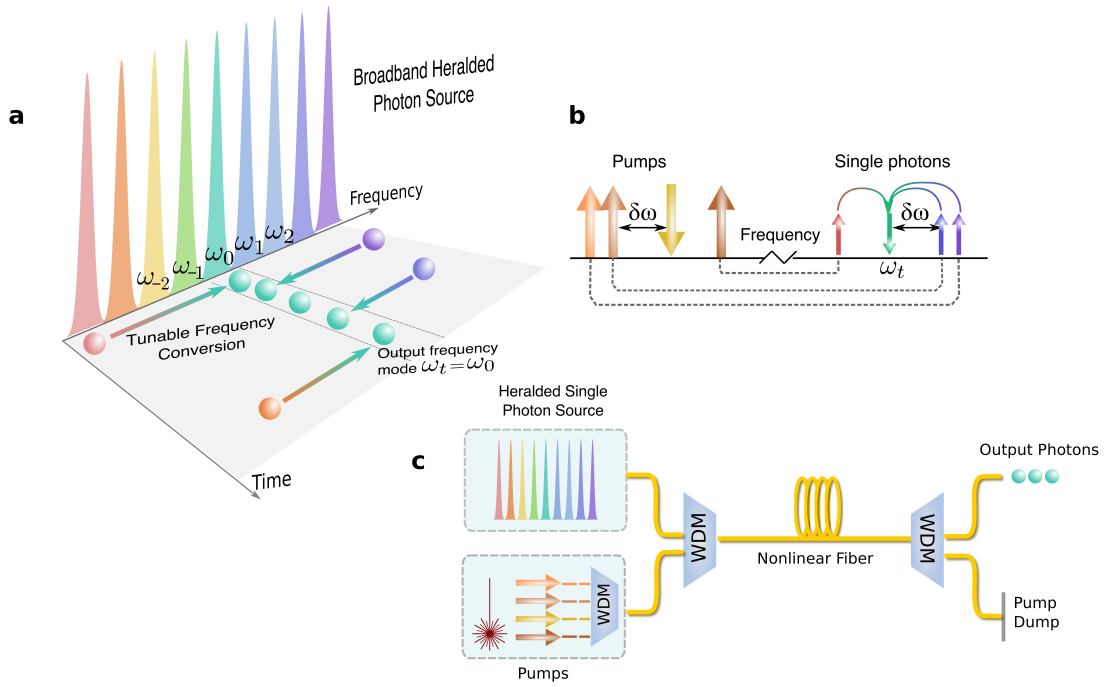

Figure 3.1: **Principle of a frequency multiplexed single-photon source. a)** Multiple narrowband frequency channels $\{\omega_0, \omega_1 ...\}$ are extracted from a broadband single-photon source. Tunable frequency conversion is used to convert photons from different channels to a common target frequency mode ω_t. **b)** Tunable frequency conversion using Bragg scattering four-wave mixing (BS-FWM): Two strong classical pumps drive the interaction between the input and target (ω_t) single-photon fields. The frequency separation $\delta\omega$ between the pump fields determines the frequency shift of the single photons, and additional pump fields can be used to increase the number of possible values of $\delta\omega$. **c)** Fixed-loss operation of frequency multiplexing: single photons and BS-FWM pumps are combined using wavelength division multiplexers (WDM), and all active frequency switching takes place in a single nonlinear fiber/waveguide. Additional channels can be added by introducing additional pumps, without introducing losses in the path of the single photons.

the inverse bandwidth $1/\Delta\nu_{BS}$. Finally, we note that all frequency switching takes place in a single spatial mode (nonlinear fiber/waveguide), as shown in Figure 3.1c. As additional channels only require additional BS-FWM pumps, no scaling losses are introduced in the path of the single photons.

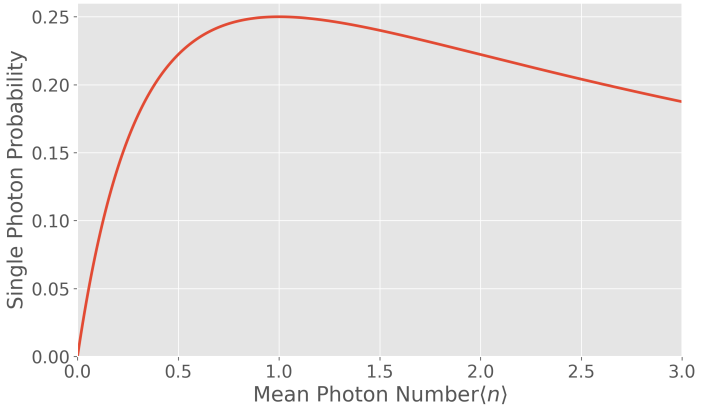

Figure 3.2: Single-photon heralding probability for a single SPDC source. The maximum probability of heralding a single photon is 25%, which occurs for squeezing levels such that the mean photon number $\mu = 1$.

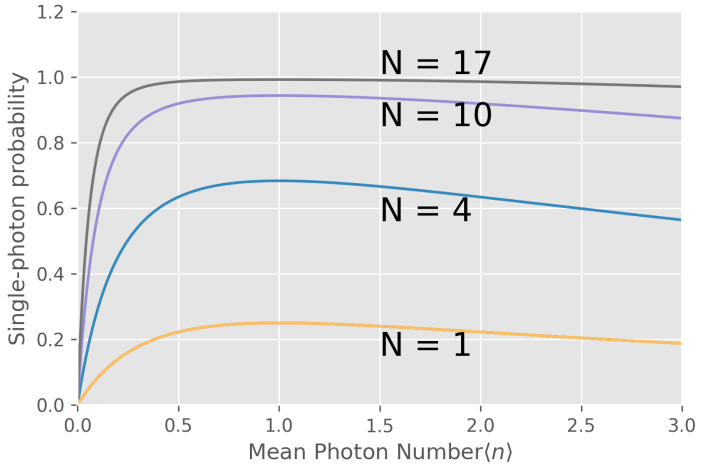

Figure 3.3: **Single-photon heralding probability for an ideal multiplexed source** Assuming PNR detectors with unity efficiency and a lossless switching network, a deterministic single-photon source can be obtained with just 17 sources.

3.2 Theoretical predictions

3.2.1 Limits to single-photon generation from a single parametric source

We adapt the analysis presented in References [72, 81]. In order to simplify the analysis, we assume that the SPDC produces photons in a single spatio-temporal mode and generates photons in a two-mode squeezed state as in Equation (2.43),

$$|\psi\rangle_{\mathrm{PDC}} = \sqrt{1-|\xi|^2}\sum_{n=0}^{n=\infty}\xi^n|n_s, n_i\rangle \tag{3.1}$$

where ξ is the squeezing parameter. As discussed previously, the photon statistics of a single-arm, obtained by tracking over the distribution of the other arm resembles a thermal distribution, causing probabilistic operation. The mean photon number for this distribution can be calculated from Equation (3.1),

$$\mu = \frac{|\xi|^2}{1-|\xi|^2}. \tag{3.2}$$

Figure 3.2 shows the maximum single-photon heralding probability as a function of the mean photon number (which is related to the squeezing parameter via Equation (3.2)). The maximum probability is 25% with $\mu = 1$. Multiplexing overcomes this limitation by operating at a significantly lower mean photon number μ for each source, thus reducing the probability of multi-photon emission while increasing the probability that at least one photon is heralded from one of the sources.

3.2.2 Multiplexed sources

The performance of multiplexed sources depends crucially on two factors (i) The loss performance of the switching network (ii) the nature of single-photon detectors. We will therefore analyze the performance of these separately.

The crucial difference between using "threshold" (non photon number resolving) and PNR (photon number resolving) detectors comes from the fact that a multiplexed source operated with PNR detectors can be operated at a higher mean photon number and the multi-photon events can be rejected, increasing the overall single-photon probability. The positive operator valued measurement (POVM) for threshold detectors is [28],

$$\Pi_{\text{th}} = \sum_{n=0}^{\infty} [1 - (1 - \eta_d)^n] |n\rangle\langle n| \tag{3.3}$$

Here η_d is the detector efficiency. The above expression sums over all possibilities where the detector registers at least one "click". The total heralding probability is obtained by summing over the probability of an n-photon Fock state registering a 'click' on the detector, given by $[1 - (1 - \eta_h)^n]$, over all n.

$$p_h^{\text{th}} = \langle\psi|\Pi_{\text{th}}|\psi\rangle \tag{3.4}$$

$$p_h^{\text{th}} = \frac{\eta_h |\xi|^2}{1 - (1 - \eta_h)|\xi|^2} \tag{3.5}$$

where η_h is the net efficiency on the heralding arm.

The POVM for a PNR detector is [28],

$$\Pi_{\text{pnr}}(n) = \sum_{N=n}^{\infty} \binom{N}{n} (1 - \eta_d)^{N-n} \eta^n |N\rangle\langle N| \tag{3.6}$$

The probability of detecting a single-photon on the heralding arm can then be calculated

to be,

$$p_h^{\text{pnr}} = \langle\psi|\Pi_{\text{pnr}}(n=1)|\psi\rangle \tag{3.7}$$

$$p_h^{\text{pnr}} = \frac{\eta_h|\xi|^2(1-|\xi|^2)}{(1-(1-\eta_h)|\xi|^2)^2} \tag{3.8}$$

The conditional probability that the heralded state in the signal arm is a single photon can be calculated by tracing over the heralded state $\langle\rho_s\rangle$, and is the same for both cases. We exclude contributions erroneous events where multi-photon events are detected as single photons in the signal arm.

$$p_s = \frac{1}{p_h}\eta_d\eta_h|\xi|^2(1-|\xi|^2) \tag{3.9}$$

where η_d is the net efficiency on the signal (heralded) arm and p_h is given by Equation (3.5) or Equation (3.8) depending on the detector. For N multiplexed sources, the probability that a heralding photon is registered in at least one of the N sources is given as,

$$p_h^{mux}(N) = 1-(1-p_h)^N \tag{3.10}$$

For small heralding probability p_h, the probability that at least one multiplexed source triggers is Np_h. As N increases, optimal performance is achieved for lower mean photon number μ, as shown in Fig. 3.3. Therefore, to obtain the scaling performance of the schemes we optimize μ for each N, maintaining this μ across schemes. If the net efficiency of the switching network is η_{switch}, the corresponding total probability that a single photon is heralded at the output is given by combining Equations (3.9) and (3.10),

$$p_s^{mux}(N) = \eta_{switch} \times p_s \times p_h^{mux}(N) \tag{3.11}$$

Several architectures have been explored for active $N \times 1$ switching of photons in spatial and temporal multiplexing schemes. Typically, these architectures use 2×2 switches as building blocks for a general $N \times 1$ switch. We compare the performance of the fixed loss scheme with the log-tree network which is generally used for spatial

multiplexing and multi-pass binary switches (or storage cavities) generally used in temporal multiplexing [69,70]. An $N\times1$ log-tree network has a depth $\lceil \log_2 N \rceil$. Assuming a switching efficiency of η_s per switch, the losses scale as $\eta_s^{\lceil \log_2 N \rceil}$ [81]. For our fixed-loss scheme, the switching losses are η_s irrespective of N.

$$\eta_{switch}^{fixed-loss} = \eta_s \tag{3.12}$$

$$\eta_{switch}^{log-tree} = \eta_s^{\lceil \log_2 N \rceil} \tag{3.13}$$

where η_s is the switching efficiency per switch. The losses from multi-pass binary switching scale exponentially as η_s^N in the worst case, but we consider an optimized implementation as in Ref. [70]. We compare the results with implementations of time multiplexing, that uses an optimized version of the multi-pass scheme to get better performance [70]. Losses are minimized by routing photons from the the last heralded slot in case of temporal multiplexing. The total heralding probability in this case is given by,

$$p_s^{mux} = \sum_{j=1}^{N} (1-p_h)^{N-j} p_h \times p_s \eta_s^{N-j} \tag{3.14}$$

In Equation (3.14), the first term is the probability that no photon was heralded in the last $N-j$ slots,and the corresponding switching losses are equal to η_s^{N-j}. We again exclude the cases where multi-photon emission is detected as a single photon event due to switching losses.

Finally, the conditional multi-photon probability for a given squeezing parameter is (ignoring switching losses):

$$\begin{aligned} p_{multi} &= |\xi|^4 \\ &= \left(\frac{\mu}{1+\mu}\right)^2 \end{aligned} \tag{3.15}$$

As the mean photon number is reduced for increasing N, the multi-photon noise correspondingly reduces for large N.

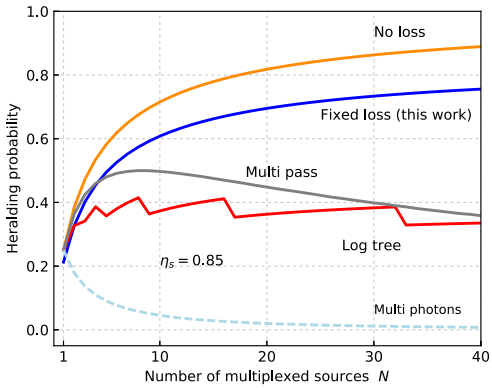

(a)

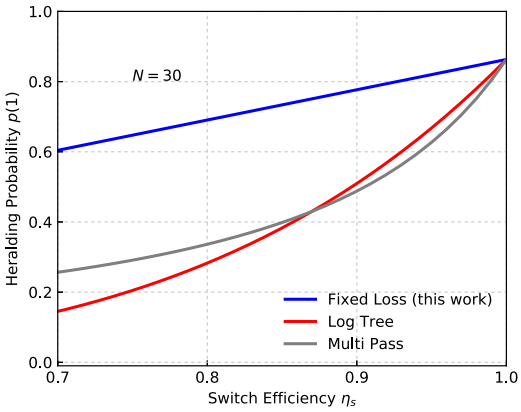

(b)

Figure 3.4: **Theoretical prediction of scaling performance for various switching schemes with threshold detectors**. **a)** The maximum single-photon heralding probability for a single source ($N = 1$) is 0.25. For an efficiency of $\eta_s = 0.85$ (0.7 dB loss) per switch, the single-photon emission probability for both log-tree and multi-pass schemes reaches a maximum of $0.41, 0.50$, respectively, and then saturates for large N due to scaling losses. In contrast, additional multiplexed sources always result in improved performance for the fixed-loss scheme, with $p_{mux}(n = 1) = 0.75$ for $N = 40$ sources. The multi-photon emission probability $p_{mux}(n > 1)$, ignoring switching losses, is shown as the dashed light blue curve, and is less than 1% for $N = 40$ modes. **b)** Single-photon heralding probability for various switching schemes as a function of switch loss, for a fixed number of sources $N = 30$. The fixed-loss scheme is significantly more robust to variability in switching losses. Note that the maximum heralding probability for $\eta_s = 1$ is not equal to 1 since the heralding detectors are non-photon-number resolving.

Loss performance of various switching schemes

To understand clearly the characteristics of our frequency multiplexing scheme, we analyze how the performance scales for varying number of multiplexed sources N and

switching efficiency η_s, for both threshold and PNR detectors.

Threshold detectors

Figure 3.4a shows a comparative scaling of the various schemes with threshold detectors. We assume a switching efficiency $\eta_s = 0.85$ (0.7 dB loss) per switch and all other components, including detectors, are assumed to be ideal ($\eta_d = \eta_s = 1$). We optimize the emission probability per source $p_{single}(n = 1)$ for each N. The maximum heralding probability for a single source ($N = 1$) is 0.25. For both log-tree and multi-pass schemes, the single photon probability reaches a maximum of 0.41 and 0.50, respectively, and saturates due to switching losses for less than $N = 10$ multiplexed sources. In contrast, for the fixed-loss scheme, additional multiplexed sources always result in an improvement in the single-photon heralding probability, with a heralding probability of 0.60 for N= 10 sources. For N= 40 sources, the fixed-loss scheme achieves $p_{mux}(n = 1) = 0.75$, compared with a maximum of 0.89 with a no-loss ideal switching network. Our scheme therefore has an advantage in the intermediate regime of 10 to 20 multiplexed modes as well as asymptotically for large N. In order to quantify the effects of practical variability in switching efficiency in implementations of multiplexed sources, we analyze the sensitivity of different schemes to switching losses in Figure 3.4b. For a moderate increase in losses to 1.2 dB per switch and 30 multiplexed modes ($\eta_s = 0.75, N = 30$), the single photon probability drops significantly from 0.86 ($\eta_s = 1$) to $0.21, 0.29$ for the log-tree and multi-pass schemes, but is reduced only moderately to 0.65 for the fixed-loss scheme. Thus, the frequency multiplexing scheme is significantly more robust to switching losses as compared to competing switching architectures in other multiplexed sources.

Photon number resolving (PNR) detectors

The predictions in Figure 3.4 for threshold detectors show that the maximum heralding probability saturates at around 75% for the fixed loss scheme, even with ideal detectors. With PNR detectors, significantly better performance can be achieved, as the mean photon number μ for each source can be kept high and multi-photon events can be rejected by the PNR heralding. This results in significantly better performance, as shown in Figure 3.5.

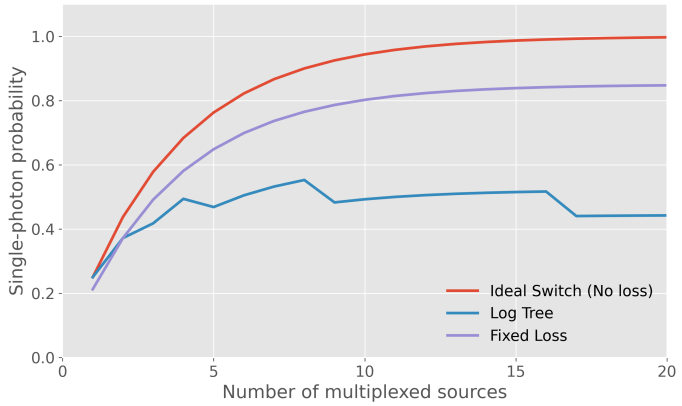

Figure 3.5: **Scaling losses with PNR detectors:** Comparative scaling losses when PNR detectors are used for heralding. The fixed loss scheme results in 85% heralding probability with 17 sources, while the log-tree scheme saturates at 55% for 8 sources. We have assumed a single-switch efficiency of 85% and detectors with unity efficiency for this analysis.

3.3 Experimental setup

We experimentally demonstrate multiplexing of three frequency modes. Figure 3.6 shows our experimental setup. Our multiplexed source is based on broadband SPDC in a periodically-poled lithium-niobate crystal (PPLN) pumped with a 543-nm CW-laser, generating photon pairs at 940 nm (heralding photons) and 1280 nm (heralded signal photons). The heralding photons are sent to a filtering setup consisting of reflecting

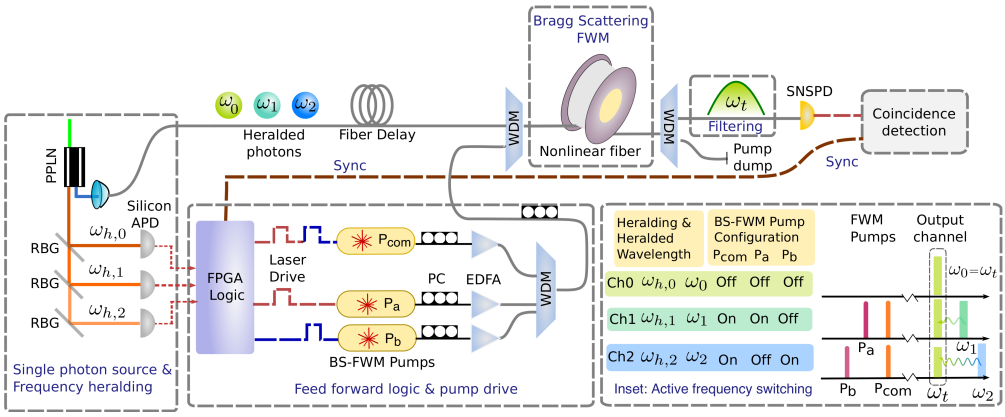

Figure 3.6: **Experimental setup for multiplexing of three frequency modes**. PPLN - periodically poled lithium niobate, RBG - reflecting Bragg grating , FPGA - Field programmable gate array, PC: polarization control, EDFA: erbium-doped fiber amplifier, WDM- wavelength division multiplexer, BS-FWM - Bragg scattering four-wave mixing, SNSPD: superconducting nanowire single-photon detectors. A PPLN crystal is pumped with a CW laser at 543 nm, generating photon pairs at 940 nm (heralding photons) and 1280 nm (heralded photons). The heralding photons are filtered into three channels $\{\omega_{h,0},\omega_{h,1}, \omega_{h,2}\}$ with 100 GHz bandwidth, with corresponding heralded signal photons as $\{\omega_0, \omega_1, \omega_2\}$. An FPGA is used to process this heralding information and selectively activate the BS-FWM pumps (see inset), such that the heralded photons are switched to the target frequency ω_t. The signal photons are combined with the BS-FWM pumps using WDMs, and sent to the nonlinear fiber. A free-space filtering setup extracts photons at ω_t at the output, which are then sent to an SNSPD. A time-tagging module is used for coincidence measurements between the FPGA processed heralding trigger (sync) and the output of the SNSPD.

Bragg gratings (RBG), creating three channels CH0, CH1, CH2 with heralding photons at $\omega_{h,0}$, $\omega_{h,1}$, $\omega_{h,2}$, respectively, with 100-GHz bandwidth. Each channel is collected into a single-mode fiber and sent to a silicon avalanche single-photon detector, which provides heralding information to the logic circuit. The source crystal temperature is tuned to maximize photon pair production at $\omega_1 = 1280.65$ nm and $\omega_2 = 1280.1$ nm, and the pair production at $\omega_0 = 1284.45$ nm is lower by a factor of 0.65. The heralded signal photons $\{\omega_0 = 1284.45 \text{ nm}, \omega_1 = 1280.65 \text{ nm}, \omega_2 = 1280.1 \text{ nm}\}$ are injected into the multiplexing setup, comprised of a 100-m nonlinear fiber, wavelength-division-multiplexing couplers and a pump filter (total losses 2.2 dB). A single channel centered at $\omega_t = 1284.45$ nm and 100 GHz wide, is selected with a tunable grating and then sent to a superconducting

nanowire single-photon detector (SNSPD) with a quantum efficiency of 53%.

The nonlinear process of BS-FWM is driven by two pump waves generated by distributed feedback lasers diodes, which determine the frequency shift and hence the input and output frequency channels. The diodes are driven with a 5-ns-long pulsed current source, and the optical pulses (for convenience aligned to the C-band ITU grid) are amplified to a peak level of 10 W via cascaded erbium-doped fiber amplifiers (EDFA). The pump pulses are combined together, temporally synchronized and aligned in polarization. In order to achieve fast switching operations, we utilize lasers at predetermined wavelengths that are selectively turned on and off via a fast logic circuit controlled by a field programmable gate array (FPGA) (see inset in Figure 3.6). We measure the conversion efficiency for both process $\omega_1 \rightarrow \omega_t$ and $\omega_2 \rightarrow \omega_t$ to be 93%. The intrinsic conversion efficiency in this case was limited to 93% due to fluctuations in BS-FWM pump power due to randomized trigger. This can be improved to 97% with pulsed pumps (Figure 2.6)

3.4 Results: Photon generation rate, coincidences-to-accidentals ratio, single-photon purity

Heralded single-photon rate

We first characterize the heralded single-photon rates as functions of SPDC pump power for each individual channel and for the multiplexed source, as shown in Figure 3.7a. The multiplexed (MUX) source has an enhanced coincidence rate by 4.8 dB as compared to the mean photon rate of the individual channels. This enhancement significantly

overcomes the losses of the setup (1.3 dB), resulting in a net enhancement of 3.5 dB (220%) in the heralded single-photon rate. At maximum SPDC pump power (25 mW), we measure a heralding rate of 1 MHz with a brightness of 23 kHz detected coincidences per second. We estimate a single-photon generation rate of 46 kHz after correcting for detector efficiency (3 dB), which is the highest reported rate for multiplexed photon sources to date. We note that although simply increasing the pump power of the SPDC source can increase the single-photon generation rate of a single source, this would lead to increased multi-photon generation.

Coincidences-to-accidentals ratio (CAR)

We measure the coincidences to accidentals ratio (CAR), a standard figure of merit to characterize the multi-photon generation of parametric sources. Figure 3.7b compares the CAR for the multiplexed source and each individual channel. For fair comparison we also measure the coincidence rate and CAR at ω_t, directly from the SPDC source, without the multiplexing setup in place (referred to as the NoMUX source). We operate in a regime in which the single-photon count rate is much higher than the dark-count rate of the detectors, and therefore the accidental counts are dominated by multi-photon generation, which is inversely proportional to the SPDC pump power. The multiplexed source has a CAR that is a factor of 2 higher throughout as compared to the NoMUX source. For low count rates, the multiplexed source has a CAR exceeding 1000 and remains high at 100 at the maximum count rate. These measurements confirm that the strong classical pumps used in BS-FWM do not introduce significant spurious noise photons even at a high pump trigger rate of 1 MHz.

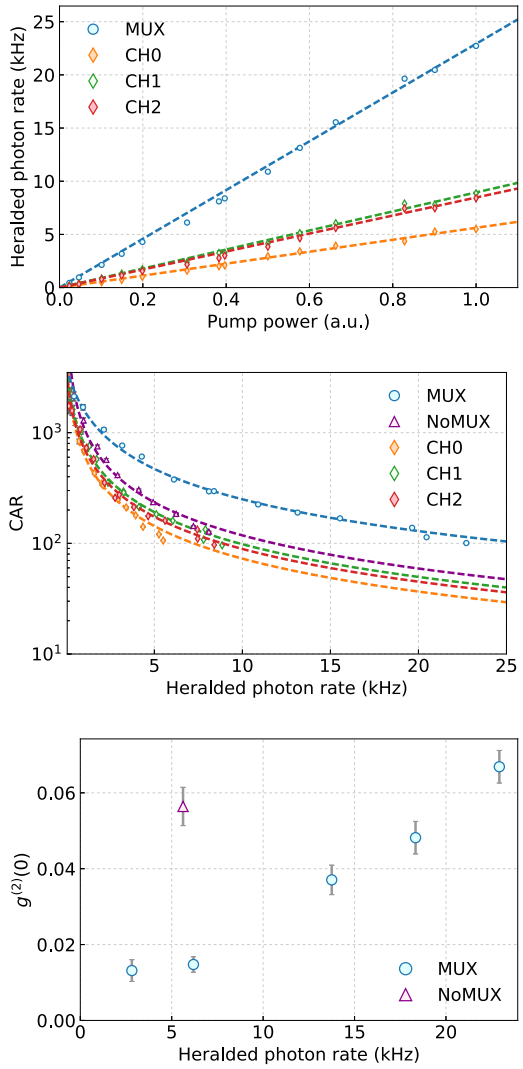

Figure 3.7: **Experimental results from multiplexing of three frequency modes.** Blue circles: multiplexed (MUX) source, purple triangles: NoMUX source, diamonds: contributions from the individual channels (orange - CH0, green - CH1, red - CH2). **a)** Total coincidence counts (heralded photons) as a function of SPDC pump power: The multiplexed source has an enhanced coincidence rate by 4.8 dB as compared to the mean of the individual channels and overcomes the losses of the setup (1.3 dB), with a net enhancement of 220%. At maximum SPDC pump power (25 mW), we measure a heralded photon rate of 23 kHz from the multiplexed source. **b)** Coincidences to accidentals ratio (CAR) vs coincidences: For a fixed coincidence rate, the multiplexed source has a CAR that is a factor of 2 higher as compared to the NoMUX source. For low coincidence rates, the multiplexed source has a CAR exceeding 1000 and remains high at 100 for large coincidence rates. **c)** Measurement of $g^{(2)}(0)$: The multiplexed source has a low $g^{(2)}(0)$ of 0.07 ± 0.005 for large coincidence rates. For the same coincidence rate of 2.5 kHz the multiplexed source has an improved single-photon purity with $g^{(2)}(0)$ of 0.015 ± 0.002 as compared to the NoMUX source with a $g^{(2)}(0)$ of 0.056 ± 0.005. Error bars are estimated using Poisson statistics.

Single-photon purity ($g^{(2)}(0)$)

Finally, we measure the purity of the photons from the multiplexed source by performing a heralded second-order correlation measurement using the Hanbury-Brown-Twiss (HBT) setup [82]. We measure $g^{(2)} = N_{abh}N_h/N_{ah}N_{bh}$ where N_{abh} is the three-fold coincidence rate between the three arms of the HBT setup, N_h is the single-photon heralding rate and N_{ah} and N_{bh} are the normalizing two-fold coincidence rates. Figure 3.7c shows the measured $g^{(2)}(0)$ for the multiplexed source and the NoMUX source, for various heralded photon rates. At the maximum heralded photon rate, the multiplexed source has a low $g^{(2)}(0)$ of 0.07 ± 0.005. For the same low heralded photon rate of 2.5 kHz, the multiplexed source and the NoMUX source have $g^{(2)}(0)$ of 0.015 ± 0.002 and 0.056 ± 0.005 respectively. The average SPDC pump power required to achieve the same photon rate is a factor of 3 lower for the multiplexed source as compared to the NoMUX source, and therefore has significantly reduced multi-photon generation. The improved single photon purity of the multiplexed source is therefore a strong indicator of successful multiplexing.

Pulsed operation and scaling

At the time of publication of this work, the performance of our frequency multiplexed source was comparable with the best multiplexed source demonstrated to-date which implemented temporal multiplexing on a free-space optics platform [70]. Prior to this work, the best demonstrated single-photon rate was 19.3 kHz with a $g^{(2)}(0)$ of 0.48 [70]. Better absolute single-photon efficiencies up to 67% have since been demonstrated [74]. Due to the low loss of our frequency switch (1.3 dB), we achieve a multiplexing enhancement factor of 2.2 with just three frequency modes. We measure a raw heralding efficiency of 2.3% and detector-corrected efficiency of 4.6%, which is the highest amongst

fiber-based and integrated multiplexed systems demonstrated so far. This efficiency is mainly limited by the fiber-collection and spectral filtering loss at the SPDC source and is independent of our "frequency switching" setup. Collection efficiencies as high as 90% can be achieved by minimizing all transmission and filtering losses, and careful mode-matching, which would correspond to an order of magnitude improvement in the heralded single-photon rates [24, 83].

Another important figure of merit for comparing the different multiplexing implementations is the maximum possible switching speed. In principle, our all-optical frequency switch allows for efficient conversion with repetition rates as high as the inverse of the BS-FWM acceptance bandwidth (100 GHz in this system). Our current implementation can support a repetition rate of 5 MHz and is limited by the amplification required for the BS-FWM pumps. This amplification requirement can be reduced by increasing the BS-FWM interaction length or or by using shorter pump pulses just enough to match the photon duration.

In order to obtain photons in well-defined temporal modes, pulsed operation is necessary. The efficiency of our "frequency switch" is partially limited to 93% due to the fluctuations in BS-FWM pump power induced by the randomized trigger arising from CW operation of the single-photon source. We measure efficiencies as high as 97% using the same setup with periodic pump triggering.

In Figure 3.8a we show that we can add up to 10 additional channels separated by 100 GHz without significant reduction in the conversion efficiency. For this measurement, we fixed a target frequency ω_t, and we fix one pump while detuning the other such that the frequency separation between the pumps equals the frequency separation between the input and target. The maximum conversion efficiency is maintained for all 10 channels. The acceptance bandwidth however reduces by a factor of 2, from 160 GHz for the first

channel to 70 GHz for the 10th channel due to effects of higher-order dispersion.

Figure 3.8b shows the calculated scaling performance of the frequency multiplexed source for 10 modes. We assume a feasible value for detector and fiber-collection efficiency of 90%. Heralding efficiencies as high as 50% can be achieved using just 10 multiplexed modes.

With just 10 multiplexed modes, our system is capable of achieving a single-photon heralding probability exceeding 50% (per input pump pulse) with a single-photon generation rate of 2.5 MHz. Finally, we note that using cavity-based sources with the spectral line-width of the pump pulse matched to the cavity line-width, it is possible to generate discrete uncorrelated joint spectral amplitudes [84]. Our system is therefore capable of approaching the regime of deterministic photon generation in pure spectral and temporal modes.

3.5 Implementation on integrated platforms and generation of spectrally pure photons

In order to generate indistinguishable photons using frequency multiplexing, the correlations between the heralding and the heralded photon must vanish within the filtering bandwidth of each channel (set less than or equal the BS-FWM bandwidth). Currently, we use a 1 cm PPLN crystal with Type 0 phase matching. Due to the highly non-degenerate nature of our downconversion source, the resulting phase matching condition is tight (Figure 3.9). This results in highly correlated photon pairs within the filtering bandwidth (see Figure 3.9b). The resulting photon purity is low with a calculated Schmidt number of 5.38. Using a shorter PPLN crystal to reduce the interaction length relaxes this condition

sufficiently to allow the generation of spectrally pure photons after filtering. Using a short 1 mm PPLN crystal and Type 0 phase matching results in a joint spectral intensity (JSI) after filtering (bandwidth - 100 GHz) with a Schmidt number K = 1.12. The expected indistinguishability is 1/K= 0.89. A shorter PPLN crystal however would reduce the photon generation rate by an order of magnitude.

A more efficient way to generate spectrally pure photon pairs in well-defined frequency modes is to use an integrated, micro-resonator-based source. We refer to Section 2.2.4 for a detailed discussion on SFWM in microresonators. As discussed in Section 2.2.4, the brightness and spectral purity of integrated sources can be controlled by modifying the coupling conditions for the pump, signal and idler photons. In particular, spectrally pure states can be generated by using an interferometric coupling scheme where the SFWM pump is overcoupled and the signal and idler photons are critically coupled. During the course of this thesis, a design to generate spectrally pure photons using such a scheme was fabcricated. The design is for a 200 GHz FSR ring resonator with 1350 nm waveguide width (moderately anomalous dispersion @1300 nm). The interferometric coupler is designed to suppress every other resonance on the drop and through port. Crucially, the gap on the through port for coupling the pump in smaller than that on the drop port. Using the integrated heaters, the phase of each of the coupler can be tuned get maxima/minima of transmission at the desired resonant frequencies. We note that even if this phase tuning is not precise, this at best results in coupling conditions that are slightly off from the optimal locations, and some leakage of the pump photons in the drop port and of the generated photons on the through port. This design is therefore robust. This chip can be used in future experiments for generating spectrally pure single photons and for a demonstration of indistinguishability with this design.

We have demonstrated a novel frequency multiplexed source with three modes, using

highly-efficient low-noise quantum frequency translation. We emphasize that adding additional channels adds complexity only to the BS-FWM pump configuration and no new components need to be added in the path of the single photons. This ensures that losses remain independent of the number of multiplexed modes. The single spatial mode operation of frequency switching maintains relative polarization stability of photons from different channels from generation to detection, ensuring that the photons are rendered indistinguishable after frequency translation. BS-FWM is fully compatible with the existing optical telecommunication architecture that harnesses dense wavelength division multiplexing (DWDM). The applications of such low-loss high repetition rate frequency multiplexing go beyond single-photon sources and can prove to be highly advantageous for all-photonic quantum repeaters that rely on active feed-forward heralding signals [85]. Our scheme is also entirely adaptable to CMOS-compatible integrated platforms. In particular, integrated comb sources where photons are already confined in well-defined frequency bins can eliminate the need for filtering [86–88] while generating spectrally pure photons [84]. In addition, implementations of BS-FWM in nanophotonic waveguides can significantly reduce pump power and amplification requirements [89]. Frequency multiplexing can thus uniquely harness both fiber and integrated technologies optimized for classical applications to address challenges of scalability in quantum technologies.

3.6 Additional system characterization

Source characterization

We characterize the spectrum of our idler (heralding) photons using a single photon spectrometer (Ocean Optics). The results are shown in Fig. 3.11. The heralding photons

are filtered into 100 GHz wide channels using reflecting Bragg gratings. The highlighted regions reflect the corresponding heralded channels.

Characterization of system efficiency

We measure the heralding efficiency on the multiplexed photon arm by measuring the ratio of the detected coincidences to the heralding rate, as shown in Fig. 3.12. The raw heralding efficiency is about 2.3%. Without the multiplexing setup in place, we measure a heralding efficiency of 3%, corresponding to a 1.3 dB loss due to the multiplexing BS-FWM setup. The losses in the path of the multiplexed photon after collection from the SPDC source were measured to be: 1.3 dB BS-FWM setup (WDMs and nonlinear fiber), 1 dB free-space filtering grating, 2.5 dB fiber-coupling after filtering and 3 dB detection loss. After accounting for detection loss, we infer a heralding probability of 4.6%. We estimate about 8 dB losses at collection from the SPDC source, primarily due to mode-mismatch and transmission loss from filtering optics.

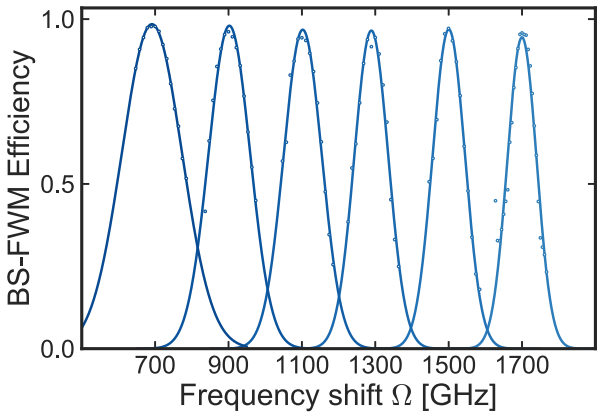

(a)

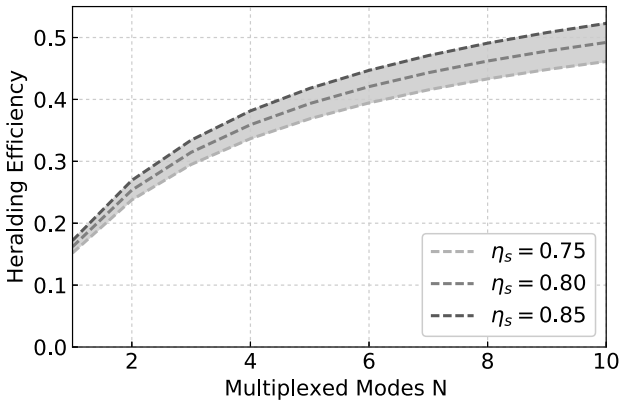

(b)

Figure 3.8: **a)** BS-FWM conversion efficiency for 10 channels separated by 100 GHz. We fix one of the two pumps while detuning the other such that the frequency separation between the two pumps matches the frequency separation between the input and the target. The conversion efficiency is maintained throughout while the acceptance bandwidth is reduced by a factor of 2 due to the effects of higher order dispersion. **b)** Scaling performance of frequency for 10 frequency modes, assuming a combined detection and fiber-collection efficiency of 90%, for varying multiplexing system efficiencies ($\eta_s = 0.75, 0.80, 0.85$). Single-photon heralding efficiencies as high as 50% can be achieved with just 10 frequency modes.

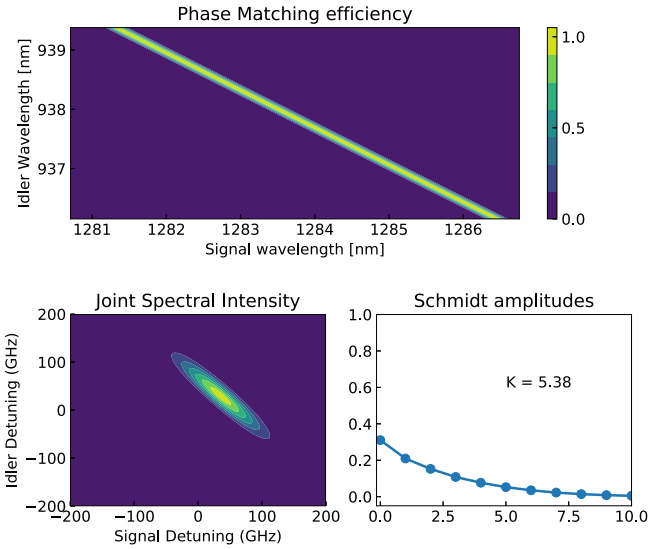

Figure 3.9: Calculated JSI before (top) and after filtering (bottom left) with a 1 cm. The phase-matching condition is tight due to the highly non-degenerate nature of the single-photon source, resulting in strongly correlated photons. The calculated Schmidt number is high (5.38), resulting in low single-photon purity.

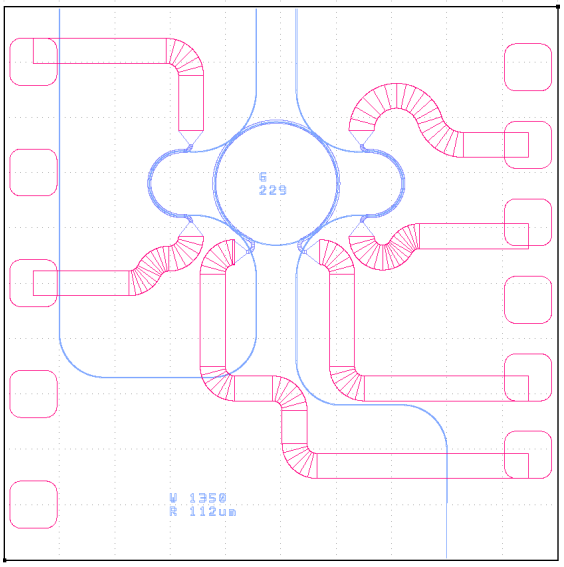

Figure 3.10: **Design for spectrally pure single-photon generation:** A 200 GHz ring resonator with interferometric coupling for both the through and the drop port. The interferometric coupler is such that it suppresses every other resonance of the ring. The gap on the through port is smaller to allow for overcoupling of the pump. The photons are extracted via the drop port (left). The platinum heaters can be used to tune the phase of the coupler to get maximum/minimum transmission at the desired resonator frequencies.

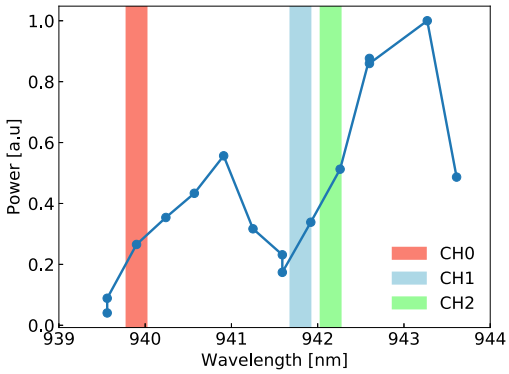

Figure 3.11: Spectrum of the heralding photons measured using a single photon spectrometer. The heralding photons are filtered into 100GHz wide channels using reflecting Bragg gratings. The highlighted regions reflect the corresponding heralded channels: CH0, CH1, CH2.

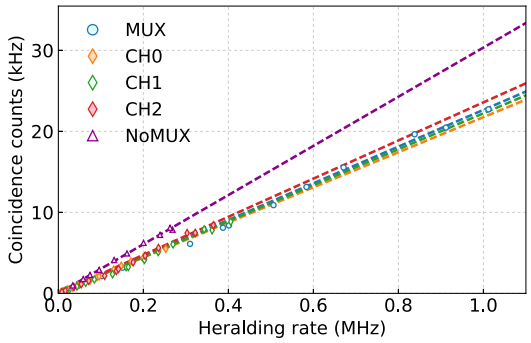

Figure 3.12: Characterization of heralding efficiency. The efficiency is given by the slope of the heralding rate vs heralded photon rate (measured as coincidence counts). We measure a heralding efficiency of 2.3% with the multiplexing setup in place and an efficiency of 3% without. This corresponds with the estimated 1.3 dB transmission loss through the BS-FWM setup measured using a classical input.

CHAPTER 4

FREQUENCY-DOMAIN QUANTUM INTERFERENCE WITH CORRELATED PHOTONS FROM AN INTEGRATED MICRORESONATOR

Two-photon interference is a fundamental quantum effect with no classical analogue. The effect was first observed by Hong, Ou and Mandel in 1987 [90]. In their experiment, two correlated photon wavepackets indistinguishable in their spectro-temporal and polarization properties were overlapped on a spatial-mode beam splitter. They observed that the photons tend to *bunch* in the same arm of the beam splitter and the coincidences between the two arms of the beam splitter go to zero. In this first demonstration, the photon wavepackets were indistinguishable in all properties except their spatial mode at the *input*, subsequent experimental and theoretical work confirms it is the indistinguishability of the two-photon amplitudes at the output of the interferometer that is crucial to the observation of HOM-type interference [91]. In [91], the authors showed that photon wavepackets that do not physically overlap simultaneously on the beam splitter also demonstrate the photon bunching effect. The photons were also propagated over a path length longer their coherence length, demonstrating that the interference effect is insensitive to phase. The crucial insight this experiment provides is that it is not *indivial* photon amplitudes that need to be indistinguishable at the input, but the *two-photon amplitudes* that need to be indistinguishable at the output of the interferometer. In addition to profound fundamental implications, Hong-Ou-Mandel (HOM) interference is the basis of several photonic QIP such as Bell-state measurement, boson sampling, measurement-based logic gates, and the generation of multipartite entangled Greenberger-Horne-Zeilinger (GHZ) and cluster states [92–95].

The insight from previous experiments leads to the interesting possibility of observing quantum interference involving spectrally distinct photons. An ‘active’ device that

coherently mixes two input frequency modes can render distinct spectral amplitudes indistinguishable, resulting in fourth-order interference with the two photons bunched in the same frequency mode [96]. At first, this is counterintuitive, as such spectrally distinct two-photon amplitudes do not interfere on passive devices such as spatial or polarization mode beam splitters. However, when a single photon is incident on one port of such a frequency beam splitter, the resulting output is a photon in a superposition of two distinct frequencies; a bichromatic qubit [2]. When two photons of distinct frequencies are incident on different ports of this device, the two-photon amplitude where both photons undergo frequency conversion destructively interferes with the two-photon amplitude where neither photon gets frequency converted. This results in HOM type interference, with both photons bunching in the same frequency mode with identical frequencies. In this chapter, we report frequency-domain HOM interference with spectrally distinct photons generated from a chip-based microresonator. We use BS-FWM to implement an active 'frequency beam-splitter' and achieve interference visibilities of 0.95 ± 0.02. We show interference with narrow photons less than 300 MHz in bandwidth and widely separated in frequency by 800 GHz. We predict and observe a rich two-photon interference pattern, including the phenomenon of quantum beating in the temporal domain. Moreover, the photons travel in the BS-FWM fiber that is more than 30 times the coherence length of the photons, confirming that the observed quantum beating is not a phase related effect. This result confirms that BS-FWM preserves all quantum properties of the input photon wavepackets and renders the photon frequencies indistinguishable after interaction.

A major motivation for this work is the fact that frequency multiplexing combined fiber and integrated photonic technologies can significantly reduce the complexity and resource requirements for realizing all-photonic quantum networks. Novel approaches for all-photonic quantum repeaters rely on a combination of efficient single-photon sources, linear operations with beam splitters and measurement-based fusion gates

to generate entangled multi-photon Greenberger-Horne-Zeilinger (GHZ) and cluster states [97, 98]. Frequency multiplexing can massively reduce the resource requirements for such all-photonic quantum networks. Frequency domain quantum operations also provide a distinct advantage in terms of the scaling of losses over spatial or polarization mode processing [99, 100]. Cavity-enhanced spontaneous four-wave mixing (SFWM) in integrated microresonators produces frequency-entangled photon pairs with an effectively discrete joint spectral intensity [32, 101–104]. A large number of such compact, identical sources can be integrated on a monolithic platform for the generation and manipulation of complex non-classical states of light [25, 105–107]. This demonstration establishes BS-FWM as a tool for selective, high-fidelity two-photon operations between frequency modes of integrated microresonators.

Creating a device that coherently combines distinct frequency modes is challenging as this requires a strong noise-free nonlinear process. BS-FWM is a unitary, third-order parametric process in which two strong classical pump waves mediate the interaction between the quantum fields via a third order ($\chi^{(3)}$) nonlinearity (Figs. Figure 4.1a and b) [3,8,9,12,108]. By controlling the power and phase of the classical fields involved, we emulate a tunable 'active' frequency beam splitter [2]. For quantum frequency conversion based on $\chi^{(2)}$ nonlinearity, the input and target modes must be placed in different optical bands, typically separated by few tens to a hundred terahertz in order to satisfy energy conservation. Alternatively, electro-optic modulators (EOMs) can impart only small frequency shifts of the order of a few gigahertz. With BS-FWM, the use of two classical fields provides an additional degree of freedom and efficient conversion is possible for separations ranging from a few hundred GHz to a few THz [99]. This makes a BS-FWM frequency beam splitter (FBS) compatible with the typical free spectral range (FSR) of integrated microresonators and also with dense wavelength division multiplexing (DWDM) components aligned to the ITU grid. Prior demonstrations Previously, EOMs

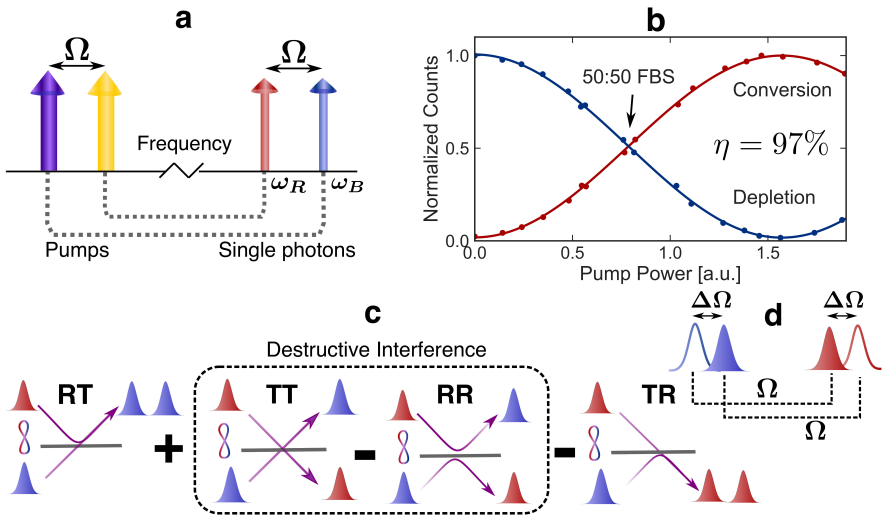

Figure 4.1: Frequency beam splitter via BS-FWM: **a)** Two strong classical pumps $(\omega_{P1}, \omega_{P2})$ mediate the interaction between two quantum fields, (ω_R, ω_B) in a medium with third-order $\chi^{(3)}$ nonlinearity. **b)** Measured signal conversion and depletion (efficiency $\eta = 97\%$). BS-FWM acts as a 50:50 frequency beam splitter (FBS) when the pump power is such that the nonlinear interaction strength $\gamma PL = \pi/8$. **c)** Two frequency-correlated photons incident on a 50:50 FBS. Perfect HOM-type interference is observed when the two-photon amplitude for both photons being frequency translated (RR) and neither photon being translated (TT) are indistinguishable. This occurs when the BS-FWM pump separation Ω matches the input photon-pair separation, resulting in $\Delta\Omega = 0$ (see **d**).

have been used in combination with integrated sources to generate high-dimensional time-frequency entangled states [76, 109–111]. These demonstrations however do not show two-photon HOM interference with photon generated from distinct spectral modes of the microresonator. Due to the limited bandwidth of the EOM, it is challenging to create a deterministic two-mode interaction between frequency modes spaced by hundreds of GHz. EOMs have been used together with pulse shaping and bulk single-photon sources, to create frequency-bin entangled states and to demonstrate two-photon HOM-type interference with modes separated by up to 25 GHz [112–118]. This however requires strong spectral filtering of the single-photon source. Frequency translation in a $\chi^{(2)}$ crystal was used to demonstrate interference between a single photon and attenuated coherent laser light [119], however the visibility was limited due to multi-photon noise

from the coherent state.

4.1 Theoretical predictions

We recall that BS-FWM creates a coherent interaction between two quantum fields at different frequencies (ω_R, ω_B), as shown in Figure 4.1. Energy conservation requires that the frequency separation between the classical pump fields ($\omega_{P1} - \omega_{P2} = \Omega$) should match the separation of the quantum fields ($\omega_B - \omega_R = \Omega$). Phase-matching ($\Delta k = \beta_R + \beta_{P1} - \beta_B - \beta_{P2}, \beta$: propagation constant) can be ensured by placing the pump fields and the quantum fields symmetrically about the zero group-velocity dispersion (GVD, $\beta^{(2)} = 0$) point of the interaction medium. Due to the effects of third-order dispersion ($\beta^{(3)}$), it is possible to ensure selective phase matching such that the resulting process is a two-mode interaction without spurious side-bands (see supplementary Section S1). For such a selectively phased-matched process ($\Delta k = 0$), the two mode solutions were derived in Equation (2.28). For a perfectly phase-matched process ($\Delta\beta = 0$), the mode transformations for signal and idler annihilation operators $\hat{a}(\omega_R), \hat{a}(\omega_B)$ after passing through the FBS are then given by,

$$\begin{aligned} \hat{a}_R(\omega_R) &\rightarrow \upsilon \hat{a}_R(\omega_R) - \mu \hat{a}_B(\omega_R + \Omega), \\ \hat{a}_B(\omega_B) &\rightarrow \mu^* \hat{a}_R(\omega_B - \Omega) + \upsilon^* \hat{a}_B(\omega_B), \end{aligned} \tag{4.1}$$

where $\upsilon = \cos(2\gamma PL), \mu = e^{i\phi} \sin(2\gamma PL)$, Ω is the frequency separation of the two pump fields, $P = \sqrt{P_1 P_2}$ depends on the power P_1, P_2 of the two classical pumps, γ is proportional to the nonlinearity of the interaction medium, L is the interaction length, ϕ is the relative phase between the pumps. The subscripts (R, B) denote the red-detuned and blue-detuned frequencies respectively. As evident from Eq. Equation (4.1) and as demonstrated in Ref. [2], BS-FWM acts as an $SU(2)$ transformation and can produce arbitrary single-qubit rotations in the two-dimensional frequency Hilbert space

$\{|\omega_R\rangle, |\omega_B\rangle\}$.

First, we formally establish that this process can be used for two-photon quantum interference (see Figs. Figure 4.1b and c). We theoretically predict the conditions for observing perfect Hong-Ou-Mandel type interference for two frequency-correlated photons and show that our experimental findings are in excellent agreement with these theoretical predictions. Consider the second-order coherence function $G^{(2)}(\tau)$ for correlated photons generated from a cavity,

$$G^{(2)}(\tau) = \langle E_R^{(-)}(t) E_B^{(-)}(t+\tau) E_B^{(+)}(t+\tau) E_R^{(+)}(t) \rangle \tag{4.2}$$

where the subscripts (R, B) denote the red-detuned and blue-detuned frequencies respectively. The $G^{(2)}(\tau)$ in Equation (4.2) is measured via a coincidence measurement between the red and blue-detuned frequency channels. The electric field operators are related to the quantized annihilation operators as,

$$E^{(+)}(t) = [E^{(-)}(t)]^\dagger \propto \frac{1}{\sqrt{(2\pi)}} \int d\omega \, \hat{a}(\omega) e^{-i\omega t} \tag{4.3}$$

The joint wavefunction of two frequency correlated photons is,

$$|\psi\rangle \propto \int d\omega_B d\omega_R \, \phi(\omega_R, \omega_B) \hat{a}_R^\dagger(\omega_R) \hat{a}_B^\dagger(\omega_B) |0, 0\rangle, \tag{4.4}$$

where $\phi(\omega_R, \omega_B)$ is the joint spectral amplitude (JSA) of the two photons.
Combining Equation (4.2),Equation (4.4) we obtain the $G^{(2)}(\tau)$ of the correlated photons before the frequency splitter to be,

$$G^{(2)}(\tau) \propto \int d\omega_B^{'''} d\omega_R^{'''} d\omega_B^{''} d\omega_R^{''} d\omega_R^{'} d\omega_B^{'} d\omega_R d\omega_B e^{i(\omega_R^{'} - \omega_R)(t+\tau)} e^{i(\omega_B^{'} - \omega_B)t} \phi^\star(\omega_B^{''}, \omega_R^{''}) \phi(\omega_B^{'''}, \omega_R^{'''})$$
$$\langle 0, 0 | \hat{a}_R(\omega_R^{''}) \hat{a}_B(\omega_B{''}) \hat{a}_R^\dagger(\omega_R^{'}) \hat{a}_B^\dagger(\omega_B^{'}) \hat{a}_R(\omega_R) \hat{a}_B(\omega_B) \hat{a}_R^\dagger(\omega_R^{'''}) \hat{a}_B^\dagger(\omega_B^{'''}) | 0, 0 \rangle \tag{4.5}$$

Using the commutation relations $[\hat{a}_R, \hat{a}_B] = 0, [\hat{a}_R, \hat{a}_B^\dagger] = 0, [\hat{a}_R(\omega), \hat{a}_R^\dagger(\omega')] = \delta(\omega - \omega')$

and $[\hat{a}_B(\omega), \hat{a}_B^{\dagger}(\omega^{'})] = \delta(\omega - \omega')$, Eq. Equation (4.5) reduces to,

$$G^{(2)}(\tau) \propto \int d\omega_B^{'''} d\omega_R^{'''} d\omega_B^{''} d\omega_R^{''} d\omega_R^{'} d\omega_B^{'} d\omega_R d\omega_B e^{i(\omega_R^{'}-\omega_R)(t+\tau)} e^{i(\omega_B^{'}-\omega_B)t} \phi^{\star}(\omega_B^{''}, \omega_R^{''}) \phi(\omega_B^{'''}, \omega_R^{'''})$$
$$\delta(\omega_R^{''} - \omega_R^{'}) \delta(\omega_B^{''} - \omega_B^{'}) \delta(\omega_R - \omega_R^{'''}) \delta(\omega_B - \omega_B^{'''}) \quad (4.6)$$

Assuming w.l.o.g that $t = 0$ and evaluating the delta functions simplifies the integral to,

$$G^{(2)}(\tau) \propto \int d\omega_R^{'} d\omega_B^{'} d\omega_R d\omega_B \, e^{i(\omega_R^{'}-\omega_R)\tau} \phi^{\star}(\omega_B^{'}, \omega_R^{'}) \phi(\omega_B, \omega_R). \quad (4.7)$$

$$(4.8)$$

With a CW-pump, the photons generated from the ring resonator are strongly correlated in frequency and the joint spectral amplitude $\phi(\omega_R, \omega_B)$ can be written as,

$$\phi(\omega_B, \omega_R) \propto \delta(\omega_R + \omega_B - 2\omega_P) l(\omega_B, \omega_B^0) l(\omega_R, \omega_R^0) \quad (4.9)$$

where $l(\omega, \omega_0) = \dfrac{(\frac{\Delta\omega}{2})^{\frac{1}{2}}}{[-i(\omega - \omega_0) + \frac{\Delta\omega}{2}]}$, such that $|l(\omega, \omega_0)|^2$ describes a Lorentzian function centered at ω_0 with a full-width at half maximum $\Delta\omega$. We assume that the detuning of the pump with respect to the cavity resonance is given by Δ, such that $\omega_R^0 + \omega_B^0 = 2(\omega_P + \Delta)$ Using the change of variables $\omega_B^{'} \rightarrow \omega_B^{'} - \omega_P, \omega_R^{'} \rightarrow \omega_R^{'} - \omega_P, \omega_B \rightarrow \omega_B - \omega_P, \omega_R \rightarrow \omega_R - \omega_P$, Eq. Equation (4.7) simplifies to:

$$G^{(2)}(\tau) \propto \int d\omega_R^{'} d\omega_B^{'} d\omega_R d\omega_B \, e^{i(\omega_R^{'}-\omega_R)\tau} \delta(\omega_R^{'} + \omega_B^{'}) \delta(\omega_R + \omega_B) \, l^{\star}(\omega_R^{'}, \Delta) l^{\star}(\omega_B^{'}, \Delta) l(\omega_R, \Delta) l(\omega_B, \Delta) \quad (4.10)$$

Evaluating the delta functions, the integral simplifies to,

$$G^{(2)}(\tau) \propto \int d\omega_B^{'} d\omega_B \, e^{i(-\omega_B^{'}+\omega_B)\tau} \, l^{\star}(-\omega_B^{'}, \Delta) l^{\star}(\omega_B^{'}, \Delta) l(-\omega_B, \Delta) l(\omega_B, \Delta) \quad (4.11)$$
$$= \int d\omega_B^{'} e^{-i\omega_B^{'}\tau} l^{\star}(-\omega_B^{'}, \Delta) l^{\star}(\omega_B^{'}, \Delta) \int e^{i\omega_B\tau} d\omega_B l(-\omega_B, \Delta) l(\omega_B, \Delta) \quad (4.12)$$

Explicitly evaluating the integrals results in the final form,

$$G^{(2)}(\tau) \propto \frac{\left(\frac{\Delta\omega}{2}\right)^2}{2\pi\left(\Delta^2 + \left(\frac{\Delta\omega}{2}\right)^2\right)} e^{-\Delta\omega|\tau|}. \tag{4.13}$$

As expected, the second-order correlation function in the time-domain is the Fourier transform of the joint spectral intensity of the two photons in the frequency domain.

We now calculate the second-order correlation function after the frequency beam splitter. Combining Equation (4.2),Equation (4.4),Equation (4.1) we obtain the $G^{(2)}(\tau)$ after the beam splitter,

$$\begin{aligned} G^{(2)}(\tau) \propto \int d\omega_B^{'''} d\omega_R^{'''} d\omega_B^{''} d\omega_R^{''} d\omega_R^{'} d\omega_B^{'} d\omega_R d\omega_B \, e^{i(\omega_R^{'}-\omega_R)\tau} \phi^{\star}(\omega_B^{''}, \omega_R^{''}) \phi(\omega_B^{'''}, \omega_R^{'''}) \\ \langle 0,0|\hat{a}_R(\omega_R^{''})\hat{a}_B(\omega_B{''})[\upsilon\hat{a}_R^{\dagger}(\omega_R^{'}) - \mu\hat{a}_B^{\dagger}(\omega_R^{'}+\Omega)] \\ [\mu\hat{a}_R^{\dagger}(\omega_B^{'}-\Omega) + \upsilon\hat{a}_B^{\dagger}(\omega_B^{'})] \\ [\mu^{\star}\hat{a}_R(\omega_B-\Omega) + \upsilon^{\star}\hat{a}_B(\omega_B)] \\ [\upsilon^{\star}\hat{a}_R(\omega_R) - \mu^{\star}\hat{a}_B(\omega_R+\Omega)]\, \hat{a}_R^{\dagger}(\omega_R^{'''})\hat{a}_B^{\dagger}(\omega_B^{'''})|0,0\rangle \end{aligned} \tag{4.14}$$

where we assume that the integration limits are well within the phase-matching bandwidth of BS-FWM. Retaining only the non-zero terms in the above expression,

$$\begin{aligned} G^{(2)}(\tau) \propto \int d\omega_B^{'''} d\omega_R^{'''} d\omega_B^{''} d\omega_R^{''} d\omega_R^{'} d\omega_B^{'} d\omega_R d\omega_B \, e^{i(\omega_R^{'}-\omega_R)\tau} \phi^{\star}(\omega_B^{''}, \omega_R^{''}) \phi(\omega_B^{'''}, \omega_R^{'''}) \\ \langle 0,0|\hat{a}_R(\omega_R^{''})\hat{a}_B(\omega_B{''})[|\upsilon|^4\hat{a}_R^{\dagger}(\omega_R^{'})\hat{a}_B^{\dagger}(\omega_B^{'})\hat{a}_R(\omega_R)\hat{a}_B(\omega_B) \\ +|\mu|^4\hat{a}_R^{\dagger}(\omega_B^{'}-\Omega)\hat{a}_B^{\dagger}(\omega_R^{'}+\Omega)\hat{a}_R(\omega_B-\Omega)\hat{a}_B(\omega_R+\Omega) \\ -|\upsilon|^2|\mu|^2\hat{a}_R^{\dagger}(\omega_R^{'})\hat{a}_B^{\dagger}(\omega_B^{'})\hat{a}_R(\omega_B-\Omega)\hat{a}_B(\omega_R+\Omega) \\ -|\upsilon|^2|\mu|^2\hat{a}_R^{\dagger}(\omega_B^{'}-\Omega)\hat{a}_B^{\dagger}(\omega_R^{'}+\Omega)\hat{a}_R(\omega_R)\hat{a}_B(\omega_B)]\hat{a}_R^{\dagger}(\omega_R^{'''})\hat{a}_B^{\dagger}(\omega_B^{'''})|0,0\rangle \end{aligned} \tag{4.15}$$

As before, using standard commutation relations, Eq. Equation (4.15) reduces to,

$$
\begin{aligned}
G^{(2)}(\tau) \propto \int & d\omega_B^{'''} d\omega_R^{'''} d\omega_B^{''} d\omega_R^{''} d\omega_R^{'} d\omega_B^{'} d\omega_R d\omega_B \, e^{i(\omega_R^{'}-\omega_R)\tau} \phi^{\star}(\omega_B^{''}, \omega_R^{''}) \phi(\omega_B^{'''}, \omega_R^{'''}) \\
& [|\upsilon|^4 \delta(\omega_B^{''} - \omega_B^{'}) \delta(\omega_B - \omega_B^{'''}) \delta(\omega_R^{''} - \omega_R^{'}) \delta(\omega_R - \omega_R^{'''}) \\
& + |\mu|^4 \delta(\omega_R^{''} - \omega_B^{'} + \Omega) \delta(\omega_B^{''} - \omega_R^{'} - \Omega) \delta(\omega_B - \Omega - \omega_R^{'''}) \delta(\omega_R + \Omega - \omega_B^{'''}) \\
& - |\upsilon|^2 |\mu|^2 \delta(\omega_R^{''} - \omega_R^{'}) \delta(\omega_B^{''} - \omega_B^{'}) \delta(\omega_B - \Omega - \omega_R^{'''}) \delta(\omega_R + \Omega - \omega_B^{'''}) \\
& - |\upsilon|^2 |\mu|^2 \delta(\omega_R^{''} - \omega_B^{'} + \Omega) \delta(\omega_B^{''} - \omega_R^{'} - \Omega) \delta(\omega_R - \omega_R^{'''}) \delta(\omega_B - \omega_B^{'''})]. \qquad (4.16)
\end{aligned}
$$

Evaluating the delta functions gives,

$$
\begin{aligned}
G^{(2)}(\tau) = \int & d\omega_R^{'} d\omega_B^{'} d\omega_R d\omega_B \, e^{i(\omega_R^{'}-\omega_R)\tau} \\
& [|\upsilon|^4 \phi^{\star}(\omega_B^{'}, \omega_R^{'}) \phi(\omega_B, \omega_R) \\
& + |\mu|^4 \phi^{*}(\omega_R^{'} + \Omega, \omega_B^{'} - \Omega) \phi(\omega_R + \Omega, \omega_B - \Omega) \\
& - |\upsilon|^2 |\mu|^2 \phi^{*}(\omega_B^{'}, \omega_R^{'}) \phi(\omega_R + \Omega, \omega_B - \Omega) \\
& - |\upsilon|^2 |\mu|^2 \phi^{*}(\omega_R^{'} + \Omega, \omega_B^{'} - \Omega) \phi(\omega_B, \omega_R)]. \qquad (4.17)
\end{aligned}
$$

As before, we use the joint spectral amplitude $\phi(\omega_B, \omega_R)$ is given by Eq. Equation (4.9), assume that the SFWM pump is detuned by Δ with respect to the cavity resonance, and introduce the variable $\Delta\Omega = \Omega - (\omega_B^0 - \omega_R^0)$ to get:

$$
\begin{aligned}
G^{(2)}(\tau) = |\upsilon|^4 & \int d\omega_B^{'} e^{-i\omega_B^{'}\tau} l^{\star}(-\omega_B^{'}, \Delta) l^{\star}(\omega_B^{'}, \Delta) \int e^{i\omega_B\tau} d\omega_B l(-\omega_B, \Delta) l(\omega_B, \Delta) \\
& + |\mu|^4 \int d\omega_B^{'} e^{-i\omega_B^{'}\tau} l^{\star}(-\omega_B^{'} + \Delta\Omega, \Delta) l^{\star}(\omega_B^{'} - \Delta\Omega, \Delta) \int d\omega_B e^{i\omega_B\tau} l(-\omega_B + \Delta\Omega, \Delta) l(\omega_B - \Delta\Omega, \Delta) \\
& - |\upsilon|^2 |\mu|^2 \int d\omega_B^{'} e^{-i\omega_B^{'}\tau} l^{\star}(-\omega_B^{'}, \Delta) l^{\star}(\omega_B^{'}, \Delta) \int e^{i\omega_B\tau} d\omega_B l(-\omega_B + \Delta\Omega, \Delta) l(\omega_B - \Delta\Omega, \Delta) \\
& - |\upsilon|^2 |\mu|^2 \int d\omega_B^{'} e^{-i\omega_B^{'}\tau} l^{\star}(-\omega_B^{'} + \Delta\Omega, \Delta) l^{\star}(\omega_B^{'} - \Delta\Omega, \Delta) \int e^{i\omega_B\tau} d\omega_B l(-\omega_B, \Delta) l(\omega_B, \Delta)]. \\
& \qquad (4.18)
\end{aligned}
$$

Explicitly evaluating the integrals results in the expression,

$$
G^{(2)}(\tau) \propto \frac{\left(\frac{\Delta\omega}{2}\right)^2}{2\pi\left(\Delta^2 + \left(\frac{\Delta\omega}{2}\right)^2\right)} e^{-\Delta\omega|\tau|} \left(|\upsilon|^4 + |\mu|^4 - |\mu|^2|\upsilon|^2 e^{-i\Delta\Omega\tau} - |\mu|^2|\upsilon|^2 e^{i\Delta\Omega\tau}\right) \qquad (4.19)
$$

When the frequency beam splitter is set such that $\mu = \frac{1}{\sqrt{2}}, \upsilon = \frac{1}{\sqrt{2}}$ we obtain,

$$G^{(2)}(\tau) \propto \frac{\left(\frac{\Delta\omega}{2}\right)^2}{2\pi\left(\Delta^2 + \left(\frac{\Delta\omega}{2}\right)^2\right)} e^{-\Delta\omega|\tau|}\left(\frac{1}{2} - \frac{1}{2}\cos(\Delta\Omega\tau)\right)$$
$$\propto \frac{\left(\frac{\Delta\omega}{2}\right)^2}{2\pi\left(\Delta^2 + \left(\frac{\Delta\omega}{2}\right)^2\right)} e^{-\Delta\omega|\tau|}\sin^2\left(\frac{\Delta\Omega\tau}{2}\right). \tag{4.20}$$

where we have introduced the variable $\Delta\Omega = \Omega - (\omega_B^0 - \omega_R^0)$ to reflect the offset between the frequency separation Ω of the BS-FWM pumps with respect to the separation of the photon envelopes centered at ω_B^0 and ω_R^0. Equation Equation (4.20) shows that the observed interference depends sensitively on the offset $\Delta\Omega$. When $\Delta\Omega = 0$, $G^{(2)}(\tau) = 0$ for all τ, as expected from the fact that two-photon wavefunction before and after frequency translation are completely indistinguishable ($\phi(\omega_B, \omega_R) = \phi(\omega_B - \Omega, \omega_R + \Omega)$). For offsets $\Delta\Omega$ that are small or comparable to the resonator linewidth $\Delta\omega$, the phenomenon of quantum beating is predicted [120]. We note that this beating can only be resolved if $2\pi/\Delta\Omega$ is much larger than the temporal resolution of the single-photon detectors [121].

Single photon source

A detailed experimental setup is shown in Figure 4.5. An external cavity diode laser (TOPTICA DL 100) at 1282.8 nm in combination with a fiber amplifier is used as the spontaneous four-wave mixing (SFWM) pump. In order to reject noise from amplified spontaneous emission (ASE) from the laser and the amplifier, we strongly filter the pump before the chip. We use a combination of fiber bragg gratings (FBG, OEland, center wavelength:1282.8 nm, bandwidth: 0.8 nm) and a free space grating filter to obtain more than 40 dB suppression of ASE noise at the photon wavelength, as shown in Figure 4.5a. The filtered pump is then coupled into the bus waveguide of the microresonator using

a lensed fiber. An integrated platinum heater driven by a current controller (Thorlabs LDC 200) is used to tune the resonance of the microring to the SFWM pump. The input is aligned to the transverse magnetic (TM) mode of the microring. The output is collected with an aspheric lens, passed through a polarizer aligned to select the TM polarization and then coupled into a single-mode fiber. The residual SFWM pump is rejected using FBGs. A circulator is used to extract this reflected residual pump and this pump power is monitored on an InGaAs photodiode. The output of the photodiode is used to continuously maintain the microring at a fixed detuning with respect to the SFWM pump via a PID feedback control loop (STEMLab Red Pitaya), on the integrated heaters (thermo-optic effect). For coincidence measurement, the two photon frequencies (ω_R, ω_B) are further separated using an O-band WDM (Passband: 1290 ± 6.5 nm). Two multi-pass grating filters are then used to reject residual noise from the BS-FWM and SFWM pumps by more than 50 dB. This strong filtering results in an excellent coincidences to accidentals ratio of 60 (see Figure 4.5c). The total loss on each photon arm from generation to detection is measured to be 15 dB. The photons are detected using superconducting nanowire single-photon detectors (SNSPDs, Photon Spot, quantum efficiency: 53% at 1300 nm). We extract a photon bandwidth of 270 ± 15 MHz from the measured two-fold coincidences for our photon source (Figure 4.5c).

Measurement of free spectral range (FSR)

The free spectral range of the microresonator is precisely characterized using higher-order sidebands generated using a phase modulator. The CW laser at 1282.8 nm is sent to a phase modulator (JDS Uniphase, 11 GHz bandwidth) and strongly driven at ν_{RF} = 25 GHz using an RF generator (Keysight). The modulated output is sent to the ring resonator and the transmission of the higher-order sidebands up to the 4th order

($\nu_{CW} + 4\nu_{RF}, \nu_{CW} - 4\nu_{RF}$) are monitored on an Optical Spectrum Analyzer (OSA). The RF frequency is changed in steps of 10 MHz until we observe simultaneous extinction of the two fourth-order sidebands. We measure this frequency to be $\nu_{RF} = 25.16$ GHz. This results in a measured FSR = $8\nu_{RF} = 201.275$ GHz. We select photon pairs located two FSRs away from the SFWM pump, resulting in a photon separation of 805.1 GHz. The photon bandwidth is extracted from a fit to the measured $G^{(\tau)}$, as show in Figure 4.5.

BS-FWM setup

The BS-FWM setup used in our experiment is similar to that in Ref. [2]. The BS-FWM pumps are prepared as shown in Figure 4.5. Two tunable external cavity diode lasers are used as the BS-FWM pumps. The wavelengths of the pumps are monitored on a wavemeter (Burleigh 1600, 30 MHz resolution) in order to maintain the pump separation Ω throughout the experiment. Electro-optic modulators (EOMs) driven at a 2 MHz repetition rate are used to carve out 10-ns pulses from the CW lasers. The pumps are pre-amplified using erbium doped fiber amplifiers (EDFA, Amonics), combined using dense wavelength division multiplexer (DWDM) aligned to the ITU-grid. The pumps are then amplified to a peak power of 10 W using a high power EDFA. The pumps are combined with the photons using a WDM and sent to a 100-m long dispersion shifted fiber (Corning Vistacor) for BS-FWM. The efficiency of frequency conversion is calibrated with respect to the BS-FWM pump power by monitoring the depletion of an attenuated coherent state at the wavelength of the photons. The polarizations of the BS-FWM pumps are aligned to the linear polarization of the input state to achieve more than 95% depletion. The pump power is then set to obtain 50% percent depletion such that the photons now see a device that emulates a 50:50 FBS. Following the nonlinear process, the pumps and the photons are separated using another WDM. For coincidence measurement, the two

photon frequencies (ω_R, ω_B) are further separated using an O-band WDM (Passband: 1290 ± 6.5 nm). Two multi-pass grating filters are then used to reject residual noise from the BS-FWM and SFWM pumps by more than 50 dB. Our high reported visibilities are indicative of the long term stability of our experimental setup.

System loss characterization

BS-FWM

We measure a total of 1.3 dB loss due to our Bragg-scattering four-wave mixing setup [99], including the wavelength-division multiplexers (WDMs) to combine the pumps and the photons, the 100-m dispersion shifted fiber and the fiber-based filters for BS-FWM pump rejection after the nonlinear process.

Single-photon source

At the output of the chip, the generated photons and residual pumps are collected using an aspheric lens, passed through a polarizer and then coupled into a single mode fiber. We measure a total of 3 dB loss through this collection setup. The 3 fiber bragg-gratings used for SFWM-pump rejection have a combined loss of 3 dB. The two photons are separated via a WDM (1 dB loss) and sent to free-space grating filters (1.5 dB loss) and collected into single-mode fibers (3.5 dB loss). We estimate the quantum efficiency of the superconducting nanowire single photon detectors to be 53% at 1300 nm. The total loss on each photon arm is 15 dB from generation to detection.

Three-fold coincidence measurement

In order to post-select only those photon coincidences that occur within the 10-nanosecond window of the BS-FWM pumps, we perform a three-fold coincidence measurement between the arrival time of the photons at the SNSPDs and a synchronization signal from the pump (Figure 4.5b). We then obtain suitable normalization by averaging over coincidences accumulated in 10-ns temporal windows that are not synchronized with the BS-FWM pumps. This data is obtained by post-processing all time tags collected on the three channels during an hour long measurement. Raw visibilities are reported using statistics accumulated over time bins of $\delta t = 160$ ps. Fit visibilities are calculated by integrating fit to the data around $\tau = 0$ over one time bin δt. The reported visibilities α are obtained according to the definition,

$$G^{(2)}(\tau) \propto e^{-\Delta\omega|\tau|}\left(\frac{1}{2} - \frac{\alpha}{2}\cos\Delta\Omega\tau\right) \tag{4.21}$$

To calculate α, we extract the extinction of ratio at $\tau = 0$ of data post selected in the presence of BS-FWM pumps (red curves, 3 maintext) with respect to half the peak of the normalization (blue curves, 3 maintext). This definition is consistent with the fact that we report a visibility $\alpha = 0$ for large detunings $\Delta\Omega = 5$ GHz. We note that that there is no background subtraction in any of our reported visibilities.

4.2 Experiment

We experimentally demonstrate this detuning-dependent HOM interference in agreement with these theoretical predictions using the scheme depicted in Figure 4.2. A silicon nitride microresonator is pumped with a continuous-wave (CW) laser at 1282.8 nm to generate frequency-correlated photon pairs in the O-band through SFWM. The generated

photons are coupled into a single-mode fiber and combined with the classical pump fields located in the C-band for BS-FWM and sent to a dispersion-shifted fiber (Corning Vistacor). The BS-FWM pumps are intensity modulated to generate 10-ns long pulses that are amplified with an erbium-doped fiber amplifier. The polarizations of the BS-FWM pumps are aligned to the linear polarization of the input state to achieve more than 95% depletion. The pump power is then set to obtain 50% depletion such that the photons now see a device that emulates a 50:50 FBS. The two frequency arms are separated using a WDM followed by free space grating filters to extract photons that are red detuned (centered at ω_R^0) and blue detuned (centered at ω_B^0) by two FSRs with respect to the SFWM pump. The photons are then detected with superconducting nanowire single photon detectors, followed by coincidence counting using a time-tagging module. In order to match the BS-FWM pump separation Ω precisely to that of the two photons ($\omega_B^0 - \omega_R^0$), we perform a precise measurement of the FSR with a phase modulator (see Supplementary Section 3). We measure an FSR of 201.275 GHz, resulting in a photon separation $(\omega_B^0 - \omega_R^0)/2\pi = 805.1$ GHz. We provide additional details and characterization of the BS-FWM setup in Section 4.4

4.3 Results: Quantum beating and photon bunching

Our experimental results are shown in Figure 4.3 and are in excellent agreement with our theoretical predictions. We obtain a photon bandwidth $\Delta\omega/2\pi = 270 \pm 15$ MHz from the measured cross-correlation $G^{(2)}(\tau)$. In order to post-select only those photon coincidences that occur within the 10-ns temporal window of the BS-FWM pumps, we perform a three-fold coincidence measurement with the arrival time of the two photons at the SNSPDs and a synchronization signal from the pumps. We then obtain suitable normalization by averaging over coincidences accumulated in 10-ns temporal windows

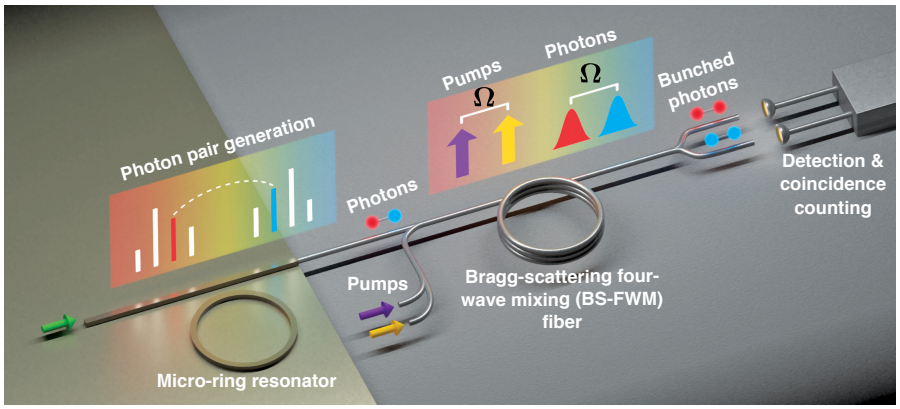

Figure 4.2: **Frequency domain two-photon interference via BS-FWM**: Narrowband frequency-correlated photons are generated via spontaneous four-wave mixing (SFWM) in a silicon nitride microring resonator. The generated photons are coupled together with two classical pump waves through a WDM into a dispersion-shifted fiber for Bragg-scattering four-wave mixing (BS-FWM). The power of the BS-FWM pumps is set such that it acts as a 50:50 frequency beam splitter and their frequency separation Ω is set to precisely match the selected pair of correlated photons. After the nonlinear interaction, the two frequency arms are separated through a WDM followed by detection and coincidence counting. Hong-Ou-Mandel type interference is observed and both photons are bunched in the same frequency mode.

that are not synchronized with the BS-FWM pumps (Figure 4.3, blue curves, see also Supplementary Section 3). For an integration time of one hour, we measure 2700 three-fold normalization coincidence counts within the $1/e$ coherence time of the photons. We introduce a visibility parameter α in Eq. Equation (4.20),

$$G^{(2)}(\tau) \propto e^{-\Delta\omega|\tau|}\left(\frac{1}{2} - \frac{\alpha}{2}\cos\frac{\Delta\Omega\tau}{2}\right) \tag{4.22}$$

This visibility parameter α corresponds the depth of the beating signal at $\tau = 0$ and is a direct indicator of the fidelity of our 50:50 FBS and the indistinguishability of the two-photon amplitude before and after frequency translation. Any distinguishability in other degrees of freedom such as polarization or deviation from the balanced splitting ratio degrades this extinction. As expected, when the offset $\Delta\Omega$ is zero, we observe nearly complete destructive interference resulting in a flat $G^{(2)}(\tau)$. We measure a raw visibility of $\alpha_r = 0.90 \pm 0.03$ from the data and extract a visibility $\alpha_f = 0.92 \pm 0.05$

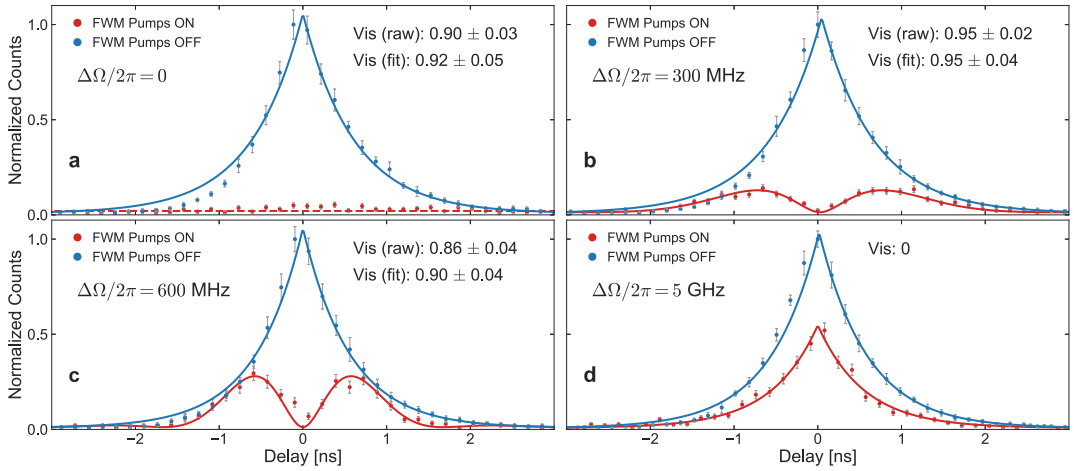

Figure 4.3: **Experimental observation of frequency domain two-photon interference**. Red curves and blue curves (dots: experiment, solid line: fit) are the normalized three-fold coincidence counts when the BS-FWM pumps are on and off, respectively. The photon bandwidth is measured to be 270 ± 15 MHz. **a)** When $\Delta\Omega = 0$, we observe a flat $G^{(2)}(\tau)$ with a raw visibility $\alpha_r = 0.90 \pm 0.03$ (fit visibility $\alpha_f = 0.92 \pm 0.05$. **b)** For a detuning $\Delta\Omega/2\pi = 300$ MHz, we observe temporal beating with a raw visibility $\alpha_r = 0.95 \pm 0.02$ (fit visibility $\alpha_f = 0.95 \pm 0.04$). **c)** For $\Delta\Omega/2\pi = 600$ MHz, we observe an increase in the amplitude of the side lobes of the beating signal with a measured raw visibility of $\alpha_r = 0.86 \pm 0.04$ (fit visibility $\alpha_f = 0.90 \pm 0.04$). **d)** For very large detuning ($\Delta\Omega/2\pi = 5$ GHz), the interference fringes are no longer resolved resulting in a double-exponential output ($\alpha = 0$). Error bars are calculated assuming Poisson statistics.

from fit to the data (Figure 4.3a, red curve). For $\Delta\Omega/2\pi = 300$ MHz, we obtain a raw visibility of $\alpha_r = 0.95 \pm 0.02$ (fit visibility $\alpha_f = 0.95 \pm 0.04$, Figure 4.3b). The high visibility of these measurements indicates that BS-FWM preserves the polarization and spatio-temporal modes of the input quantum fields after frequency translation. For higher detunings $\Delta\Omega = 600$ MHz, we see the expected increase in the amplitude of the side lobes (Figure 4.3c). We measure an interference visibility of $\alpha_r = 0.86 \pm 0.04$ (fit visibility $\alpha_f = 0.90 \pm 0.04$) from this detuning. The reduced raw visibilities in these measurements are due to fluctuations in polarization and pump power during the hour-long measurement, and due to multi-photon noise (see Supplementary Section 3) [28, 64]. For large detuning, $\Delta\Omega/2\pi = 5$ GHz, the interference fringes are no longer resolved by the detection system, resulting in a double-exponential output ($\alpha = 0$) as shown in

Detuning $\Delta\Omega$ (MHz)	Raw Visibility (α_r)	Fit Visibility (α_f)
0	0.90 ± 0.03	0.92 ± 0.05
300	0.95 ± 0.02	0.95 ± 0.04
600	0.86 ± 0.04	0.90 ± 0.04

Table 4.1: **Measured two-photon interference visibilities:** The measured raw visibilities (α_r) are consistent with the visibilities extracted from fit to the data (α_f) within our measurement error, indicating excellent agreement between our theory and experiment.

Figure 4.3d. Our results are summarized in Table 1. The measured raw visibilities are consistent with the visibilities extracted from fit to the data within our measurement error, indicating excellent agreement between our theoretical predictions and experiment.

We emphasize that we are observing interference of the joint two-photon amplitudes before and after the nonlinear process, rather than that of the individual probability amplitudes of the photons themselves. This is evident from the fact that the photons travel a distance that is much longer than the coherence length of the SFWM pumps in the 100-m long BS-FWM fiber [91].

The 50:50 FBS stochastically bunches photons to the same frequency mode with a probability $1/4$ even in the absence of two-photon interference (Figure 4.3d, red curve). This probability is enhanced by a factor of 2 in the presence of two-photon interference, resulting in near-perfect coalescence. We experimentally confirm this enhancement in bunching with a second-order auto correlation measurement on the blue-detuned (ω_B) frequency arm. As shown in Figure 4.4, we observe an enhancement for small pump detunings $\Delta\Omega/2\pi$ = 300 MHz as compared to the case with large pump detunings $\Delta\Omega/2\pi$ = 5 GHz, with a measured peak autocorrelation of 1.93 ± 0.13.

In conclusion, we have demonstrated two-photon interference in the frequency domain using an on-chip photon source with visibilities as high as 95%. In contrast to experiments based on bulk photon sources and free-space optics, we observe interference in a single

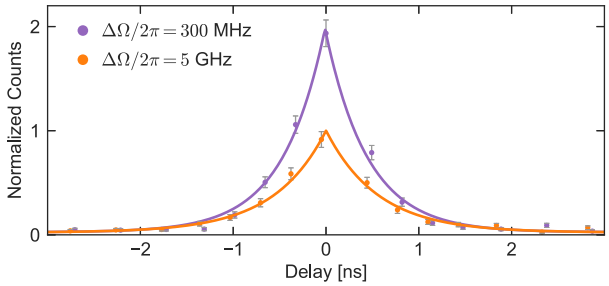

Figure 4.4: **Photon bunching via autocorrelation**. Measured enhancement in two-photon bunching for small (purple, $\Delta\Omega/2\pi = 300$ MHz) over large pump detunings (orange, $\Delta\Omega/2\pi = 5$ GHz) with a measured peak autocorrelation of 1.93 ± 0.13.

spatial mode, and do not require active stabilization or alignment of interferometric paths to achieve high visibility. Selective two-photon operations are possible between arbitrary pairs of resonator modes over a large bandwidth up to a few THz (see Supplementary Figure 1d) [99]. While multiplexing several two-photon operations will be associated with a classical resource overhead for the preparation of additional BS-FWM pumps, no additional components or losses are introduced in the paths of the photons (see Supplementary Section 4). Our demonstration can be extended to spectrally pure single-photons generated via pulsed excitation of the microresonator [43, 122]. Together with implementations of BS-FWM in nanophotonic devices [123–126], such two photon operations can be used for the on chip generation of multipartite entangled GHZ and cluster states. Our demonstration offers a path to combining on-chip photon sources, fiber-based wavelength division multiplexing and four-wave mixing for the realization of scalable frequency-multiplexed photonic quantum repeaters and networks.

4.4 Additional system characterization

4.4.1 Single Photon Source

A detailed experimental setup is shown in Figure 4.5. An external cavity diode laser (TOPTICA DL 100) at 1282.8 nm in combination with a fiber amplifier is used as the spontaneous four-wave mixing (SFWM) pump. In order to reject noise from amplified spontaneous emission (ASE) from the laser and the amplifier, we strongly filter the pump before the chip. We use a combination of fiber bragg gratings (FBG, OEland, center wavelength:1282.8 nm, bandwidth: 0.8 nm) and a free space grating filter to obtain more than 40 dB suppression of ASE noise at the photon wavelength, as shown in Figure 4.5a. The filtered pump is then coupled into the bus waveguide of the microresonator using a lensed fiber. An integrated platinum heater driven by a current controller (Thorlabs LDC 200) is used to tune the resonance of the microring to the SFWM pump. The input is aligned to the transverse magnetic (TM) mode of the microring. The output is collected with an aspheric lens, passed through a polarizer aligned to select the TM polarization and then coupled into a single-mode fiber. The residual SFWM pump is rejected using FBGs. A circulator is used to extract this reflected residual pump and this pump power is monitored on an InGaAs photodiode. The output of the photodiode is used to continuously maintain the microring at a fixed detuning with respect to the SFWM pump via a PID feedback control loop (STEMLab Red Pitaya), on the integrated heaters (thermo-optic effect). For coincidence measurement, the two photon frequencies (ω_R, ω_B) are further separated using an O-band WDM (Passband: 1290 ± 6.5 nm). Two multi-pass grating filters are then used to reject residual noise from the BS-FWM and SFWM pumps by more than 50 dB. This strong filtering results in an excellent coincidences to accidentals ratio of 60 (see Figure 4.5c). The total loss on each photon

arm from generation to detection is measured to be 15 dB. The photons are detected using superconducting nanowire single-photon detectors (SNSPDs, Photon Spot, quantum efficiency: 53% at 1300 nm). We extract a photon bandwidth of 270 ± 15 MHz from the measured two-fold coincidences for our photon source (Figure 4.5c).

4.4.2 Measurement of Free Spectral Range (FSR)

The free spectral range of the microresonator is precisely characterized using higher-order sidebands generated using a phase modulator. The CW laser at 1282.8 nm is sent to a phase modulator (JDS Uniphase, 11 GHz bandwidth) and strongly driven at ν_{RF} = 25 GHz using an RF generator (Keysight). The modulated output is sent to the ring resonator and the transmission of the higher-order sidebands up to the 4th order ($\nu_{CW} + 4\nu_{RF}, \nu_{CW} - 4\nu_{RF}$) are monitored on an Optical Spectrum Analyzer (OSA). The RF frequency is changed in steps of 10 MHz until we observe simultaneous extinction of the two fourth-order sidebands. We measure this frequency to be ν_{RF} = 25.16 GHz. This results in a measured FSR = $8\nu_{RF}$ = 201.275 GHz. We select photon pairs located two FSRs away from the SFWM pump, resulting in a photon separation of 805.1 GHz. The photon bandwidth is extracted from a fit to the measured $G^{(\tau)}$, as show in Figure 4.5.

BS-FWM Setup

The BS-FWM setup used in our experiment is similar to that in Ref. [2]. The BS-FWM pumps are prepared as shown in Figure 4.5. Two tunable external cavity diode lasers are used as the BS-FWM pumps. The wavelengths of the pumps are monitored on a wavemeter (Burleigh 1600, 30 MHz resolution) in order to maintain the pump separation

Ω throughout the experiment. Electro-optic modulators (EOMs) driven at a 2 MHz repetition rate are used to carve out 10-ns pulses from the CW lasers. The pumps are pre-amplified using erbium doped fiber amplifiers (EDFA, Amonics), combined using dense wavelength division multiplexer (DWDM) aligned to the ITU-grid. The pumps are then amplified to a peak power of 10 W using a high power EDFA. The pumps are combined with the photons using a WDM and sent to a 100-m long dispersion shifted fiber (Corning Vistacor) for BS-FWM. The efficiency of frequency conversion is calibrated with respect to the BS-FWM pump power by monitoring the depletion of an attenuated coherent state at the wavelength of the photons. The polarizations of the BS-FWM pumps are aligned to the linear polarization of the input state to achieve more than 95% depletion. The pump power is then set to obtain 50% percent depletion such that the photons now see a device that emulates a 50:50 FBS. Following the nonlinear process, the pumps and the photons are separated using another WDM. For coincidence measurement, the two photon frequencies (ω_R, ω_B) are further separated using an O-band WDM (Passband: 1290 ± 6.5 nm). Two multi-pass grating filters are then used to reject residual noise from the BS-FWM and SFWM pumps by more than 50 dB. Our high reported visibilities are indicative of the long term stability of our experimental setup.

4.4.3 System Loss Characterization

BS-FWM

We measure a total of 1.3 dB loss due to our Bragg-scattering four-wave mixing setup [99], including the wavelength-division multiplexers (WDMs) to combine the pumps and the photons, the 100-m dispersion shifted fiber and the fiber-based filters for BS-FWM pump rejection after the nonlinear process.

Single-Photon Source

At the output of the chip, the generated photons and residual pumps are collected using an aspheric lens, passed through a polarizer and then coupled into a single mode fiber. We measure a total of 3 dB loss through this collection setup. The 3 fiber bragg-gratings used for SFWM-pump rejection have a combined loss of 3 dB. The two photons are separated via a WDM (1 dB loss) and sent to free-space grating filters (1.5 dB loss) and collected into single-mode fibers (3.5 dB loss). We estimate the quantum efficiency of the superconducting nanowire single photon detectors to be 53% at 1300 nm. The total loss on each photon arm is 15 dB from generation to detection.

4.4.4 Three-fold coincidence measurement

In order to post-select only those photon coincidences that occur within the 10-nanosecond window of the BS-FWM pumps, we perform a three-fold coincidence measurement between the arrival time of the photons at the SNSPDs and a synchronization signal from the pump (Figure 4.5b). We then obtain suitable normalization by averaging over coincidences accumulated in 10-ns temporal windows that are not synchronized with the BS-FWM pumps. This data is obtained by post-processing all time tags collected on the three channels during an hour long measurement. Raw visibilities are reported using statistics accumulated over time bins of $\delta t = 160$ ps. Fit visibilities are calculated by integrating fit to the data around $\tau = 0$ over one time bin δt. The reported visibilities α are obtained according to the definition,

$$G^{(2)}(\tau) \propto e^{-\Delta\omega|\tau|}\left(\frac{1}{2} - \frac{\alpha}{2}\cos\Delta\Omega\tau\right) \tag{4.23}$$

To calculate α, we extract the extinction of ratio at $\tau = 0$ of data post selected in the presence of BS-FWM pumps (red curves, 3 maintext) with respect to half the peak of the

normalization (blue curves, 3 maintext). This definition is consistent with the fact that we report a visibility $\alpha = 0$ for large detunings $\Delta\Omega = 5$ GHz. We note that that there is no background subtraction in any of our reported visibilities.

4.4.5 Multiphoton Noise Contribution

We estimate the contribution of multiphoton noise to the background in the reported measurements in 3 (main text). The state of the photon pairs generated via SFWM in microresonators can be described as a two-mode squeezed state, $|\psi\rangle \propto \sqrt{1-|\xi|^2}(|0,0\rangle + \xi|1,1\rangle + \xi^2|2,2\rangle + O(\xi^3))$ [28, 64]. The squeezing parameter can be estimated by a direct two-photon cross correlation measurement (Figure 4.5c). Genuine two-photon coincidences are proportional to $|\xi|^2$ and contributions from multi-photon terms are proportional to $|\xi|^4$. The coincidences to accidentals ratio (CAR) is then proportional to $1/|\xi|^2$. After the FBS, the contribution of multi-photon noise can be calculated by including higher order terms in the input state to evaluate Eq. Equation (4.14). These terms are proportional to $|\xi|^4$. The normalization calculated using temporal windows not synchronized with the BS-FWM pumps (red curves, 3 main text) is proportional to $|\xi|^2$. Multiphoton noise contribution then limits the measured interference visibility by $|\xi|^4/|\xi|^2 \approx 1/\mathrm{CAR}$. From the measured CAR of 60 (Figure 4.5c) we estimate this contribution to be approximately 1.6%. Further deviation from unit visibilities is caused due to fluctuations in polarization and pump power during the hour-long measurement.

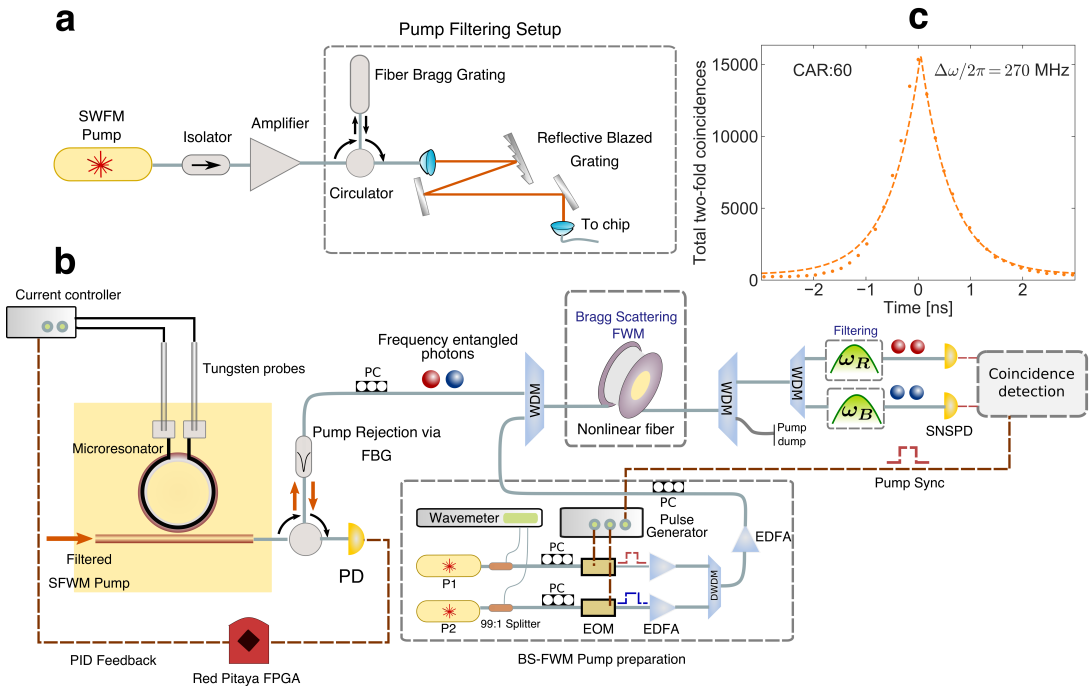

Figure 4.5: **Experimental Setup**. PC: polarization control, EDFA: erbium-doped fiber amplifier, WDM: wavelength-division multiplexer, PD: photodiode, FBG: fiber bragg grating,EOM: electro-optic modulator, SNSPD: superconducting nanowire single-photon detectors. a) **Preparation of the SFWM pump**: An external cavity diode laser at 1282.8 nm together with a fiber amplifier is used as the SFWM pump. A combination of a free-space filtering setup and FBGs is used to reject amplified spontaneous emission noise before coupling the SFWM pump to the chip. b) **Photon-pair generation and BS-FWM**: The SFWM pump is coupled to the TM mode of the bus waveguide. The resonator is maintained at a fixed detuning with respect to the SFWM pump via a feed back control loop on the integrated microheaters. BS-FWM pumps are prepared using EOMs, amplified via EDFAs and combined using WDMs. After the nonlinear process, the pumps and the photons are separated using WDMs followed by free-space grating filters. A three-fold coincidence measurement is performed after photon detection with SNSPDs together with a sync signal from the BS-FWM pumps. c) **Single-photon source characterization**: Measured two-fold coincidences from the single-photon source. We extract a bandwidth of 270 ± 15 MHz from the coincidence measurement and a coincidences to accidentals ratio (CAR) of 60.

4.5 Comparison with EOM-based schemes

4.5.1 Loss performance

Our implementation of BS-FWM setup has a total insertion loss of just 1.3 dB (see also Ref. 11, main text). The total insertion loss of the EOM-pulse-shaper-EOM frequency beam-splitter setup is about 12.5 dB (out of which 2.8 dB is due to each EOM and 4.7 dB is from the pulse shaper, Ref. 36 main text). The low insertion loss of the BS-FWM is particularly advantageous for scaling frequency domain operations to include a large number of modes. In our experiment, the BS-FWM pumps are modulated with 2% duty cycle (2 MHz repetition rate with 10 ns pump duration) in order to achieve a high effective peak power while the photon source is CW-pumped. This induces an effective loss of 17 dB as we post-select photon coincidences on temporal windows synchronized with the 10 ns BS-FWM pump window. However, using pulsed excitation of the microresonator, it is possible to temporally synchronize the photon pair generation and BS-FWM process thereby eliminating the need for post selection. Such a pulsed-pump photon source will have higher brightness due to higher peak power in the resonator. Moreover, with such a synchronized scheme, the BS-FWM pump duration can be significantly reduced to match the coherence time of the single-photons (1 ns in this implementation), allowing for significantly higher repetition rates without the need of additional amplification. It is also possible to create an effectively pulsed excitation of the microresonator by using a self-lasing external actively mode-locked cavity consisting of a gain medium (such as a fiber-based amplifier) together with the microresonator acting as a spectral filter [122].

4.5.2 Bandwidth

Electro-optic modulators have bandwidths up to a few 10s of GHz. The frequency conversion efficiency to the n^{th} order sideband is proportional to $J_n^2(a)$, where J_n is the n^{th} Bessel function and a is proportional to the RF-drive strength. The maximum frequency-conversion efficiency is 34%, 24% and 19% for $n = 1$, 2 and 3 respectively. EOMs can effectively process closely spaced frequency modes generated by spectrally filtering free-space single-photon sources [127, 128]. For modes separated by more than a few 10s of GHz, implementing a *deterministic* two-mode frequency beam splitter interaction where the photons are not lost to spurious sidebands is challenging to achieve using EOMs.

As shown in Supplementary Figure 2.3d, efficient frequency conversion ($\eta > 0.95$) is possible for frequency separations ranging from a few hundred GHz to a few THz via BS-FWM. Our FBS is therefore compatible with the spectral mode spacing of integrated microresonators. This makes it possible to realize two-photon quantum interference in the frequency domain over large frequency separations (800 GHz) as demonstrated in our manuscript. In contrast to bulk sources, photon pairs generated via cavity-enhanced spontaneous four-wave mixing in microresonators are produced in discrete, narrow-frequency modes with high brightness, eliminating the need for strong spectral filtering to create discrete frequency bins. Our work shows that integrated single-photon sources and BS-FWM are complementary tools for realizing selective two-photon quantum operations in the frequency domain.

4.5.3 Multiplexing of frequency-domain operations

The implementation of a deterministic two-photon FBS by combining 2 EOMs and pulse shaping is an attractive scheme demonstrated in Refs. 34 and 36 (main text). In this scheme, multiplexed operations targeting different spectral modes are possible by simply modifying the phase on the pulse shaper due to the fact that spectral mode mixing with EOMs via a single RF-drive $\Delta\nu_{RF}$ induces a global coupling between all frequency modes spaced by $\Delta\nu_{RF}$ ($\Delta\nu_{RF}$ = 25 GHz in Ref. 36). After appropriate pulse shaping, the modes can be recombined via interaction through another EOM, resulting in an effectively two-mode interaction.

In contrast, we operate BS-FWM in a regime where the frequency separation of the two single photons (800 GHz) is much larger than the BS-FWM acceptance bandwidth (δ_{BS} = 150 GHz). If we operate in a regime where the photon separation is smaller than this acceptance bandwidth, multiplexed operations with classical pumps and pulse-shaping similar to the EOM scheme above are possible. However, for multiplexing operations between modes with frequency separations compatible with microresonators, the use of additional BS-FWM pumps is necessary. Scaling our scheme to include more modes will be accompanied by additional classical resource overhead for preparing the appropriate BS-FWM pumps. However, the loss tolerance for classical resources and processing is significantly higher and no additional components/losses are introduced in the path of the single photons [99].

CHAPTER 5

FREQUENCY DOMAIN BOSON SAMPLING

In the previous chapter, we demonstrated quantum interference of two photons of distinct colors. The bunching of two photons in the same arm of a Hong-Ou-Mandel interferometer is the result of interference of the *complex two-photon amplitudes* at the output. This problem can be further generalized by considering a multi-photon interferometer. The problem of correctly predicting the outcome of multi-photon interference in a large linear optical interferometer however is classically intractable. Aaronson and Arkhipov in [129] showed that this problem is equivalent to calculating the permanent of a sub-matrix of the unitary matrix describing the linear optical interferometer and belongs to the #P complexity class. Several related problems such as instantaneous quantum-polynomial sampling (IQP) [130, 131] and random circuit sampling [132, 133] have also been shown to be hard to simulate on classical computers. These problems have gained wide traction due to their potential for demonstrating "quantum supremacy". A successful demonstration of such quantum supremacy would refute the extended Church-Turing thesis, which states that any "effectively computable function" can be efficiently calculated on a Turing machine [134]. Google's recent experiment implemented on a superconducting microwave circuit claiming such supremacy relied on the computational hardness of a variant of random circuit sampling. In addition, quantum sampling problems such as boson sampling may have applications in quantum cryptography, where the unitary matrix describing the linear photonic interferometer acts as a shared secret and two parties can communicate via a noisy channel using a multi-photon state encrypting the message [135, 136].

Several experimental implementations of boson sampling have been realized to date [94, 137, 138]. These experiments use miniaturized integrated circuits to implement

the linear optical interferometers. The state-of-the-art demonstration of boson sampling utilizes 20 photons at the input of a 60 mode interferometer [139].

Here, we propose an alternative implementation in the frequency domain. A crucial advantage of this implementation is that the BS-FWM pumps can easily couple non-nearest neighbor modes, so that the complexity of the four-wave mixing interaction is decoupled from the number of pumps involved. We show that we can generate arbitrary, Haar random target $N \times N$ unitary matrices using a cascaded scheme using N^2 BS-FWM pumps. The eigenvalues and eigenvectors of the generated matrices are uniformly distributed, resulting in matrices that are uniformly drawn from the Haar measure. The amplitude and phase of the pumps can be easily tuned using commercial 4f-shapers to realize arbitrary, reconfigurable unitary interactions in the frequency domain.

5.1 Generalized coupled mode equations for BS-FWM

Consider N single-photon level fields interacting via N BS-FWM pump fields. We assume as before that each pair of signal (single-photon) field and pump field are placed symmetrically with respect to the zero dispersion point of the interaction medium. We also assume that the dispersion is strong enough that asymmetrically placed pairs of pump fields do not couple a given pair of signal fields. The coupled mode equations in this case are given as,

$$\begin{aligned} \frac{\partial A_P^n}{\partial z} &= i\gamma \left(|A_P^n|^2 + 2 \sum_{m \neq n} |A_P^m|^2 \right) A_P^n \\ \frac{\partial A_S^n}{\partial z} &= i\gamma \left(2 \sum_{m} |A_P^m|^2 \right) A_S^n + 2i\gamma \sum_{n \neq m} A_P^n A_P^m A_S^m \exp i\Delta k_L z \end{aligned} \tag{5.1}$$

The explicit z-dependence in the coupling term for the signal fields in Equation (5.1) can be eliminated via the transformations,

$$A_P^n = C_P^n \exp\left[i\left(\gamma|A_P^n|^2 + 2\gamma\sum_{m\neq n}|A_P^m|^2\right)\right] \tag{5.2}$$

$$A_S^n = C_S^n \exp\left[i\left(\beta_P^n - \gamma|A_P^n|^2\right)\right] \tag{5.3}$$

The coupled mode equations for the signal fields now take the z-independent form,

$$\frac{dC_s^n}{dz} = i(\beta_s^n + \beta_p^n - \gamma|C_p^n|^2)C_s^n + i2\gamma\sum_{k\neq n} C_p^k C_p^{n*} C_s^k \tag{5.4}$$

Notice that in Equation (5.4), the first terms represent diagonal matrices representing the relevant propagation constant and nonlinear phase for each of the signal fields and the second term represents the coupling term between the various fields. This second term is a skew-Hermitian matrix. We now make the crucial observation that the coupling matrix represented by Equation (5.4), can be written in the form,

$$H = 2i\gamma \boldsymbol{C}_P C_P^\dagger \tag{5.5}$$

Where $\boldsymbol{C}_P$ is a column vector containing the complex pump amplitudes. It is clear that the right hand side of Equation (5.5) is a rank-1 matrix. We will use this fact in the next section to decompose an arbitrary Haar-random unitary matrix in terms of a cascaded BS-FWM interaction.

5.2 Arbitrary target unitary transformations via BS-FWM

The hardness proof for boson sampling from a complexity theory point of view assumes that the unitary matrix is uniformly distributed according to the Haar measure. This is equivalent to drawing a random $N \times N$ unitary matrix uniformly from the subspace of *all* $N \times N$ unitary matrices. Naturally, the eigenvalues and eigenvectors of these matrices will demonstrate statistical properties corresponding to these measures. Here, we focus

on showing that we can generate an arbitrary target Haar random unitary matrix (U_t) via BS-FWM. Every unitary matrix is diagonalizable due to the spectral theorem and the logarithm of the unitary matrix can be calculated after diagonalization. Let H_t be the resulting skew-Hermitian matrix such that $\exp H_t = U_t$. The entries of a skew-Hermitian matrix are purely complex. Now, the skew-Hermitian matrix H_t has rank N as all rows and columns of the unitary matrix U_t are orthogonal. Once again, using the spectral theorem, we can write,

$$H_t = \sum_{i \in N} \lambda_i v_i v_i^\dagger \tag{5.6}$$

where λ_i are the complex eigenvalues of H_t and v_i are the corresponding eigenvectors. Comparing equations Equation (5.5) and Equation (5.6), we can now clearly see that by cascading N BS-FWM processes each driven by N pumps, we can generate an arbitrary target unitary evolution U_t. While we need a total of N phase-amplitude settings for each pump, this can be performed in a loop where the same set of BS-FWM pumps are reset and the single-photon fields are looped back into the input of the BS-FWM medium.

Figure 5.1 shows such an interaction as a function of the interaction length. The amplitudes and phases of the pumps were calculated such that the target unitary matrix U_t is achieved for $L = 1$.

This calculation opens up several possibilities for our BS-FWM setup. In particular, we can implement special matrices such as the quantum fourier transform matrix. The action of such a matrix on frequency qudits and the resulting interference patterns would be an interesting direction to explore. Finally, for applications such as boson sampling, a *particular* target matrix is not required. The number of loops required for these applications can then potentially be less than N.

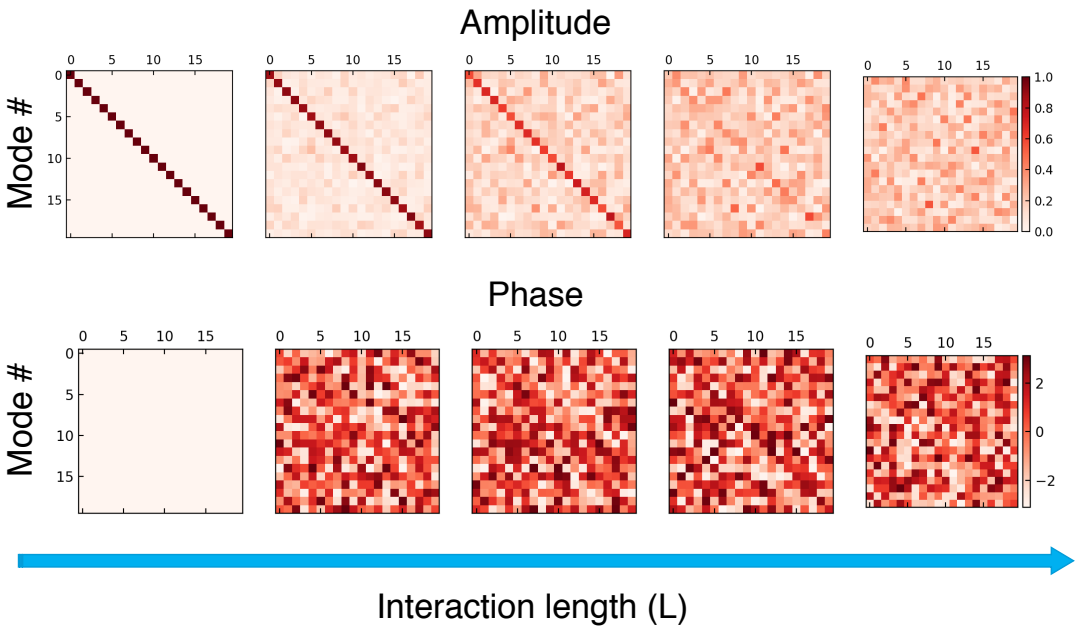

Figure 5.1: **Amplitude and Phase evolution:** Calculated amplitude and phase of the elements of the unitary matrix describing the interaction of 20 frequency modes via BS-FWM. For sufficiently large average interactions strength, the coupling between the various frequency modes is highly delocalized. The phase of the individual elements is randomly distributed, as expected from a Haar random unitary matrix.

CHAPTER 6

PICOSECOND-RESOLUTION SINGLE-PHOTON TIME LENS FOR TEMPORAL MODE QUANTUM PROCESSING

In previous chapters, we demonstrated applications of BS-FWM to processing of narrowband, discrete frequency modes of single photons. However for applications that require active synchronization in the time-domain, it is necessary to use single photons in well defined temporal modes. Field-orthogonal, frequency-broadband temporal modes of light have recently been shown to be a complete framework for photonic QIP [140]. 1D Hermite-Gaussian (HG) modes and their linear superpositions form a complete, mutually unbiased basis set for such temporal mode processing. By combining classical techniques such as 4f pulse shaping and sum frequency generation (SFG), a complete set of operations including generation of single-photons, coherent manipulation and tomography of temporal HG modes have been demonstrated [140–145].

In this work, we propose an alternative route for processing single-photon waveforms on the picosecond and sub-picosecond time scales. Drawing on space-time duality, temporal imaging systems (”time lens”) have been used for the generation, manipulation and direct characterization of complex, ultrafast classical pulses with bandwidths > 1 THz [146]. By directly harnessing nonlinear optical processes such as four-wave mixing, these techniques overcome the limited bandwidth of electronic signal processing and photo-detection systems and have led to the creation of a new toolkit for high-bandwidth all-optical signal processing. Here, we propose to extend these well-developed tools for temporal processing of ultrafast single photon waveforms. In the spatial domain, elegant tools from Fourier optics have been used for high-dimensional quantum key distribution (QKD) and cryptography using the orbital angular momentum eigenstates (OAM) of light. OAM eigenstates and corresponding set of complete multually unbiased states

have been generated using computer generated holograms, spiral phase plates, spatial light modulators and digital micro mirror devices. An arbitrary set of OAM modes can be efficiently sorted by performing a log-polar coordinate transformation using just two phase plate and a Fourier transform lens. In this chapter, we show that techniques from Fourier optics such as coordinate transformations can be generalized to the time domain to create a powerful toolkit for arbitrary processing of temporal modes of single-photons.

In the first part of this chapter, we will demonstrate a time-lines based on coherent and noise-free manipulation of single-photon level pulses using BS-FWM. We demonstrate a magnification factor of 158 along with discrimination of pulses of 2.2 ps width. Next, we propose a temporal mode sorter that acts as an efficient demultiplexer for 1D Hermite-Gaussian modes. This can be achieved by imparting a complex but smooth phase pattern on the BS-FWM. Using numerical optimization techniques (steepest gradient descent), we demonstrate that 12 temporal modes can be sorted using just 4 cascaded "time lens" stages.

6.1 Single-photon time lens using Bragg Scattering Four-Wave Mixing

In Chapter 1, we developed the theory for BS-FWM using coupled mode equations for 4 interacting fields in the cw-limit i.e. assuming each of the 4 interacting fields is narrow in frequency. Here, we show that broadband phase matching conditions can be engineered in order to use BS-FWM with pulsed single-photon level inputs. As shown in Figure 6.1, we consider the case where two of the symmetrically placed fields (ω_{P1}, ω_R) are chirped pulses, and the other pump (ω_{P2}) is cw. Below, we derive conditions under which the broadband input centered at ω_R is converted to a narrow field centered at ω_B.

This corresponds to spectral compression (temporal magnification) of the input pulse. We assume that the pulsed fields centered at $\omega_{P1}^0, \omega_R^0$ are imparted a group delay dispersion (GDD, $\beta^2 L$) of (Φ_{P1}, Φ_{P2}) respectively. The GDD introduces a phase $\exp\left(\frac{i\tau^2}{2\Phi}\right)$ [147]. In the limit of large linear chirp on the two pulsed fields ($\Phi^2\delta\omega^4 \gg 1$), we can calculate the derivative of the phase $\omega^0\tau + \tau^2/2\Phi$ and write the instantaneous frequency of each of the pulses to be,

$$\omega_{P1}(\tau) = \omega_{P1}^0 + \frac{\tau}{\Phi_{P1}} \tag{6.1}$$

$$\omega_R(\tau) = \omega_{P1}^0 + \frac{\tau}{\Phi_R} \tag{6.2}$$

We can now calculate the instantaneous phase mismatch using an expression similar to Equation (2.32),

$$\Delta k(\tau) = -\frac{\beta^{(3)}}{2\Phi_R^2\Phi_B^2}\tau(\tau + \Omega\Phi_{P1})(\Phi_{P1} + \Phi_R)(\tau + 2\omega\Phi_R) + O(\beta^{(4)}) \tag{6.3}$$

From the above equation, it is clear that broadband phase matching is possible when the two pulsed fields have equal and opposite chirps ($\Phi_R = -\Phi_{P1}$). The higher order dispersion terms ultimately limit the acceptance bandwidth and temporal aperture of lens. Figure 6.2 shows the calculated conversion efficiency when these conditions are satisfied. These calculations show that the BS-FWM acceptance bandwidth (δ_{BS}) for pulsed inputs exceeds 5 nm. The corresponds to sub-picosecond temporal resolution with our implementation of BS-FWM in a dispersion shifted fiber.

6.2 Temporal magnification and picosecond pulse discrimination

In this section, we summarize experimental results for temporal magnification using a BS-FWM time lens. Our scheme for temporal magnification is shown in Fig. We generate an ultrashort signal pulse that is synchronized with the BS-FWM pulsed pump

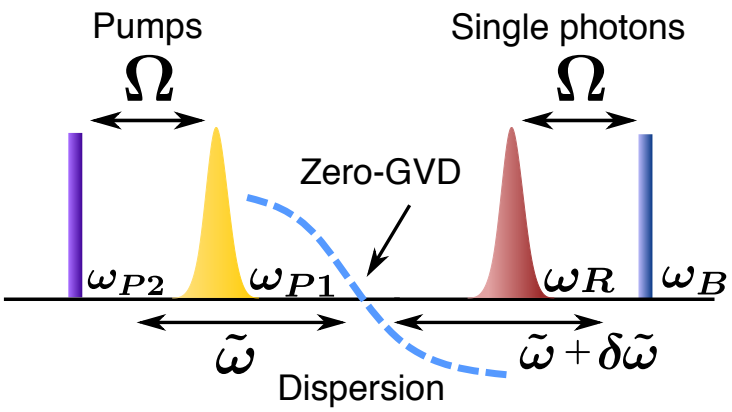

Figure 6.1: **BS-FWM with pulsed inputs:** To implement a time lens via BS-FWM, we use two chirped pulsed inputs (ω_{P1}, ω_R) and the other pump field is assumed to be narrow in frequency. If the chirps applied to the two pulsed fields are equal in magnitude and opposite in sign ($\Phi_{P1} = -\Phi_R$), the broadband input field centered at ω_R gets converted to a narrow input field centered at ω_B.

as shown in Fig. 6.3. We use a pulsed laser (center wavelength 1560 nm, 80 fs nominal pulse width, 70 mW average power, 80 MHz repetition rate) to seed the generation of broadband supercontinuum in a highly nonlinear fiber (HNLF). We find that the seed power launched into the HNLF is the most important factor determining the extent of the spectral broadening of the laser and increasing the length of the HNLF does not significantly improve the spectral broadening. We modified the splicing parameters on the Fujikura Fusion Splicer in order to fuse one end of the HNLF with an SMF, and find that a higher arc power and arc current as compared to SMF splicing parameters resulted in lower splicing loss. This reduced splicing loss was a critical factor in achieving the required broadband supercontinuum in Fig. 6.3.

We extract a narrowband signal centered at 1285 nm using a monochromator (3dB bandwidth 5 nm). The probe is sent through 4 km OFS Truewave fiber to impart a group delay dispersion $\Phi_s = 7.6ps^2$ to the input signal. The remaining power from the pulsed laser is sent to a Finisar waveshaper for amplitude and phase filtering. We apply a flat top amplitude filter centered at 1550 nm with a quadratic phase (group delay

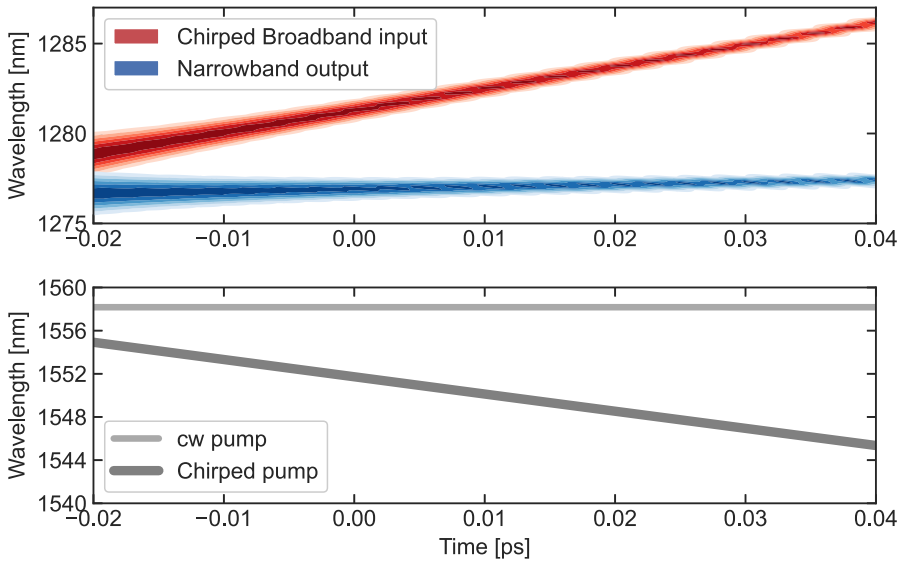

Figure 6.2: **Broadband phase matching with BS-FWM:**Calculated conversion efficiency with one pump as a chirped broadband pulse and the other pump as a cw field. Optimal phase matching is observed for broadband input pulse (red) with a chirp equal in magnitude but opposite in sign to that of the pump. The broadband input is converted to the narrow, unchirped output shown in blue. The acceptance bandwidth of this process exceeds 5 nm ($\delta_{BS} > 5$ nm) corresponding to sub-picosecond temporal resolution ($1/\delta_{BS} < 1$ ps)

dispersion $\Phi_p = -7.6ps^2$) to the pump so that the condition $\Phi_p = -\Phi_s$ is satisfied. The signal is passed through a free space delay line comprised of a 60 cm dovetail rail fitted with a corner cube and an additional tunable delay line for fine delay control. The tunable delay line is controlled by a Kinesis servo motor controller. The signal is then combined with the chirped pump and sent to the BS-FWM fiber. A small band of the rejected supercontinuum is monitored on a fast photodiode (EOT 3500 F). The photodiode signal is amplified with a high bandwidth 3-stage RF amplifier (Centellax) and then downsampled to 4 MHz using a field-programmable gate array (FPGA). The downsampled signal is used as a trigger to carve out 10 ns pulses from a CW laser at 1558 nm using electro-optic modulators which acts as the second pump in the BS-FWM process. For efficient four-wave mixing, the pulsed pump and the input signal must be

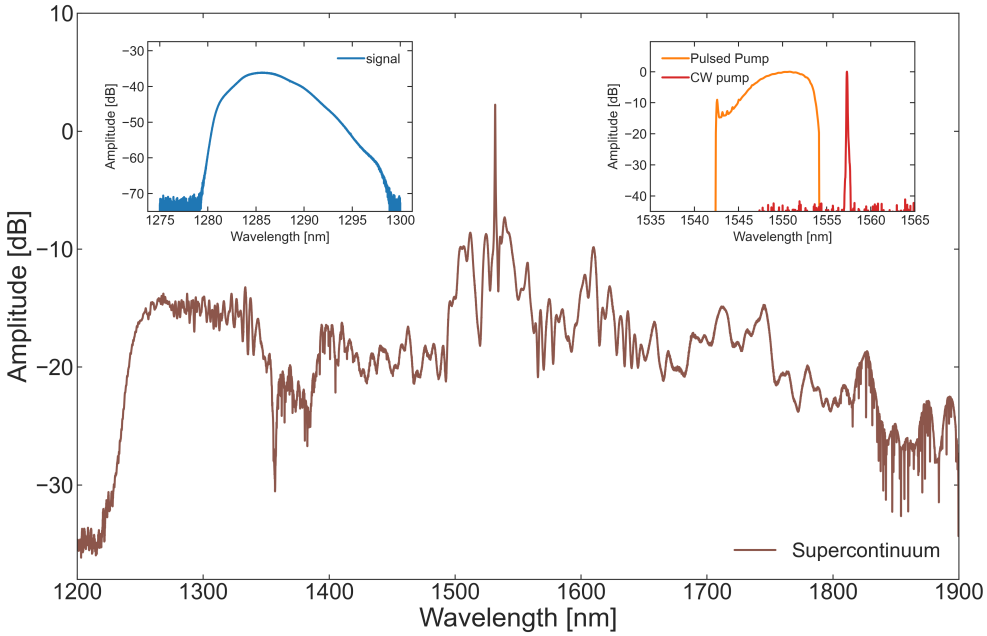

Figure 6.3: **Generation of temporally synchronized signal pulse:** A pulsed laser (80 fs nominal pulse width) is used to seed the generation of broad supercontinuum from 1250 to 1800 nm. Using a monochromator, a part of this generated supercontinuum with 5 nm 3dB bandwidth is extracted as the signal (see inset 1). The pulsed and cw BS-FWM pumps are shown in inset 2.

precisely overlapped in time. We observe the delay between the two pulses after the BS-FWM fiber and adjust the signal delay line to achieve a crude overlap of the two pulses. We then scan the Thorlabs tunable delay line in steps of 0.1 mm to get maximum four-wave mixing conversion efficiency. The signal is then passed through an 80 km DCM (measured GDD Φ_M = 1300 ps/nm @1300 nm). A copy of the downsampled signal is used as a start trigger to the time-tagging module and the converted idler pulses are detected using superconducting nanowire single photon detectors.

In order to measure the magnification factor of our system, we scan the relative delay between the signal and the pulsed BS-FWM pump (tunable delay line step size of 0.2 mm) and observe the magnified delay on the SNSPDs. This is analogous moving an object away from the optical axis of a spatial lens. Fig. 6.4 shows our results from this measurement. The gradient of the shifted peaks are calculated to accurately calibrate

the magnified delay with respect to the actual stage delay. We measure a magnification factor of 158, as shown in Fig. 6.5. This value comes close to the expected theoretical magnification factor $M = \left|\frac{\Phi_M}{\Phi_s}\right| = 171$.

Finally, we demonstrate pulse discrimination of two single-photon level pulses at the picosecond time scale. We use a polarization maintaining fiber that introduces as a delay between the fast and the slow axis to create two signal pulses. The two pulses are magnified with our temporal lens system and observed directly on the SNSPDs, as shown in Fig. 6.5. From the measured magnified pulsed width (FWHM 350 ps) and the calibrated magnification factor ($M = 158$), we infer that the input pulse width is at most 2.2 picoseconds. The two pulses, initially separated by 2.5 ps and unresolvable by direct detection can now be discriminated with the time lens. The measured resolution of our temporal lens system is limited by the combined electronic jitter of our measurement system. We estimate the combined jitter of the SNSPDs, the time tagging module and the trigger signal from the FPGA to be 240 ps (see fig.). In the next section, we perform theoretical calculations and simulations to show that the optical performance of the system is capable to resolving sub-picosecond pulses.

6.3 Timing jitter analysis

The measured resolution of our time lens is primarily limited by electronic jitter of the trigger signal from the FPGA acting as the ”start” channel in all our measurements with the time tagging module. In this section, we provide detailed measurements to extract the electronic jitter of our measurement system. In order to characterize the intrinsic jitter of the time tagging module, we measure the autocorrelation of a fast electronic signal. The FWHM of the measure autocorrelation signal is $\tau_{ttm} = 76$ ps. This FWHM is

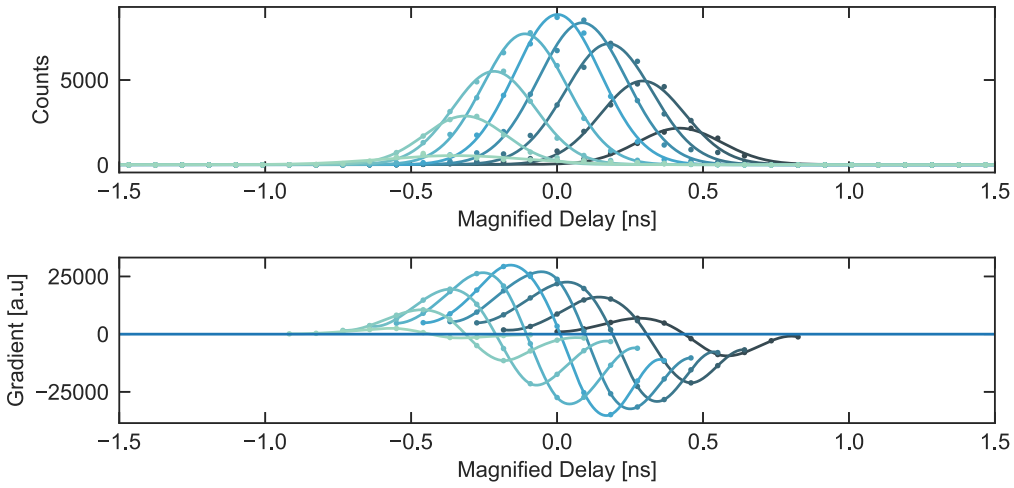

Figure 6.4: **Magnification of temporal delay:** The delay of the input signal is scanned relative to the pulsed BS-FWM pump and the magnified delay is observed directly on the single-photon detectors. The gradient of the shifted peaks are calculated to accurately calibrate the magnified delay with respect to the actual stage delay.

related to the single channel jitter J_{ttm} as $2J_{\text{ttm}}^2 = \tau_{\text{ttm}}^2$ ps, resulting in $J_{\text{ttm}} = 54$ ps. Next, we send the pulsed laser (200 fs pulse width) directly to the SNSPDs and measure the cross-correlation of the trigger signal with this optical signal using the TTM (see). The measured FWHM for this cross-correlation signal is $\tau_{ttm,snspd} = 260$ ps. We can write the combined jitter for this measurement as,

$$J_{\text{pulse}}^2 + J_{\text{snspd}}^2 + J_{\text{trig}}^2 + 2J_{\text{ttm}}^2 = \tau_{\text{ttm,snspd}}^2 \tag{6.4}$$

The J_{pulse} is negligible as we are using a fs-pulsed laser as the optical input. The nominal jitter of out SNSPDs is $J_{\text{snspd}} = 70$ ps, and using the measured jitter of the TTM module (54 ps), we can extract the jitter of the trigger signal from Equation (6.4) $J_{trig} = 240$ ps. This trigger signal jitter is the result of the combined timing jitter of the photodiode, RF amplifier and the FPGA latency. State-of-the-art time tagging modules have an electronic jitter of ¡5 ps. The electronic jitter of our measurement system can be significantly reduced by using a faster downsampling circuit.

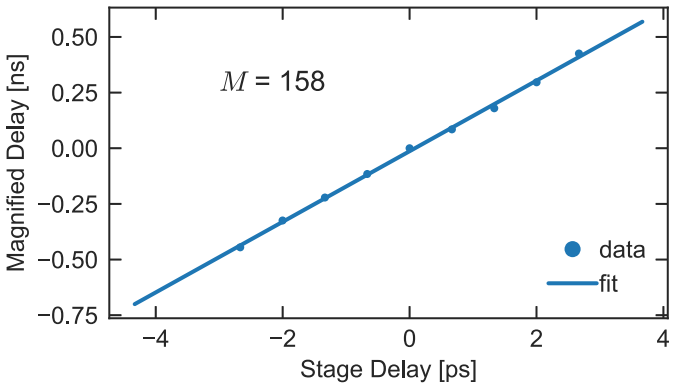

Figure 6.5: **Magnification factor:** Calibration of the measured magnified delay relative to the actual stage delay results in a measured magnification factor of 158 for our temporal imaging system.

Having isolated the effects of electronic jitter, we can now directly determine the optical resolution ($J_{\text{snspd}}, J_{\text{pulse}}$) of our measurement system. For the measurement shown in Figure 6.6, the total jitter is,

$$J_{\text{opt}}^2 + J_{\text{elec}}^2 = 350^2 \tag{6.5}$$

$$J_{\text{elec}}^2 = J_{\text{trig}}^2 + 2J_{\text{ttm}}^2 \tag{6.6}$$

In Equation (6.6), we include contributions from the SNSPD jitter to the ”optical” jitter. From Equation (6.6), we extract the total optical jitter to be $\tau_{\text{opt}} = 244$ ps. From this, we extract the measured optical resolution of our system to be $\tau_{\text{opt}}/M = 1.5ps$. This optical jitter is the result of spectral filtering of the supercontinuum to generate the probe pulse, and possible residual chirp arising from the filtering setup. In the next section, we show that the optical resolution of the BS-FWM time lens is predominantly determined by the acceptance bandwidth of the BS-FWM process and can reach sub-picosecond thresholds.

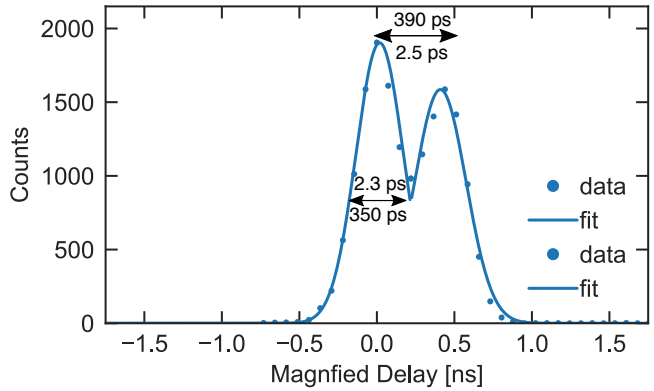

Figure 6.6: **Pulse discrimination with picosecond resolution:** The input signal is sent through a polarization maintaining fiber to create two pulses with a small relative delay. The two pulses are magnified and directly discriminated on the superconducting nanowire single photon detectors. Based on the measured magnified pulse width and the calibrated magnification factor of the time lens, the input pulse width is estimated to be at most 2.2 ps. The two pulses, initially separated by 2.5 ps and unresolvable by direct detection can now be discriminated with the time lens

6.4 Temporal mode sorting with a time lens

Field-orthogonal temporal modes have intensity overlapping spectra and temporal shapes in the frequency and time domain respectively. This makes it challenging to efficiently sort temporal modes by direction observation of the spectra. Temporal mode sorting has been theoretically analyzed and experimentally demonstrated using temporal mode selective frequency conversion [141, 148]. The efficiency of single-stage mode selective frequency conversion is however limited to about 0.8 as phase-matching is only satisfied for the central frequencies of the interacting pulsed fields [141, 148]. By using a two-stage Ramsey interferometer, the conversion efficiency can be improved to unity, resulting in a deterministic temporal mode selective device [143, 149]. However, in order to realize an arbitrary temporal mode demultiplexer using this scheme, several shaped pump pulses must be included simultaneously in the nonlinear interaction. Here, we propose an alternative method for temporal mode sorting and demultiplexing using the

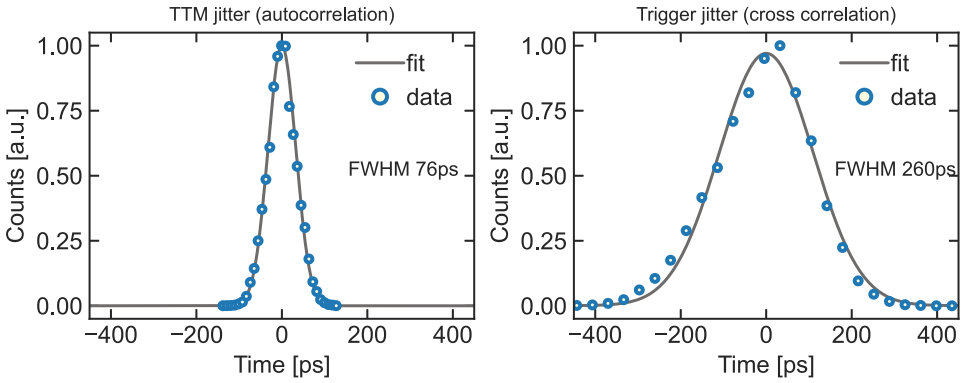

Figure 6.7: **Characterization of jitter**: a) Measured TTM jitter via autocorrelation using a fast electronic signal. b) Measured trigger jitter via cross correlation of trigger signal with an ultrashort optical pulse incident on the SNSPDs. These measurements are used to isolate the effects of electronic and optical jitter in our measurement system.

time lens paradigm. The time lens described before for temporal magnification imparts only a quadratic phase shift $\phi(t) = \frac{t^2}{2D_f}$ in time on the input temporal waveform, and this lens performs a Fourier transform just as in the spatial case. A significantly richer and complex set of operations is possible by using an arbitrary waveform $\phi(t)$ and a generalized dispersion function $G(\omega)$ [150].

It was recently shown in [151] that 210 orthogonal spatially co-located 2D HG modes can efficiently sorted into distinct Gaussian spots on a cartesian grid using a 7-stage multi-plane light converter. We adapt this concept to 1D HG modes in the time domain to realize efficient sorting of orthogonal temporal modes. Our scheme is shown in Figure 6.8. The input ψ_N^0 is the set $HG_0, HG_1, HG_2 ... HG_n$ of orthogonal 1D HG modes. The target output are a series of temporally separated Gaussian pulses (see Fig. 6.8a). We define the loss function,

$$e = 1 - \frac{1}{S}\frac{1}{N}\sum_{i\in 1..S}\sum_{k\in 1...N} |\langle \psi_{i,b}^k | \psi_{i,f}^k \rangle|^2 \tag{6.7}$$

where (f, b) denote the forward and backward propagated waveforms respectively, N

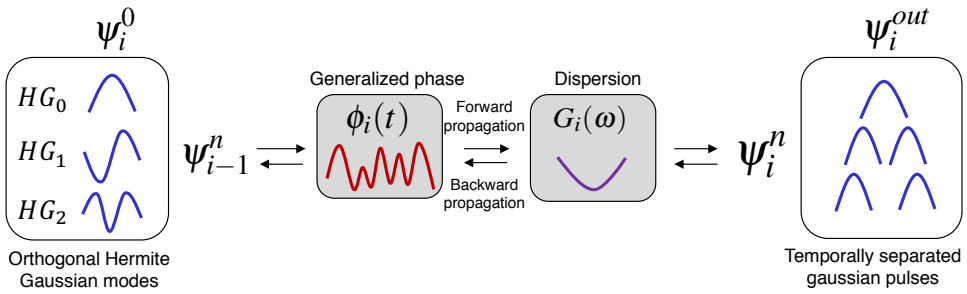

Figure 6.8: **Temporal mode sorting with a time lens**: Complex, arbitrary unitary transformations on input temporal waveforms ψ are possible by cascading several phase-only time ($\phi(t)$) and frequency ($G(\omega)$) operations as shown above. For temporal mode sorting, we set $\phi(t)$ to be an arbitrary time-domain waveform and restrict $G(\omega)$ to second-order dispersion. The input waveforms ψ^n are an orthonormal basis set of n Hermite-Gaussian (HG) modes. The target waveforms are temporally separated Gaussian pulses. The parameters of ϕ and G are numerically optimized using steepest gradient descent to obtain maximum overlap for both forward and backward propagated waveforms ψ_i at each stage i.

denotes the number of input HG modes and S is the total number of optimization stages. The loss function in Eq. 6.7 captures the waveform mismatch for forward and backward propagation at each stage. While Ref. [151] calculates the updated phase by strictly enforcing wavefront matching at each optimization step, here we use steepest gradient descent (GD) to calculate the parameters determining $\phi(t)$ and $G(\omega)$. We restrict $G(\omega)$ to small second order dispersion terms, $G(\omega)$ therefore acts as a phase-only frequency filter. We use a piecewise-constant ansatz for the phase function $\phi(t)$. In order to contain the magnitude of the functions ϕ and G during the optimization process, we use regularization terms proportional to the the magnitude of the coefficients in *phi* and G. These regularization terms are added to the loss function in Eq. Equation (6.7). We implement the GD descent algorithm using PyTorch, which allows for fast computation of gradients of the loss function with respect to a large number of optimization parameters. Our optimization converges quickly after about 1000 iterations. Our results are shown in Fig. 6.10. We use 4 cascaded stages of time and frequency phase-only manipulations for sorting 10 orthogonal 1D HG modes. The optimized phases determined by GD are

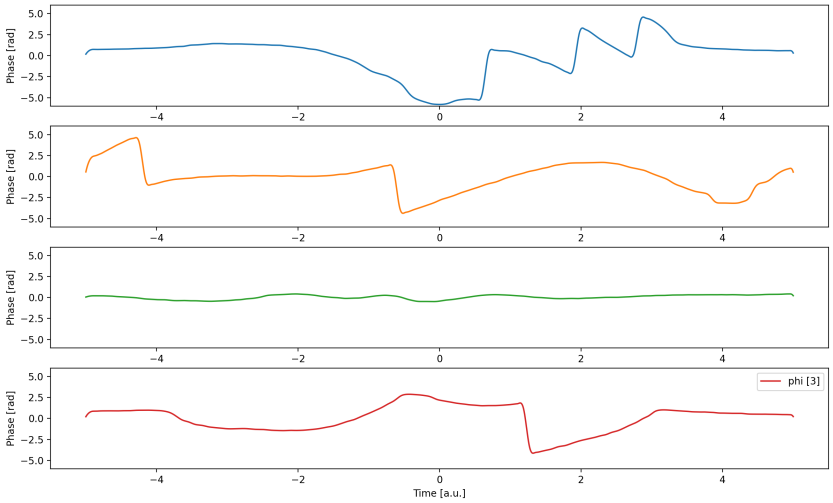

Figure 6.9: **Optimized phase function** $\phi_i(t)$ for each of the four cascaded stages for sorting 10 orthogonal HG modes.

shown in Fig. Figure 6.9. We measure a combined overlap of 92% with the target modes. The temporally separated Gaussian modes can then be temporally magnified and directly observed using single-photon detectors for efficient sorting/demultiplexing.

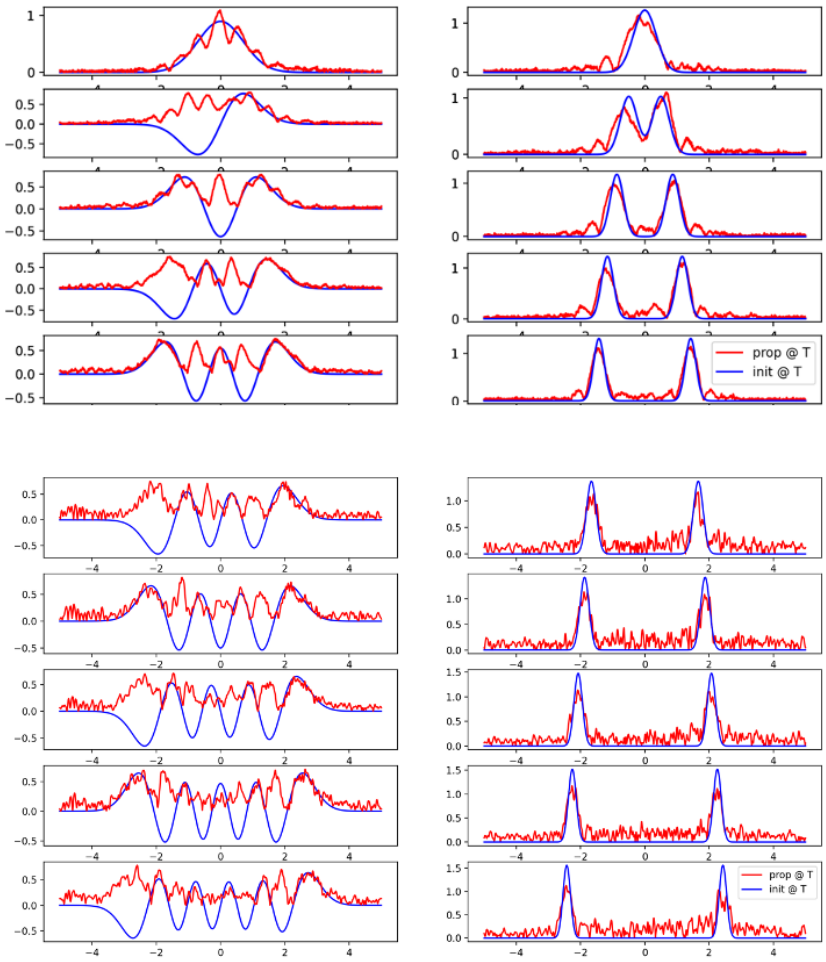

Figure 6.10: **Temporal mode sorting results:** Sorting of 10 orthogonal 1D HG modes (left) to temporally separated Gaussians (right) using 4 cascaded stages of time and frequency phase manipulations. The blue curves denote the initial (left) and the target (right) modes respectively. The red curves denote the backward (left) an forward propagated modes from the target and initial modes respectively. We measure a combined overlap of 92% with the target modes. The Gaussian pulses on the right can be temporally magnified and directly observed on single-photon detectors for efficient sorting/demultiplexing.

CHAPTER 7

PERSPECTIVES AND FUTURE DIRECTIONS

The results presented in this thesis demonstrate that BS-FWM is a powerful, reliable and repeatable tool for the coherent manipulation of quantum states of light in the frequency and time domain. The applications described here exploit the flexibility that this platform provides and open up several new directions and avenues for the future. Some of them are discussed below.

7.1 Deterministic frequency multiplexed source of single photons

Chapter 3, we demonstrated low loss (1.3 dB) frequency switching with BS-FWM. The major limitation in the demonstrated heralding probability (4.6%) was the heralding efficiency of the SPDC source used in our experiment. Starting with an optimized SPDC source, the overall heralding efficiency of the multiplexed source can be significantly improved. This can be achieved by careful spatial mode matching and the use of efficient single-photon detectors. State-of-the-art commercial SNSPDs now have system detection efficiencies close to 93% at telecom wavelengths. By improving the dielectric stack for complete absorption of the photons, detection efficiencies as high as 98% have recently been demonstrated. Several pioneering demonstrations of the loophole-free test of Bell's theorem relied on stringent requirements of source efficiency. SPDC sources in [24, 152, 153] have raw heralding efficiencies as high as 83%. These demonstrations relied on bulk periodically poled KTP crystals with optimized free space mode matching and fiber coupling. Recent efforts towards integration of SPDC sources have also been successful, achieving close to 50% heralding efficiency with a PPLN waveguide-based, fiber-pigtailed "plug-and-play" source demonstrated in [25].

As shown in Figure 3.5, the performance of multiplexed sources is significantly improved by using PNR detectors for heralding. PNR detectors based on superconducting transition edge sensors (TES) however have a long reset time of several μs, severely constraining the speed of operation of these detectors. For the particular application of single-photon multiplexing however, we only need to be able to distinguish between single-photon ($N = 1$) and multi-photon ($N > 1$) events, and do not need strict photon number resolution capability. A promising new direction for PNR detection technology is to modify the readout circuitry such that the detector becomes sensitive to the number of hotspots on the detection nanowire [58]. In [58], single photon resolution up to 4 photons with a timing jitter of 160 ps was demonstrated. The Photon Spot cryostat in the Gaeta lab can easily house 5 additional nanowires. The fact that the heralding photons have distinct frequencies can be used to detect the photons in a time multiplexed fashion after passing through low-loss dispersion modules, significantly reducing the resources required for implementing a multiplexed single-photon source. A multiplexed single-photon source using PNR heralding has yet to be demonstrated and the new developments in detection technology can create significant breakthroughs in the implementation of multiplexed single-photon sources.

A high efficiency, high repetition rate frequency multiplexed source that combines the above two elements can be implemented at telecom wavelengths with about 20 multiplexed frequency modes and can enable revolutionary new applications in photonic quantum information processing that are not currently possible with existing probabilistic sources.

7.2 On-chip, unidirectional BS-FWM using higher-order waveguide modes

Our implementation of BS-FWM in dispersion shifted fiber can achieve close to 97% efficiency due to suppression of all spurious competing processes in the fiber [2, 154]. Two-mode operation was achieved by ensuring that only a single sideband is efficiently phase matched for a given input frequency ω_{in}, and a given pump separation Ω. A major roadblock to extending this to chip-based waveguides and resonator devices is that the short interaction length is insufficient to create sufficient phase mismatch for the undesired side band [123–125, 155, 156]. This also leads to cascaded processes that further degrade the conversion efficiency of the system. Several solutions to this have been proposed, including creating polarization mode dispersion with highly assymmetric cross sections [157].

We propose an alternative implementation using higher order spatial modes of Si_3N_4 waveguides. Distinct modes families of these orthogonal transverse modes have significantly different effective propagation constants [23, 158]. This fact can be exploited to create strong phase mismatch for the undesired sideband. Efficient couplers for such higher order modes can be designed by matching the effective index of the two waveguides. Preliminary calculations show that such a process is still tunable over a wide range of pump and input/target wavelengths and can in principle achieve unity conversion efficiency with devices few cms in length. This requires a use of short few 100 ps pump pulses in order to avoid damage to the Si_3N_4 waveguides.

7.3 On-chip generation of frequency-polarization entangled Bell states

It is straightforward to directly generate polarization-entangled Bell states using SPDC in $\chi^{(2)}$ crystals and type-II phase matching. However, an on-chip source that directly generated polarization entangled photon pairs has yet to be demonstrated. Previous demonstrations relied on converting path entanglement to polarization entanglement [159]. We propose an alternative, simpler implementation with Si_3N_4 ring resonators. The idea is to generate entanglement by path identity [160]. Two uncoupled ring resonators are coupled to the same bus waveguide. The waveguide cross section of the two rings is designed such that the FSR of the TE fundamental mode family of one ring is matched to the FSR of the TM mode family of the other ring. Using a SFWM that is diagonally polarized, we can now directly generate polarization entangled photon pairs using this simple design. We note that for this scheme to be successful, the FSR of the microresonators for the TM and TE modes respectively has to match to a precision much smaller than the linewidth of the resonator. In addition to complete polarization mode tomography, characterizing this state requires precise measurements which can be performed with the same phase modulation technique used in Chapter 4. The theoretical calculations of the dispersion for Si_3N_4 devices are now very accurate, and certainly allow for the design of this device.

7.4 On-chip generation of GHZ and cluster states

Massive, multipartite entangled states of single photons known as cluster ”states” are universal resources for implementing quantum networks and computers [5, 161]. Recent proposals for all-photonic quantum repeaters replace matter-based quantum memories

with these entangled states at the repeater stations [97, 98, 162]. Due to the lack of deterministic photon-photon nonlinearity at optical frequencies, it is challenging to generate such highly entangled states of optical photons. However, large-scale cluster state generation is possible by combining deterministic sources of single photons, linear operations and efficient single-photon detectors [5, 6, 163]. In these protocols, smaller entangled states of 3 photons known as GHZ states [92] are "fused" together via two-photon interference operations ("fusion gates"). If the probability of the "fusion" operations exceeds a certain threshold, long-range entanglement can be generated via successive fusion operations. The resource requirements for generating these states are massive, making integration a crucial requirement.

The first step in this direction is a GHZ-source generator that operates at high generation rates. A GHZ generator takes 6 single photons as input and interferes pairs of photons on 50:50 beam splitters. Using post-selection, the other three photons can be heralded into a GHZ state [5, 6]. Several modifications of this protocol also exist [164]. Another promising approach to generate such GHZ states is to exploit entanglement by path identity [160]. In this scheme, two sources, each generating 3 entangled photons in two orthogonal modes of a single degrees of freedom (in our case, frequency) can be used to generate a GHZ state. Our demonstration in Chapter 4 shows that efficient fusion gates in the frequency domain are possible. Furthermore, optimization algorithms to minimize the number of switching operations required for these protocols can be be used to further improve the loss performance of our frequency multiplexed systems [165].

The GHZ states generators above require 6 photons to be *simulataneously* release at the input. In order to temporally synchronize the release of photons, on-demand storage-release cavities can be used. With Si_3N_4 resonator quality factors approaching 37 million, storage cavities with tens of ns of lifetime can be implemented [166, 167]. The

major challenge is active switching of the resonances on timescales much smaller than the cavity lifetime. This is an active area of research.

7.5 Temporal mode sorting with a time lens

The numerical calculations presented in Section 6.4 show efficient mode sorting of 12 orthogonal temporal modes using time dependent phase $\phi(t)$ and dispersion parameters $G(\omega)$. The parameters $\phi(t), G(\omega)$ have been constrained during numerical optimization to experimentally feasible values. The time dependent phase $\phi(t)$ can be implemented using a spatial light modulator (SLM) and the dispersion $G(\omega)$ can be implemented using a dispersive free space grating, alternating reflections between the grating and the SLM [150, 151]. The final step would be to magnify the separated gaussian modes using our time lens.

7.6 Applications of synthetic dimensions to frequency translation and frequency domain single-photon operations

Synthetic dimensions harness various degrees of higher dimensional freedom (DoF) of a photon (such as frequency and orbital angular momentum) to create a periodic lattice. Much theoretical work related to synthetic dimensions focuses on topological physics and analogies with solid-state systems [168, 169]. However, these concepts can have powerful applications such as unidirectional frequency translation using integrated ring resonators [170–172]. These concepts can be combined with that BS-FWM which can induce efficient non-nearest neighbor coupling to realize novel applications which are

not otherwise possible with electo-optic modulators.

BIBLIOGRAPHY

[1] Boyd, R. W. *Nonlinear Optics* (Academic Press, Burlington, MA, ©2008). 1

[2] Clemmen, S., Farsi, A., Ramelow, S. & Gaeta, A. L. Ramsey Interference with Single Photons. *Physical Review Letters* **117**, 223601 (2016). 2, 69, 70, 72, 79, 88, 117

[3] McGuinness, H. J., Raymer, M. G., McKinstrie, C. J. & Radic, S. Quantum Frequency Translation of Single-Photon States in a Photonic Crystal Fiber. *Physical Review Letters* **105**, 093604 (2010). 2, 7, 70

[4] Li, Y., Humphreys, P. C., Mendoza, G. J. & Benjamin, S. C. Resource Costs for Fault-Tolerant Linear Optical Quantum Computing. *Physical Review X* **5**, 041007 (2015). 2

[5] Browne, D. E. & Rudolph, T. Resource-Efficient Linear Optical Quantum Computation. *Physical Review Letters* **95**, 010501 (2005). 2, 118, 119

[6] Gimeno-Segovia, M., Shadbolt, P., Browne, D. E. & Rudolph, T. From Three-Photon Greenberger-Horne-Zeilinger States to Ballistic Universal Quantum Computation. *Physical Review Letters* **115**, 020502 (2015). 2, 119

[7] Huang, J. & Kumar, P. Observation of quantum frequency conversion. *Physical Review Letters* **68**, 2153–2156 (1992). 7

[8] McKinstrie, C. J., Radic, S. & Raymer, M. G. Quantum noise properties of parametric amplifiers driven by two pump waves. *Optics Express* **12**, 5037–5066 (2004). 8, 70

[9] McKinstrie, C. J., Yu, M., Raymer, M. G. & Radic, S. Quantum noise properties of parametric processes. *Optics Express* **13**, 4986–5012 (2005). 8, 70

[10] Agrawal, G. Chapter 2 - Pulse Propagation in Fibers. In *Nonlinear Fiber Optics (Fifth Edition)*, Optics and Photonics, 27–56 (Academic Press, Boston, 2013). 11

[11] McGuinness, H. J., Raymer, M. G., McKinstrie, C. J. & Radic, S. Quantum Frequency Translation of Single-Photon States in a Photonic Crystal Fiber. *Physical Review Letters* **105**, 093604 (2010). 14

[12] McKinstrie, C. J., Harvey, J. D., Radic, S. & Raymer, M. G. Translation of quantum states by four-wave mixing in fibers. *Optics Express* **13**, 9131–9142 (2005). 18, 70

[13] Farsi, A. Coherent Manipulation Of Light In The Classical And Quantum Regimes Via Four-Wave Mixing Bragg Scattering (2015). 20

[14] Hart, T. R., Aggarwal, R. L. & Lax, B. Temperature Dependence of Raman Scattering in Silicon. *Physical Review B* **1**, 638–642 (1970). 21

[15] Clauser, J. F. & Shimony, A. Bell's theorem. Experimental tests and implications. *Reports on Progress in Physics* **41**, 1881–1927 (1978). 23

[16] Klyshko, D. N. SCATTERING OF LIGHT IN A MEDIUM WITH NONLINEAR POLARIZABILITY 5. 24, 25

[17] Klyshko, D. N. Two-photon (squeezed) light: Classical and quantum effects. *Physics Letters A* **146**, 93–101 (1990). 24

[18] Hong, C. K., Ou, Z. Y. & Mandel, L. Measurement of subpicosecond time intervals between two photons by interference. *Physical Review Letters* **59**, 2044–2046 (1987). 24

[19] Wu, L.-A., Kimble, H. J., Hall, J. L. & Wu, H. Generation of Squeezed States by Parametric Down Conversion. *Physical Review Letters* **57**, 2520–2523 (1986). 24

[20] Kwiat, P. G. *et al.* New High-Intensity Source of Polarization-Entangled Photon Pairs. *Physical Review Letters* **75**, 4337–4341 (1995). 24

[21] Takesue, H. & Inoue, K. Generation of 1.5 - μ m band time-bin entanglement using spontaneous fiber four-wave mixing and planar light-wave circuit interferometers. *Physical Review A* **72** (2005). 24

[22] Ramelow, S., Ratschbacher, L., Fedrizzi, A., Langford, N. K. & Zeilinger, A. Discrete Tunable Color Entanglement. *Physical Review Letters* **103**, 253601 (2009). 24

[23] Mohanty, A. *et al.* Quantum Interference between Transverse Spatial Waveguide Modes. *arXiv preprint arXiv:1601.00121* (2016). 24, 117

[24] Shalm, L. K. *et al.* Strong Loophole-Free Test of Local Realism. *Physical Review Letters* **115**, 250402 (2015). 24, 60, 115

[25] Montaut, N. *et al.* High-Efficiency Plug-and-Play Source of Heralded Single Photons. *Physical Review Applied* **8**, 024021 (2017). 24, 70, 115

[26] Christ, A., Laiho, K., Eckstein, A., Cassemiro, K. N. & Silberhorn, C. Probing multimode squeezing with correlation functions. *New Journal of Physics* **13**, 033027 (2011). 25, 26

[27] U'Ren, A. B., Banaszek, K. & Walmsley, I. A. Photon engineering for quantum information processing (2003). 27

[28] Christ, A. & Silberhorn, C. Limits on the deterministic creation of pure single-photon states using parametric down-conversion. *Physical Review A* **85**, 023829 (2012). 27, 49, 84, 91

[29] Boyd, Robert W. Chapter-2—Wave-Equation-Description-of-Nonlinear-Optical_2008_Nonlinear-Op.pdf. 28, 29

[30] Clemmen, S. *et al.* Continuous wave photon pair generation in silicon-on-insulator waveguides and ring resonators. *Optics Express* **17**, 16558 (2009). 30, 31

[31] Brainis, E. Four-photon scattering in birefringent fibers. *Physical Review A* **79**, 023840 (2009). 31

[32] Ramelow, S. *et al.* Silicon-Nitride Platform for Narrowband Entangled Photon Generation. *arXiv:1508.04358 [physics, physics:quant-ph]* (2015). 1508.04358. 31, 70

[33] Dutt, A. On-chip quantum and nonlinear optics: From squeezing to spectroscopy (2017). 32

[34] Ji, X. *et al.* Ultra-low-loss on-chip resonators with sub-milliwatt parametric oscillation threshold. *Optica* **4**, 619–624 (2017). 33

[35] Wen, Y. H., Kuzucu, O., Hou, T., Lipson, M. & Gaeta, A. L. All-optical switching of a single resonance in silicon ring resonators. *Optics Letters* **36**, 1413–1415 (2011). 34

[36] Demirtzioglou, I. *et al.* Frequency comb generation in a silicon ring resonator modulator. *Optics Express* **26**, 790–796 (2018). 34

[37] Helt, L. G., Yang, Z., Liscidini, M. & Sipe, J. E. Spontaneous four-wave mixing in microring resonators. *Optics Letters* **35**, 3006–3008 (2010). 34

[38] Vernon, Z. & Sipe, J. E. Spontaneous four-wave mixing in lossy microring resonators. *Physical Review A* **91**, 053802 (2015). 34, 35

[39] Vernon, Z. & Sipe, J. E. Strongly driven nonlinear quantum optics in microring resonators. *Physical Review A* **92**, 033840 (2015). 34

[40] Vernon, Z., Liscidini, M. & Sipe, J. E. No free lunch: The tradeoff between heralding rate and efficiency in microresonator-based heralded single photon sources. *Optics Letters* **41**, 788 (2016). 1512.04879. 34, 35

[41] Vernon, Z. & Sipe, J. E. Strongly driven nonlinear quantum optics in microring resonators. *Physical Review A* **92**, 033840 (2015). 35

[42] Tison, C. C. *et al.* The Path to Increasing the Coincidence Efficiency of Integrated Photon Sources. *arXiv:1703.08368 [quant-ph]* (2017). 1703.08368. 35

[43] Vernon, Z. *et al.* Truly unentangled photon pairs without spectral filtering. *Optics Letters* **42**, 3638–3641 (2017). 36, 86

[44] Helt, L. G., Yang, Z., Liscidini, M. & Sipe, J. E. Spontaneous four-wave mixing in microring resonators. *Optics Letters* **35**, 3006–3008 (2010). 36

[45] Scully. Field-field and photon-photon interferometry. 39

[46] Aaronson, S. Quantum Computing, Postselection, and Probabilistic Polynomial-Time. *arXiv:quant-ph/0412187* (2004). quant-ph/0412187. 39

[47] Gol'tsman, G. N. *et al.* Picosecond superconducting single-photon optical detector. *Applied Physics Letters* **79**, 705–707 (2001). 40

[48] Marsili, F. *et al.* Detecting single infrared photons with 93% system efficiency. *Nature Photonics* **7**, 210–214 (2013). 40

[49] Reddy, D. V., Lita, A. E., Nam, S. W., Mirin, R. P. & Verma, V. B. Achieving 98% system efficiency at 1550 nm in superconducting nanowire single photon detectors. In *Rochester Conference on Coherence and Quantum Optics (CQO-11)*, W2B.2 (OSA, Rochester, New York, 2019). 40

[50] Kok, P. & Braunstein, S. L. Detection devices in entanglement-based optical state preparation. *Physical Review A* **63**, 033812 (2001). quant-ph/9910084. 41

[51] Achilles, D., Silberhorn, C., Śliwa, C., Banaszek, K. & Walmsley, I. A. Fiber-assisted detection with photon number resolution. *Optics Letters* **28**, 2387–2389 (2003). 41

[52] Fitch, M. J., Jacobs, B. C., Pittman, T. B. & Franson, J. D. Photon-number resolution using time-multiplexed single-photon detectors. *Physical Review A* **68**, 043814 (2003). 41

[53] Mattioli, F. *et al.* Photon-number-resolving superconducting nanowire detectors. *Superconductor Science and Technology* **28**, 104001 (2015). 41

[54] Nehra, R., Chang, C.-H., Yu, Q., Beling, A. & Pfister, O. Photon-number-resolving segmented detectors based on single-photon avalanche-photodiodes. *Optics Express* **28**, 3660–3675 (2020). 41

[55] Lita, A. E., Miller, A. J. & Nam, S. W. Counting near-infrared single-photons with 95% efficiency. *Optics Express* **16**, 3032 (2008). 41

[56] Humphreys, P. C. *et al.* Tomography of photon-number resolving continuous-output detectors. *New Journal of Physics* **17**, 103044 (2015). 41

[57] Morais, L. A., de Almeida, M. P., Gillett, G. & White, A. G. Revealing the Number of Single Photons in Real Time. In *Frontiers in Optics + Laser Science APS/DLS (2019), Paper JTu4A.42*, JTu4A.42 (Optical Society of America, 2019). 41

[58] Zhu, D. *et al.* Resolving Photon Numbers Using a Superconducting Nanowire with Impedance-Matching Taper. *Nano Letters* **20**, 3858–3863 (2020). 41, 116

[59] Migdall, A. L., Branning, D. & Castelletto, S. Tailoring single-photon and multiphoton probabilities of a single-photon on-demand source. *Physical Review A* **66**, 053805 (2002). 43

[60] Jeffrey, E., Peters, N. A. & Kwiat, P. G. Towards a periodic deterministic source of arbitrary single-photon states. *New Journal of Physics* **6**, 100–100 (2004). 43

[61] Pittman, T. B., Jacobs, B. C. & Franson, J. D. Single photons on pseudodemand from stored parametric down-conversion. *Physical Review A* **66**, 042303 (2002). 43

[62] Shapiro, J. H. & Wong, F. N. On-demand single-photon generation using a modular array of parametric downconverters with electro-optic polarization controls. *Optics Letters* **32**, 2698–2700 (2007). 43

[63] Mower, J. & Englund, D. Efficient generation of single and entangled photons on a silicon photonic integrated chip. *Physical Review A* **84**, 052326 (2011). 43

[64] Bonneau, D., Mendoza, G. J., O'Brien, J. L. & Thompson, M. G. Effect of loss on multiplexed single-photon sources. *New Journal of Physics* **17**, 043057 (2015). 43, 84, 91

[65] Ma, X.-s., Zotter, S., Kofler, J., Jennewein, T. & Zeilinger, A. Experimental generation of single photons via active multiplexing. *Physical Review A* **83**, 043814 (2011). 43

[66] Broome, M. A., Almeida, M. P., Fedrizzi, A. & White, A. G. Reducing multi-photon rates in pulsed down-conversion by temporal multiplexing. *Optics Express* **19**, 22698 (2011). 43

[67] Collins, M. J. *et al.* Integrated spatial multiplexing of heralded single-photon sources. *Nature communications* **4**, 2582 (2013). 43

[68] Mendoza, G. J. *et al.* Active temporal and spatial multiplexing of photons. *Optica* **3**, 127 (2016). 43

[69] Xiong, C. *et al.* Active temporal multiplexing of indistinguishable heralded single photons. *Nature Communications* **7**, 10853 (2016). 43, 51

[70] Kaneda, F. *et al.* Time-multiplexed heralded single-photon source. *Optica* **2**, 1010–1013 (2015). 43, 51, 59

[71] Francis-Jones, R. J. A., Hoggarth, R. A. & Mosley, P. J. All-fiber multiplexed source of high-purity single photons. *Optica* **3**, 1270–1273 (2016). 43

[72] Christ, A. & Silberhorn, C. Limits on the deterministic creation of pure single-photon states using parametric down-conversion. *Physical Review A* **85**, 023829 (2012). 43, 48

[73] Kaneda, F. *et al.* Temporal Multiplexing toward Periodic and Deterministic Single-Photon Sources. FM2A.5 (OSA, 2015). 43

[74] Kaneda, F. & Kwiat, P. G. High-efficiency single-photon generation via large-scale active time multiplexing. *Science Advances* **5**, eaaw8586 (2019). 43, 59

[75] Joshi, C., Farsi, A., Ramelow, S., Clemmen, S. & Gaeta, A. L. Frequency multiplexing for quasi-deterministic heralded single-photon sources. In *Conference*

on Lasers and Electro-Optics (2016), paper FTh1C.2, FTh1C.2 (Optical Society of America, 2016). 44

[76] Roslund, J., de Araújo, R. M., Jiang, S., Fabre, C. & Treps, N. Wavelength-multiplexed quantum networks with ultrafast frequency combs. *Nature Photonics* **8**, 109–112 (2014). 44, 71

[77] Humphreys, P. C. *et al.* Continuous-variable quantum computing in optical time-frequency modes using quantum memories. *Physical Review Letters* **113**, 130502 (2014). 44

[78] Sinclair, N. *et al.* Spectral Multiplexing for Scalable Quantum Photonics using an Atomic Frequency Comb Quantum Memory and Feed-Forward Control. *Physical Review Letters* **113**, 053603 (2014). 44

[79] Lukens, J. M. & Lougovski, P. Frequency-encoded photonic qubits for scalable quantum information processing. *Optica* **4**, 8–16 (2017). 44

[80] Puigibert, M. G. *et al.* Heralded single photons based on spectral multiplexing and feed-forward control. *arXiv:1703.02068 [quant-ph]* (2017). 1703.02068. 44

[81] Bonneau, D., Mendoza, G. J., O'Brien, J. L. & Thompson, M. G. Effect of loss on multiplexed single-photon sources. *New Journal of Physics* **17**, 043057 (2015). 48, 51

[82] Brown, R. H. & Twiss, R. Q. Correlation between Photons in two Coherent Beams of Light. *Nature* **177**, 27–29 (1956). 59

[83] Ramelow, S. *et al.* Highly efficient heralding of entangled single photons. *Optics Express* **21**, 6707 (2013). 60

[84] Helt, L. G., Yang, Z., Liscidini, M. & Sipe, J. E. Spontaneous four-wave mixing in microring resonators. *Optics Letters* **35**, 3006–3008 (2010). 61, 63

[85] Azuma, K., Tamaki, K. & Lo, H.-K. All-photonic quantum repeaters. *Nature Communications* **6**, ncomms7787 (2015). 63

[86] Reimer, C. *et al.* Integrated frequency comb source of heralded single photons. *Optics Express* **22**, 6535 (2014). 63

[87] Reimer, C. *et al.* Generation of multiphoton entangled quantum states by means of integrated frequency combs. *Science* **351**, 1176–1180 (2016). 63

[88] Ramelow, S. *et al.* Silicon-Nitride Platform for Narrowband Entangled Photon Generation. *arXiv:1508.04358 [physics, physics:quant-ph]* (2015). 1508.04358. 63

[89] Agha, I., Davanço, M., Thurston, B. & Srinivasan, K. Low-noise chip-based frequency conversion by four-wave-mixing Bragg scattering in SiN_x waveguides. *Optics Letters* **37**, 2997–2999 (2012). 63

[90] Hong, C. K., Ou, Z. Y. & Mandel, L. Measurement of subpicosecond time intervals between two photons by interference. *Physical Review Letters* **59**, 2044–2046 (1987). 68

[91] Pittman, T. B. *et al.* Can Two-Photon Interference be Considered the Interference of Two Photons? *Physical Review Letters* **77**, 1917–1920 (1996). 68, 85

[92] Bouwmeester, D., Pan, J.-W., Daniell, M., Weinfurter, H. & Zeilinger, A. Observation of Three-Photon Greenberger-Horne-Zeilinger Entanglement. *Physical Review Letters* **82**, 1345–1349 (1999). 68, 119

[93] Knill, E., Laflamme, R. & Milburn, G. J. A scheme for efficient quantum computation with linear optics. *nature* **409**, 46–52 (2001). 68

[94] Spring, J. B. *et al.* Boson Sampling on a Photonic Chip. *Science* **339**, 798–801 (2013). 68, 96

[95] Ewert, F. & van Loock, P. $3/4$-Efficient Bell Measurement with Passive Linear Optics and Unentangled Ancillae. *Physical Review Letters* **113**, 140403 (2014). 68

[96] Raymer, M. G., van Enk, S. J., McKinstrie, C. J. & McGuinness, H. J. Interference of two photons of different color. *Optics Communications* **283**, 747–752 (2010). 69

[97] Zwerger, M., Dür, W. & Briegel, H. J. Measurement-based quantum repeaters. *Physical Review A* **85**, 062326 (2012). 70, 119

[98] Azuma, K., Tamaki, K. & Lo, H.-K. All-photonic quantum repeaters. *Nature Communications* **6**, 6787 (2015). 70, 119

[99] Joshi, C., Farsi, A., Clemmen, S., Ramelow, S. & Gaeta, A. L. Frequency multiplexing for quasi-deterministic heralded single-photon sources. *Nature Communications* **9**, 1–8 (2018). 70, 80, 86, 89, 95

[100] Hiemstra, T. *et al.* Pure Single Photons from Scalable Frequency Multiplexing. *arXiv:1907.10355 [quant-ph]* (2019). 1907.10355. 70

[101] Reimer, C. *et al.* Integrated frequency comb source of heralded single photons. *Optics Express* **22**, 6535 (2014). 70

[102] Harris, N. C. *et al.* Integrated Source of Spectrally Filtered Correlated Photons for Large-Scale Quantum Photonic Systems. *Physical Review X* **4**, 041047 (2014). 70

[103] Jiang, W. C., Lu, X., Zhang, J., Painter, O. & Lin, Q. Silicon-chip source of bright photon pairs. *Optics Express* **23**, 20884–20904 (2015). 70

[104] Grassani, D. *et al.* Micrometer-scale integrated silicon source of time-energy entangled photons. *Optica* **2**, 88–94 (2015). 70

[105] Meyer-Scott, E. *et al.* High-performance source of spectrally pure, polarization entangled photon pairs based on hybrid integrated-bulk optics. *Optics Express* **26**, 32475–32490 (2018). 70

[106] Qiang, X. *et al.* Large-scale silicon quantum photonics implementing arbitrary two-qubit processing. *Nature Photonics* **12**, 534–539 (2018). 70

[107] Paesani, S. *et al.* Generation and sampling of quantum states of light in a silicon chip. *Nature Physics* **15**, 925–929 (2019). 70

[108] Farsi, A. *Coherent Manipulation Of Light In The Classical And Quantum Regimes Via Four-Wave Mixing Bragg Scattering*. Ph.D. thesis, Cornell University (2015). 70

[109] Kues, M. *et al.* On-chip generation of high-dimensional entangled quantum states and their coherent control. *Nature* **546**, 622–626 (2017). 71

[110] Reimer, C. *et al.* High-dimensional one-way quantum processing implemented on d -level cluster states. *Nature Physics* **15**, 148–153 (2019). 71

[111] Imany, P. *et al.* High-dimensional optical quantum logic in large operational spaces. *npj Quantum Information* **5**, 1–10 (2019). 71

[112] Mérolla, J.-M., Mazurenko, Y., Goedgebuer, J.-P. & Rhodes, W. T. Single-Photon Interference in Sidebands of Phase-Modulated Light for Quantum Cryptography. *Physical Review Letters* **82**, 1656–1659 (1999). 71

[113] Olislager, L. *et al.* Frequency-bin entangled photons. *Physical Review A* **82**, 013804 (2010). 71

[114] Olislager, L. *et al.* Creating and manipulating entangled optical qubits in the frequency domain. *Physical Review A* **89**, 052323 (2014). 71

[115] Lu, H.-H. *et al.* Quantum interference and correlation control of frequency-bin qubits. *Optica* **5**, 1455–1460 (2018). 71

[116] Imany, P. *et al.* Frequency-domain Hong-Ou-Mandel interference with linear optics. *Optics Letters* **43**, 2760–2763 (2018). 71

[117] Lu, H.-H. *et al.* Electro-Optic Frequency Beam Splitters and Tritters for High-Fidelity Photonic Quantum Information Processing. *Physical Review Letters* **120**, 030502 (2018). 71

[118] Galmès, B., Phan-Huy, K., Furfaro, L., Chembo, Y. K. & Merolla, J.-M. Nine-frequency-path quantum interferometry over 60 km of optical fiber. *Physical Review A* **99**, 033805 (2019). 71

[119] Kobayashi, T. *et al.* Frequency-domain Hong–Ou–Mandel interference. *Nature Photonics* **10**, 441–444 (2016). 71

[120] Legero, T., Wilk, T., Hennrich, M., Rempe, G. & Kuhn, A. Quantum Beat of Two Single Photons. *Physical Review Letters* **93**, 070503 (2004). 77

[121] Legero, T., Wilk, T., Kuhn, A. & Rempe, G. Time-resolved two-photon quantum interference. *Applied Physics B* **77**, 797–802 (2003). 77

[122] Roztocki, P. *et al.* Pulsed quantum frequency combs from an actively mode-locked intra-cavity generation scheme. In *2017 Conference on Lasers and Electro-Optics (CLEO)*, 1–1 (2017). 86, 93

[123] Agha, I., Davanço, M., Thurston, B. & Srinivasan, K. Low-noise chip-based frequency conversion by four-wave-mixing Bragg scattering in SiN_x waveguides. *Optics Letters* **37**, 2997–2999 (2012). 86, 117

[124] Li, Q., Davanço, M. & Srinivasan, K. Efficient and low-noise single-photon-level frequency conversion interfaces using silicon nanophotonics. *Nature Photonics* **10**, 406–414 (2016). 86, 117

[125] Li, K., Sun, H. & Foster, A. C. Four-wave mixing Bragg scattering in hydrogenated amorphous silicon waveguides. *Optics Letters* **42**, 1488–1491 (2017). 86, 117

[126] Bell, B. A., Xiong, C., Marpaung, D., McKinstrie, C. J. & Eggleton, B. J. Unidirectional wavelength conversion in silicon using four-wave mixing driven by cross-polarized pumps. *Optics Letters* **42**, 1668–1671 (2017). 86

[127] Lukens, J. M. & Lougovski, P. Frequency-encoded photonic qubits for scalable quantum information processing. *Optica* **4**, 8–16 (2017). 94

[128] Lu, H.-H. *et al.* Quantum interference and correlation control of frequency-bin qubits. *Optica* **5**, 1455 (2018). 94

[129] Aaronson, S. & Arkhipov, A. The Computational Complexity of Linear Optics. In *Proceedings of the Forty-Third Annual ACM Symposium on Theory of Computing*, STOC '11, 333–342 (ACM, New York, NY, USA, 2011). 96

[130] Shepherd, D. & Bremner, M. J. Temporally unstructured quantum computation. *Proceedings of the Royal Society A: Mathematical, Physical and Engineering Sciences* **465**, 1413–1439 (2009). 96

[131] Bremner, M. J., Jozsa, R. & Shepherd, D. J. Classical simulation of commuting quantum computations implies collapse of the polynomial hierarchy. *Proceedings of the Royal Society A: Mathematical, Physical and Engineering Sciences* **467**, 459–472 (2011). 96

[132] Aaronson, S. & Chen, L. Complexity-Theoretic Foundations of Quantum Supremacy Experiments. *arXiv:1612.05903 [quant-ph]* (2016). 1612.05903. 96

[133] Bouland, A., Fefferman, B., Nirkhe, C. & Vazirani, U. On the complexity and verification of quantum random circuit sampling. *Nature Physics* **15**, 159–163 (2019). 96

[134] Turing, Alan. On computable numbers, with an application to the entscheidungsproblem. *Proceedings of the London mathematical society* **2**, 230–265 (1937). 96

[135] Huang, Z. *et al.* Photonic quantum data locking. *arXiv:1905.03013 [quant-ph]* (2020). 1905.03013. 96

[136] Nikolopoulos, G. M. Cryptographic One-way Function Based on Boson Sampling. *Quantum Information Processing* **18**, 259 (2019). 1907.01788. 96

[137] Broome, M. A. *et al.* Photonic Boson Sampling in a Tunable Circuit. *Science* **339**, 794–798 (2013). 96

[138] Loredo, J. C. *et al.* Boson Sampling with Single-Photon Fock States from a Bright Solid-State Source. *Physical Review Letters* **118**, 130503 (2017). 96

[139] Wang, H. *et al.* Boson Sampling with 20 Input Photons and a 60-Mode Interferometer in a $1{0}{\hat{1}4}$-Dimensional Hilbert Space. *Physical Review Letters* **123**, 250503 (2019). 97

[140] Brecht, B., Reddy, D. V., Silberhorn, C. & Raymer, M. G. Photon temporal modes: A complete framework for quantum information science. *Physical Review X* **5**, 041017 (2015). 1504.06251. 101

[141] Reddy, D. V., Raymer, M. G., McKinstrie, C. J., Mejling, L. & Rottwitt, K. Temporal mode selectivity by frequency conversion in second-order nonlinear optical waveguides. *Optics Express* **21**, 13840–13863 (2013). 101, 110

[142] Reddy, D. V., Raymer, M. G. & McKinstrie, C. J. Efficient sorting of quantum-optical wave packets by temporal-mode interferometry. *Optics Letters* **39**, 2924 (2014). 101

[143] Reddy, D. V., Raymer, M. G. & McKinstrie, C. J. Sorting photon wave packets using temporal-mode interferometry based on multiple-stage quantum frequency conversion. *Physical Review A* **91** (2015). 101, 110

[144] Brecht, B., Eckstein, A., Christ, A., Suche, H. & Silberhorn, C. From quantum pulse gate to quantum pulse shaper—engineered frequency conversion in nonlinear optical waveguides. *New Journal of Physics* **13**, 065029 (2011). 101

[145] Ansari, V. *et al.* Tomography and Purification of the Temporal-Mode Structure of Quantum Light. *Physical Review Letters* **120**, 213601 (2018). 101

[146] Salem, R., Foster, M. A. & Gaeta, A. L. Application of space–time duality to ultrahigh-speed optical signal processing. *Advances in Optics and Photonics* **5**, 274 (2013). 101

[147] Kolner, B. H. & Nazarathy, M. Temporal imaging with a time lens. *Optics Letters* **14**, 630 (1989). 103

[148] Reddy, D. V. & Raymer, M. G. Engineering temporal-mode-selective frequency

conversion in nonlinear optical waveguides: From theory to experiment. *Optics Express* **25**, 12952–12966 (2017). 110

[149] Reddy, D. V., Raymer, M. G. & McKinstrie, C. J. Efficient sorting of quantum-optical wave packets by temporal-mode interferometry. *Optics Letters* **39**, 2924–2927 (2014). 110

[150] Mazur, M. *et al.* Multi-wavelength arbitrary waveform generation through spectro-temporal unitary transformations. *arXiv:1907.02595 [physics]* (2019). 1907.02595. 111, 120

[151] Fontaine, N. K. *et al.* Laguerre-Gaussian mode sorter. *Nature Communications* **10**, 1–7 (2019). 111, 112, 120

[152] Ramelow, S. *et al.* Highly efficient heralding of entangled single photons. *Optics Express* **21**, 6707 (2013). 115

[153] Giustina, M. *et al.* Significant-Loophole-Free Test of Bell's Theorem with Entangled Photons. *Physical Review Letters* **115**, 250401 (2015). 115

[154] Clark, A. S., Shahnia, S., Collins, M. J., Xiong, C. & Eggleton, B. J. High-efficiency frequency conversion in the single-photon regime. *Optics Letters* **38**, 947 (2013). 117

[155] Kossey, M., Li, K., Sun, H. & Foster, A. C. Four-Wave Mixing in a Multi-Layer SiNx/a-Si:H Photonic Chip. In *Conference on Lasers and Electro-Optics (2018), Paper STh3I.5*, STh3I.5 (Optical Society of America, 2018). 117

[156] MacFarlane, N., Kossey, M. R., Stroud, J. R., Foster, M. A. & Foster, A. C. A multi-layer platform for low-loss nonlinear silicon photonics. *APL Photonics* **4**, 110809 (2019). 117

[157] Bell, B. A., Xiong, C., Marpaung, D., McKinstrie, C. J. & Eggleton, B. J. Unidirectional wavelength conversion in silicon using four-wave mixing driven by cross-polarized pumps. *Optics Letters* **42**, 1668–1671 (2017). 117

[158] Zhao, Y. *et al.* Visible nonlinear photonics via high-order-mode dispersion engineering. *Optica* **7**, 135–141 (2020). 117

[159] Kang, D., Kim, M., He, H. & Helmy, A. S. Two polarization-entangled sources from the same semiconductor chip. *Physical Review A* **92**, 013821 (2015). 118

[160] Krenn, M., Hochrainer, A., Lahiri, M. & Zeilinger, A. Entanglement by Path Identity. *Physical Review Letters* **118** (2017). 118, 119

[161] Raussendorf, R., Browne, D. E. & Briegel, H. J. Measurement-based quantum computation with cluster states. *Physical Review A* **68**, 022312 (2003). quant-ph/0301052. 118

[162] Pant, M., Towsley, D., Englund, D. & Guha, S. Percolation thresholds for photonic quantum computing. *Nature Communications* **10** (2019). 119

[163] Rudolph, T. Why I am optimistic about the silicon-photonic route to quantum computing. *APL Photonics* **2**, 030901 (2017). 119

[164] Lu, C.-Y. *et al.* Experimental entanglement of six photons in graph states. *Nature Physics* **3**, 91–95 (2007). 119

[165] Gimeno-Segovia, M. *et al.* Relative multiplexing for minimizing switching in linear-optical quantum computing. *New Journal of Physics* **19**, 063013 (2017). 1701.03306. 119

[166] Ji, X. *et al.* Ultra-low-loss on-chip resonators with sub-milliwatt parametric oscillation threshold. *Optica* **4**, 619–624 (2017). 119

[167] Xu, Q., Dong, P. & Lipson, M. Breaking the delay-bandwidth limit in a photonic structure. *Nature Physics* **3**, 406–410 (2007). 119

[168] Dutt, A. *et al.* Experimental band structure spectroscopy along a synthetic dimension. *Nature Communications* **10** (2019). 120

[169] Dutt, A. *et al.* A single photonic cavity with two independent physical synthetic dimensions. *Science* **367**, 59–64 (2020). 120

[170] Houtz, R., Chan, C. & Müller, H. Wideband, Efficient Optical Serrodyne Frequency Shifting with a Phase Modulator and a Nonlinear Transmission Line. *Optics Express* **17**, 19235–19240 (2009). 120

[171] Yuan, L. & Fan, S. Bloch oscillation and unidirectional translation of frequency in a dynamically modulated ring resonator. *Optica* **3**, 1014–1018 (2016). 120

[172] Hu, Y. *et al.* Reconfigurable electro-optic frequency shifter (2020). 120